FOCAL MODULATION MICROSCOPY
A NOVEL OPTICAL IMAGING METHOD

Wong Chee Howe
B.Eng(Hons), NUS
October 2010

A THESIS SUBMITTED

FOR THE DEGREE OF DOCTOR OF PHILOSOPHY IN
ELECTRICAL AND COMPUTER ENGINEERING

DEPARTMENT OF ELECTRICAL AND COMPUTER
ENGINEERING

NATIONAL UNIVERSITY OF SINGAPORE

Abstract

This thesis proposes a novel method for improving the imaging depth of a microscope based on focal modulation. The usual method for improving imaging depth often relies on the use of a long wavelength light source. Light with a spectrum closer to red, generally suffers lower extinction due to reduced scattering in the water-predominant tissue environment. However, this often precludes the usage of the current fluorescence dye suite and inhibits long wavelength source usage proliferation. The focal modulation approach aims to circumvent the above inhibition while affording the advantage of improved imaging depth without usage of a long wavelength source.

Focal modulation is a method in which the focal point intensity is modulated via interference between a reference and a frequency phase modulated beam. Due to the sinusoidal frequency modulation of these interfered beams, the focal point intensity profile is constantly varying, with the main central lobe and the side lobes intensity varying from maximum to minimum periodically. On a fluorescence labelled specimen sample, the resultant fluorescence intensity will be modulated with the excitation beam, though the time-averaged fluorescence intensity will be equivalent to that of a conventional confocal microscope. The detector plane pinhole subsequently acts as a filter, blockading the side lobe intensity contribution and allows for retrieval of the modulated intensity.

A prototype optical system which resembles closely to a conventional confocal microscope, is constructed to verify the concept. A pair of mirrors, each forming a half of the aperture and on which a piezoshifter is attached to one of them, is used to form the illumination aperture of the system. A sinusoidal control signal is supplied

to the piezoshifter and the fluorescence light is then gathered via fiber optics attached to a PMT. Three different types of specimen (fluospheres, Schefflera arboricola and chicken cartilage) were used to study the proposed idea. From the experimental results, an improved sectioning effect is observed in the focal modulation microscope over the confocal microscope.

Hence it is proposed that the focal modulation microscope provides a method in which the imaging depth is improved, yet at a minimal installation cost in terms of hardware and manpower.

Acknowledgement

The pursuit of a PhD degree can often be compared to a lonely and fustrating voyage. Yet it is with the assistance, companionship and kindness of the numerous people listed here, that I have completed my study and this dissertation. I would like to express my gratitude and appreciation for the following people:

My supervisor, Dr Chen for his support, trust and help in making this study possible. You have always been ready to help out on for every little aspect of this project, knowing that I am a mere novice in optics. Your dedication and industrious attitude have certainly left an impression on me. Forgive my doubts and pessimismistic remarks that I have given many a times

My co-supervisor, Prof Sheppard who has always lent his time generously to my ad hoc visit and discussion. You have been a great source of knowledge and yet have always lent listening ears to my wild suggestions, no matter how stupid they might be. Thanks for the extra mile that you are willing to go through for me. You have been the perfect academic scholar I looked up to.

Everyone in the lab, whom has aided me and been a constant source of companionship . Without all the academic discussion and social diversion that you guys have provided, this journey would have been unbearable. Thanks for all the great help, regardless of whether you have simply helped to turn a screw or solved a particularly crucial problem for me. It has been my privilege to know you all.

My family, for their patience, support and understanding for this time period.

Forgive my many faults and thoughtlessness which have often caused you grief. My pursuit of this dream have meant the laying down of yours and replacing them with much financial burden and the cares of life. For you all, I am the most gratified.

For those who are with me at the beginning of this venture but who are unable to see it together with me at the end. Thank you.

God, for his presence in the garish day or in the darkest night. For You alone know my pains, the things I have given up and my failures during this time period. Thanks for watching over me.

In the event of any errors or omissions in this report, it is my negligence and the responsibility is my alone.

What a journey this has been!

God saw that the light was good, and He separated the light from the darkness

Genesis 1:4

Contents

List of Tables

List of Figures

List of Abbreviations

The following list of abbreviation is used in the thesis unless otherwise explicitly stated

AM	Amplitude Modulation
CCD	Charge Coupled Device
CM	Confocal Microscopy
CT	Computed Tomography
DAQ	Data Acquisition
DR	Dynamic Range
FLIM	Fluorescence Lifetime Imaging Microscopy
FWHM	Full Width Half Measure
IPSF	Intensity Point Spread Function
KDP	Potassium Dihydrogen Phosphate
MPM	Multi-Photon Microscopy
MRI	Magnetic Resonance Imaging
NA	Numerical Aperture
NEP	Noise Equivalent Power
OCM	Optical Coherence Microscopy
OCT	Optical Coherence Tomography
OTF	Optical Transfer Function

PBS	Phosphate Buffered Saline
PC	Personal Computer
PMT	Photo Multiplier Tube
PSF	Point Spread Function
QE	Quantum Efficiency
RTE	Radiative Transfer Equation
SBR	Signal to Background Ratio
SHG	Second Harmonic Generation
SIM	Structured Illumination Microscopy
SNR	Signal to Noise Ratio
TPEF	Two Photon Excitation Fluorescence

Chapter 1

Introduction

1.1 Background and overview

1.1.1 Overview of in-vivo optical imaging

There is an evolving capability in novel non-invasive clinical imaging methods and instrumentation to monitor biological systems based upon optical (photonic) technologies. Optical imaging techniques have been employed widely in clinical imaging such as in endoscopy [1, 2] as well as ophthamology [3, 4]. The re-emergence of these techniques is brought about with the tremendous growth in biomedical science and biotechnology. Many of the techniques are still largely in the developmental stage and have not been widely adopted as standard clinical practice. The potential roles for optical imaging include diagnosis (e.g. detection of disease, particularly early detection), staging, disease localization for therapeutic guidance, monitoring of therapeutic response, and monitoring of metabolic and physiological functions.

1.1.2 In-vivo optical imaging information return

Different information can be obtained via optical imaging, not just merely the conventional image that is formed via capturing sample-scattered light. Light interaction with tissue does not merely provide us with information pertaining to the spatial

description of an organism but also includes chemical- and temporal-specific information. The ultimate goal is for optical imaging to be able to provide "functional" information to assist in diagnosis or research. In general, information from optical imaging can be captured in three disparate categories:

1. By spectrum - Spectrum profile of collected light that has been altered either by tissue absorption or emission from fluorescence that is bound to the subject of interest(tissue/organism) [5, 6].

2. By spatial - The collected backscattered/transmitted light is used to depict the spatial image [7].

3. By temporal - Light propagation through the tissue is being studied against the time progression. Indirect measurement of tissue property is realised by correlating the light propagation to the impediment suffered within the tissue or simply the tissue density. Events such as scattering, reflection and absorption could be recorded to give time-dependent information on tissue [8, 9, 10].

In general, optical imaging has been deployed in three distinct levels: surface, subsurface and volumetric. Surface imaging [11] has often been employed in the familiar mode of endoscopy and conventional microscopy. Studies into the deeper specimen region would often require physical sectioning or biopsy. Subsurface imaging was implemented recently with the introduction of optical techniques such as confocal microscopy [12, 13] and optical coherence tomography [14, 15]. These approaches offer an optical sectioning capability which does not require physical sectioning. In-vivo volumetric readings are much more ardous to achieve compared to the traditional imaging modalities such as MRI and CT. A multiple imaging head and detectors via a complex transmission tomography algorithm are often used in the optical imaging method to surmount this problem [16].

1.1.3 Advantage of in-vivo optical imaging

The fundamental advantage of in vivo optical imaging is that it can directly provide "molecular" information, because the photon energies are in the range of molecular energy levels. In addition, since the wavelength involved is small, light is sensitive to the tissue microstructure. Hence, optical imaging fits well with advances in molecular medicine and is likely to play a major role as new molecularly-based diagnostic and therapeutic techniques are implemented. In addition to this, optical imaging can be performed with little or no hazard to the patient compared to other ionizing imaging modalities such as CT.

Another important factor is that optical or light based imaging has a cost advantage opposed to other form of imaging such as MRI and CT. Cost consideration is often a critical factor in providing preventive and diagnostic medical treatment where early therapeutic examination and intervention could possibly mitigate and relieve life threatening conditions in patients.

The option of real time imaging is made attainable with optical techniques of high acquisition speed. Despite improved MRI and CT imaging rates over the years, a number of cell events [17] still occur at a speed which can only be observed via optical imaging. The higher imaging speed from optical techniques over MRI and CT delivers a safer and more effective method for surgery guidance. Also as discussed above, the non-ionizing nature of the optical techniques permits continuous monitoring of a subject's different physiological function without harming or damaging the tissue [18].

Endogenous light-absorbing pigments such as melanin, myoglobin, hemoglobin and other chromophores, have an absorption spectrum which is often wavelength dependent and falls within visible light range. This would give better differentiation to the specimen under study. Many of the laboratory developed biomarkers such as GFP would be able to be used. This allows for many developed microscopic techniques to be ported over, together with the usage familiarity and experience.

1.2 Problem of tissue interaction with light

1.2.1 Overview of light-tissue interaction

The development of optical methods as a futuristic imaging tool is hampered by the not fully-understood interaction of light with biological tissues. The nature of tissue presents a formidable problem outstretching the complexities encountered in applications such as laser radar or optical remote sensing. Biological tissues are highly heterogeneously structured with building blocks ranging from a few nanometers to hundreds of microns that are potential light scattering centers. The high water content and presence of absorbing pigments within a tissue further compound the problem of light propagation. The various process that light undergoes within tissue [9] is given below in Figure 1.1.

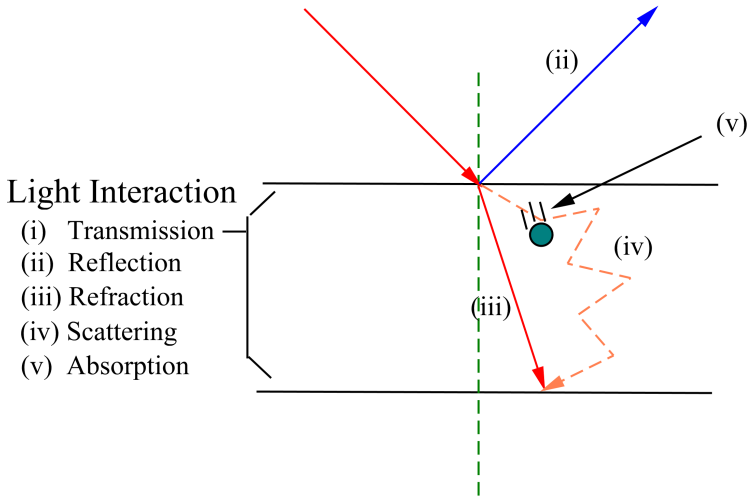

Figure 1.1: Light interaction with tissue

Light used in optical imaging often lacks tissue penetrating power and subsurface imaging is often a problem as there is often little to no returning light to the detector. In general, absorption by water could be discounted, especially if one uses light within the water window wavelength (between 0.65 - 1.4 μm). In this window, the absorption coefficient varies between $0.003 - 0.007 cm^{-1}$ which poses insignificant attenuation to

the infrared light propagation through the sample. Photonic energy absorbed by the tissue is transformed to heat, kinetic, chemical or light energy.

A much pronounced obstacle lies in the issue of optical radiation scattering. Scattering is a phenomenon in which optical radiation is forced to deviate from its straight trajectory in the medium after encountering the medium's non-uniformities. The scattering mean free path or the mean distance in which a photon will be able to travel before being scattered is around $100\mu m$. There is a possibility that a photon that arrive at a photodetector might not be from its originally intended propagation orientation. A deviant photon could reach the photodetector and cloud the resultant image. Diffraction limited images are solely attainable with thin tissue where scattering is limited. This introduces formidable challenges for optical imaging which employs optical sectioning techniques.

Even though an infrared light source is employed to overcome this problem, optical imaging still suffers from a low contrast predicament. For cancer detection, normal and abnormal cells differ marginally particularly during early stages. Perceived contrast from two disparate cell types is frequently too poor to make an accurate diagnosis leading to elevated risk in misdiagnosis and quantification. Decision making is thus hampered for prompt therapeutic intervention. Highly sensitive detectors are frequently demanded in optical imaging, particularly for auto fluorescence detection, which increase the setup complexity and cost.

1.2.2 Scattering problem with microscopy

Scattering limits the imaging depth in soft tissue with the conventional microscope. It becomes virtually impossible to distinguish light contribution from the in-focus region and out-of focus region when imaging tissue of considerable depth($\approx 100\mu m$) [19]. The advent of the confocal microscope which utilizes point illumination and a pinhole in an optically conjugated plane in front of the detector proves to be capable of eliminating out of focus light [20, 21, 22, 23]. This major breakthrough however is not adequate to effectively deter some multiply scattered photons from reaching

the detector. Consequently, high resolution detail from the deeper region would still be clouded by the strong scattered background signal. The broadening of the point spread function with increasing imaging depth [24] further exacerbates the problem, degrading resolution and thus concealing fine details from the microscope user.

The new generation of microscope techniques such as the nonlinear microscope (eg multiphoton microscope) and coherence gating-based OCT features better imaging depth over confocal microscope. The nonlinear excitation requirement of multiphoton microscopy [25, 26, 27] confines excitation to the focused volume as well as suppressing the contribution from out of focus illumination. The coherence gating mechanism of OCT [28, 29, 30, 31] excels in eliminating out of focus light while selecting the backscattered light.

These latest techniques are not free from their woes. The multiphoton microscope utilizes an expensive laser and is limited currently by the range of fluorescence dyes it can utilize, while OCT is generally incompatible with fluorescence usage, limiting its molecular imaging capability [32, 33, 34]. Extensive research is underway to overcome the above mentioned problems.

1.3 Objectives

The problem associated with the new optical imaging techniques poses a major obstacle to the introduction of optical imaging as a standard clinical imaging modality. In order to overcome the problem, compromises often have to be made and these imaging methods remain as qualified success. This has prompted a relook into ways and methods that could be used to improve on the current confocal microscope, which is often regarded as the microscopy "gold" standard.

On the whole, for an optical imaging modality to be widely accepted in clinical settings, it has to be able to produce quality images with sufficient resolution beyond the superficial layer. Yet at the same time, the complexity and cost of the improvement should be affordable. Fluorescence compatibility is likewise essential so as to

conduct research that uncovers molecular interaction of biological specimen.

1.4 Organisation of the thesis

This dissertation presents the development of a novel technique in microscopy, focal modulation microscopy. Focal modulation microscopy proposed a superior mechanism in rejecting out of focus light when compared to confocal microscope. Consequently, the technique offered improved sectioning ability and noteworthy imaging depth increment over the conventional confocal microscope. This scheme relies on a simple modification to the pupil aperture of the confocal and does not introduce steep setup cost. At the same time, the technique compatibility with biomarkers, particularly fluorescence is maintained.

The dissertation is arranged as follows. First, an in-depth discussion on scattering modes together with optical sectioning techniques will be put forth. Previous work done for structured illumination from which focal modulation microscopy draws some of its inspiration will be discussed. A short discussion on the noise and detection system will be presented. The next chapter will derive a general formulation of the focal modulation microscope and some theoretical discussions will be made to discern its capability. Next, the physical implementation of the focal modulation microscope will be exhibited. After this the experimental results will be discussed, showcasing the improved deep imaging and sectioning effect. Finally the dissertation will end off with suggestions for future development direction and new imaging techniques that could be integrated with the focal modulation approach.

Chapter 2

Literature Review

2.1 Introduction

For this chapter, different modes of scattering will be reviewed in conjunction with techniques employed by other researchers to overcome or eliminate the scattering predicament. A brief discussion on optical sectioning will be accompanied with a survey of various optical sectioning techniques. Their susceptibility to scattering will be mentioned. Structured illumination which the focal modulation microscopy derives its idea from will be brought up for discussion. Discussion on various types of noise and detector system is likewise given to provide for system evaluation.

2.2 Scattering

The investigation of phenomenon that occurs commonly in our everyday life frequently provides a new staging point in the quest for new knowledge. The study into the colour of sky by Lord Rayleigh [35, 36] and John Tyndall established its relationship to the scattering effect, which has far outreaching significance. The explanation offered by the scattering effect is extended to the interpretation of similar observations in liquids [37, 38] and even amorphous solids [39, 40], providing guidance as an experiment aid to ensuing molecular structural study. Even though years have advanced man's understanding of light scattering effects, and in return brought forth

numerous applications [41, 42, 43] in which light scattering could be employed, our understanding of this phenomenon has remained wanting. The study of light scattering still continues to bring one into some of the deepest problem in chemistry and physics.

2.2.1 Types of Scattering

Scattering is an optical process in which the incident light wave direction and/or wavelength are changed. The alteration is attributed to the collision of individual photons with particles or centers of inhomogeneity in the medium. The process is highly influenced by the scattering medium physical properties such as size, density and the state of the inhomogeneity center. The scattering process could be established and classified into two broad based categories [44, 45], according to differences in energy transfer as shown in Figure 2.1.

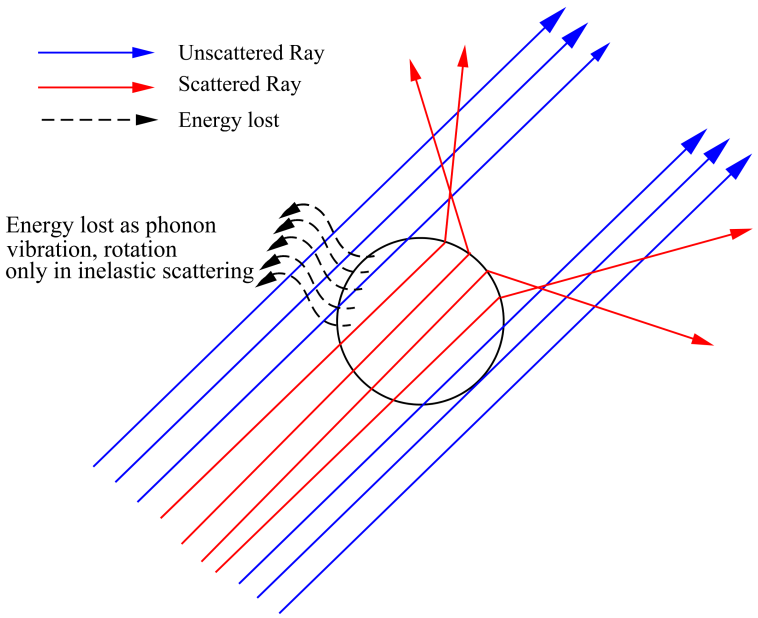

Figure 2.1: Two different scattering modes.
2 different forms of scattering exist: (i) Elastic & (ii) Inelastic. They differ by that in inelastic scattering, energy is lost.

Elastic Light Scattering

This form of scattering events merely alters light propagation direction, leaving photon energy and hence the initial light wavelength unchanged. The scattering of light by particles that are in the small size parameter regime ($\leq 1\lambda$) can be described by the theory of Rayleigh scattering [46, 47, 48]. Rayleigh scattering is the dominant reason for the colour of the blue sky due to light interaction with the air molecule [49].

In contrast to Rayleigh scattering theory, Mie theory [48, 50] provides a complete analytical solution of Maxwell's equations for the scattering of electromagnetic radiation by spherical particles. The scattering cross section is named as the Mie scattering cross-section. For Mie scattering, the scattering center is assumed to be a homogenous and isotropic sphere. Mie scattering is applied in broader context usage, such as optical metrology and biological tissue simulation.

Both scattering process described above have their postulation based upon a static scattering center. Electromagnetic radiation scattered from a moving center experiences Doppler shift and the output light has its frequency altered and suffered from a decrement in energy. Such form of light scattering is known as dynamic scattering [51, 52] and is sometimes classified under quasi-elastic scattering (due to the slight loss of energy). It details the scattering process with spherical particles in Brownian motion. Such a process is adopted in the explanation of real time system dynamics and applied to particle size measurement in chemistry, biological and physics fields [53].

The differences between various forms of elastic scattering is summarised by the Table 2.1 below.

Elastic Scattering types	Size of scattering center	Mobility	Energy Loss
Rayleigh	Smaller than wavelength	No	No
Mie	Equivalent to wavelength	No	No
Dynamic	Non Applicable	Yes	Slight

Table 2.1: Classification of different types of elastic scattering.

Non-Elastic Scattering

In non-elastic scattering, the energy of the incoming light is not conserved and the scattered photons have a longer wavelength to that of the incident light [45]. This mode of scattering corresponds to molecular perturbation theory and occurs with a shift in vibrational, rotational and electronic energy in the molecule. Energy exchange occurs between the incident photon and the molecule, resulting in either absorption of energy by the molecule and photon energy loss. The difference is determined by the different energies between the vibrational and rotational molecular energy levels.

Two modes of non elastic scattering are: Raman Scattering [54, 55, 56, 57, 58] and Brillouin Scattering [44, 59, 60, 61]. Both modes describe an almost identical process with the exception that Brillouin scattering is mainly used to describe the scattering process interaction with quasi particles such as phonons [60, 62, 63, 64]. Raman scattering finds application in identifying chemical structure by assessing the scattering attributed to the molecular vibration and transition. Two different forms of Raman Scattering exist in which the molecules gain energy (Stokes transition; raman scattering) or it looses energy (anti-Stokes transition) [65]. An illustration with elastic scattering is shown in Figure 2.2.

2.2.2 Scattering in Biomedical Application

The light scattering effect is applied to gauge various optical characteristics between different biological media, in particular with tissues [66, 67]. Observation of the light displacement in tissue could be interpreted to distinguish between normal and malignant tissue, aiding clinical diagnostic [63, 64]. The interaction of external stimuli (ie thermal variation, chemical infusion etc) with a biological specimen could be deduced and measured from the associated light scattering observation. One other important role light scattering plays is in drug evaluation [68, 69]. This is achieved via ascertaining the drug's contribution towards alteration in blood composition and resultant hemodynamics [70].

However, for tissue imaging, the scattering effect consitutes a nuisance. Pure

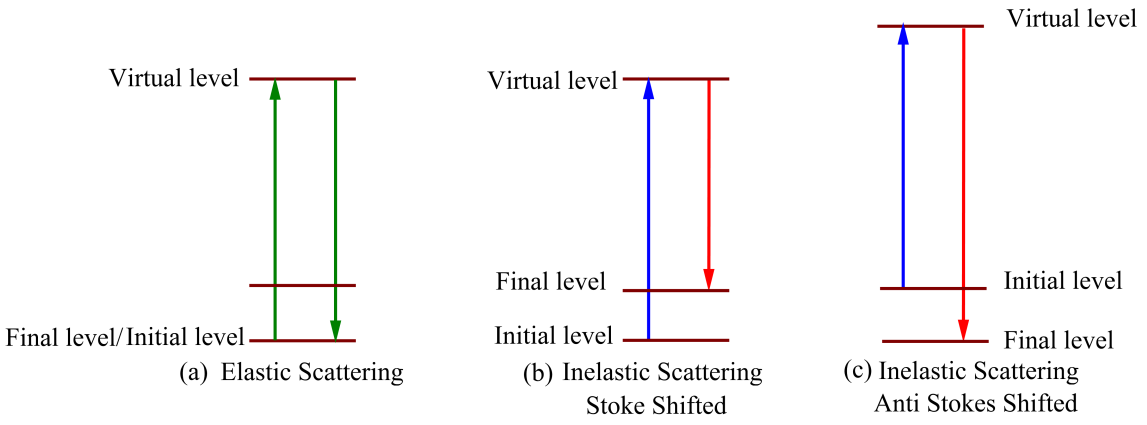

Figure 2.2: Comparison between elastic scattering with 2 different Raman scattering modes.
Diagram (a) Elastic scattering showing no energy loss (b) Raman scattering showing a molecular gain in energy (c) Anti Raman scattering denoting the loss of energy of a molecule.

optical imaging is currently hampered by shallow imaging depth [71, 72, 73]. A biomedical tissue sample typically has a thickness in the magnitude from tens of microns to several millimeters, which is comparable to the working distance of an objective lens. The ballistic light decays exponentially with respect to the turbid medium optical thickness, as scattering effects become dominant.

$$\text{Optical thickness} = (\text{Penetration Depth})/(\text{Scattering Mean Free Path})$$

Deep tissue imaging is highly susceptible to strong signal attenuation and resolution degradation. High resolution imaging with good SNR is frequently inhibited to 1 mean free path of depth [74]. In order to contend with absorption loss, light in the near infrared region is often employed at the expense of reduced resolution. Frequent employment of targeted biomarkers [75] and clearing agents [76] is required to improve contrast. Recovering imaging information with better spatial detail for subsequent image reconstruction remains a challenge. Despite the numerous forms of information optical imaging can offer (Section. 1.1.2), two core reservations linger in the development of optical imaging as a clinical modality:

1. How quantitative will optical imaging be? Will it allow for true quantification of the specimen under studies? What role should scattered light play in image reconstruction?

2. With the limited penetration depth, will optical imaging in humans be limited to tissues near the surface or to optical imaging utilizing various sensors that can be inserted into the body to image organs such as the prostate?

2.2.3 Scattering reduction method in optical imaging

Photon trajectories are often deviated from the original propagation path due to the presence of scattering centers. The photons eventually arriving at the detector could be demarcated into three regimes [45, 77]:

I Ballistic photons are photons that arrive at the detector undiverted.

II Snake photons which are photons slightly deviated from the ballistic photon path.

III Diffuse photons are photons which have been multiply scattered.

The assortment of photons from different regimes yields a general uncertainty as to which photons that arrived are from the intended imaged position. Superior quantitative measurement and diffraction limited imaging can only be realised with ballistic photons. However, useful information could also be gleaned with optical information from the diffusive regime, extending imaging limit up to several cm [78, 79, 80, 81]. For this thesis, we will restrict our studies to solely ballistic photon imaging.

The objective of ballistic imaging is to retain ballistic photons while at the same time discarding the non-ballistic ones. For ballistic imaging, the scattering reduction method could be classified according to how ballistic photon characteristic differences are utilised for the discrmination ballistic and non-ballistic photons.

Spatial filtering

A straightforward manner in which the diffuse and snake photons can be eliminated is via some form of spatial filtering. The technique capitalises on the notion that a deviant photon normally travels at higher spatial frequencies (ie angle) while a ballistic photon travels at a lower spatial frequencies. A form of low pass filtering, analogous to electrical signal processing, can be applied to remove the scattered photon thus preventing their access to the detector. Variants of the spatial filtering technique includes the use of a spatial collimating grid or a Fourier plane processing with a filter [82, 83] to eliminate the deviant scattered photons. A pinhole format of this spatial filtering method is shown in Figure 2.3.

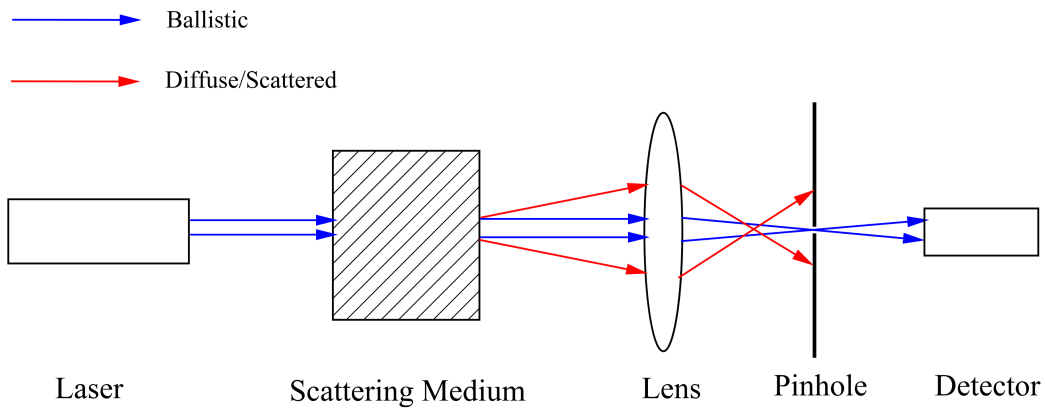

Figure 2.3: Spatial filtering with a pinhole.
A widefield configuration could be attained by placing an additional lens behind the pinhole, forming a 4-f configuration with the previous lens. The pinhole will reside in the common focal point formed by the two lens.

The confocal pinhole can be regarded as a variant form to this spatial filtering method. The detrimental effect of the scattered light to imaging is greatly ameliorated by the localised excitation of this microscope. In CM [84], photons originating from the co-localised spot formed by the illumination and detection objectives are utilised for image formation.

Time gating

Scattered light often travels a lengthier path to reach detector when compared to ballistic light. Hence temporal discrimination [85, 86] can be utilised to select early arriving ballistic light over delayed scattered photons. A time gate is employed to bar the entrance after a certain time duration (ballistic photon time of flight). As the time gates required a resolution of less than 1 ps, low coherence interferometry and nonlinear correlation techniques [87, 88] are often incorporated into the detection unit to alleviate the sensor temporal resolution constraint. Direct measurement with an optical detector [89, 90] would invariably acquire some snake photons due to the lower temporal responses. In order to overcome this shortfall, direct time gate detectors are augmented with nonlinear optical techniques such as the optical Kerr effect [91] and SHG [92, 93] (shown in Figure 2.4) to conduct 3 dimensional imaging.

An optical Kerr effect is induced when a strong light pulse is applied to generate birefringence in a Kerr material. An optical Kerr detector can be constructed by placing the Kerr material in between two crossed polarizers. An image-bearing signal will be directed through the setup but prevented from passing due to the crossed polarizers. When a reference (trigger signal) is applied, only the signal component which overlaps temporally and spatially with the reference will experience the polarization change due to brief birefringence and can pass through the final polarizer gate. In general, the reference signal is aligned at a small angle to the signal source and the laser trigger requirement warrants the use of high power femto second laser.

SHG time gate works through correlation technique. The reference beam and the sample beam are focused onto a KDP crystal and made to overlap in time. The diffuse beam is rejected while the ballistic beam is selected to generate an SHG signal with the reference beam. The SHG signal is subsequently collected by the detector. An advantage that SHG time gate mechanism has over optical Kerr gate lies in its lower energy expenditure.

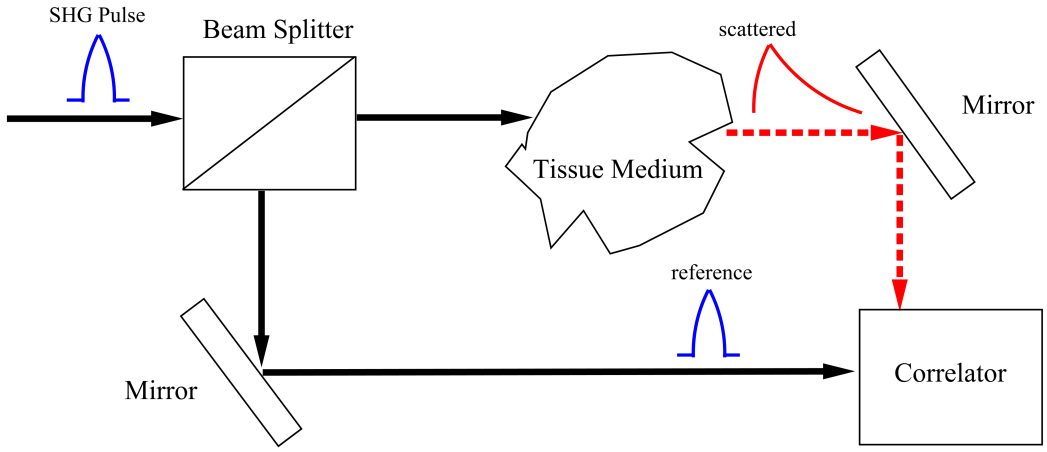

Figure 2.4: Time gating achieved with correlation with an ultrasharp pulse from SHG
SHG pulse broadens after passing through tissue medium. Correlation is done as a form of "ranging".

Coherence gating

The coherence properties of laser grant a potent technique to discriminate against scattered photons. After transmission through a turbid medium, ballistic light retains its coherence trait while scattered light loses its coherence and becomes incoherent [94, 95]. Coherence gating often depends on heterodyne detection [96, 97, 98] in the time domain, in that the weak unscattered light is preferentially selected amid the 1/f noise. OCT [28, 99] and coherence-gated holographic imaging [100, 101] are some prime examples in utilising coherence gating to preserve ballistic photons. Figure 2.5 illustrate a time domain implementation of the OCT concept.

Polarization gating

The polarization state of the photons is perturbed randomly after they undergoes scattering in a nonbirefringent scattering medium. Ballistic light component can be retrieved through an imaging technique known as polarization difference imaging [102, 103, 104]. In this technique, polarized laser light is transmitted through a linear polarization analyser after transversing through the scattering medium (shown in

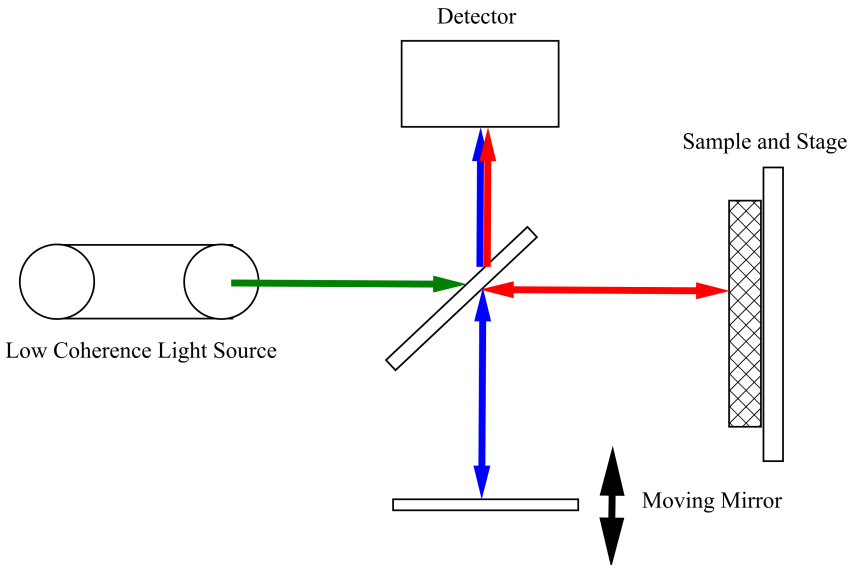

Figure 2.5: Time domain implementation of OCT
Moving mirror generates the variable phase delay and modulates the strength of the signal. Resulting signal has a Doppler frequency which is translated into fringes by the detector.

Figure 2.6). The ballistic signal is obtained through the signal difference captured through switching the analyser polarization state orthogonally.

2.2.4 Scattering effect modelling

The three forms of scattering described above provide approximate solutions that describe the scattering process. However, in a highly scattering medium, these solutions supplied are insufficient to illustrate the high recurrence of multiple scattering processes. Solutions derived from empirical observations [105] are solicited to provide an approximate answer for practical application.

One such approach is the description of the light scattering processes inside a turbid medium as a propagation of photons using averaged properties of the medium according to the radiative transfer equation (RTE). The RTE [106, 45] describes radiation inside tissue via the principle of conservation of energy and is formulated in as a differential equation or the Boltzmann equation. Energy loss in the form of

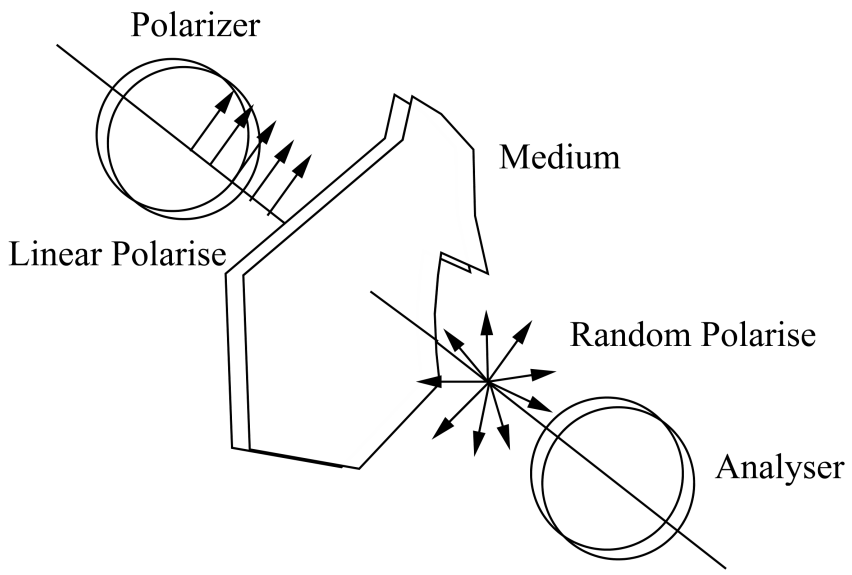

Figure 2.6: Polarization state after passing through medium.
Polarization state of analyser could be varied to obtain parallel/perpendicular signal by setting itself parallel/orthogonal to the polarizer. The difference between the two signals return the ballistic signal.

absorption or scattering away from the propagation path is balanced out by gain from scattering directed along the beam direction.

RTE poses a significant challenge for anyone to solve and simplification is performed to reduce the number of independent variables (about 6 of them) for a simplified problem. The diffusion approximation equation [107, 108, 109, 110] makes an assumption based on the following assumption:

i Scattering dominates the processes. There is little absorption and the use of diffusion approximation is restricted to highly scattering tissue.

ii Scattering events that occur are totally isotropic in nature.

iii Volume under consideration is far removed from the boundary and that changes in light density occurs much slowly than the photon movement time.

iv Any light source, and that photons reaching the photo-detector are time-independent.

Despite the various restriction, the diffusion approximation equation is popular because it allows for calculation over varied geometries. Finite elements can likewise be employed to solve the equation [111].

One last major approach taken by researchers is by using Monte Carlo simulation [112, 113, 114, 115, 116]. The Monte Carlo method simulates the processes described in the equation without resorting to the analytical transport equation or its simplified diffused approximation form. Monte Carlo is based on a stochastic model whereby the value of the physical quantity we are interested in is determined by the expected value of a certain random variable(s). Light propagation is regarded in the miniscule level by treating light as a mass of photons which is propagated in a random walk manner. One advantage of this method is that it allows one to deal with complex geometrical medium structure or optical system with ease. However, Monte Carlo simulation is prone to lengthy computation time which precludes its usage within a field analysis device.

2.3 Optical sectioning technique

The examination of biological specimen often necessitates the slicing up of the specimen into thin slices in order to prevent the out-of-focus layer's light from obscuring the desired image. This study process is known as histology [117] and would require lengthy sample preparation such as fixation and paraffin embedding before undergoing microtoming or sectioning to obtain the thin slices required. Biological study is constrained to the examination of chemically treated dead samples which inadvertently contribute to distortion of the anatomy. The advent of optical sectioning techniques [118, 119, 120, 121] spares the user from these lengthy procedures and allows living samples to be examined. Stray light interference (Figure 2.7 & 2.8) is either eliminated or minimised by these techniques, unlike in conventional widefield microscopy where the image is clouded by such noises upon defocus. In an optical

sectioning microscope, images simply darken and disappear upon defocus, granting greatly improved contrast. Depth discrimination is realised and 3 dimensional reconstructions [122, 123, 124, 125, 126] is enabled via using data from a stack of image frames from each layer. The 3D reconstructed image structure offers unprecedented insight to the cell morphology and functionality beyond what a conventional widefield microscope could accomodate.

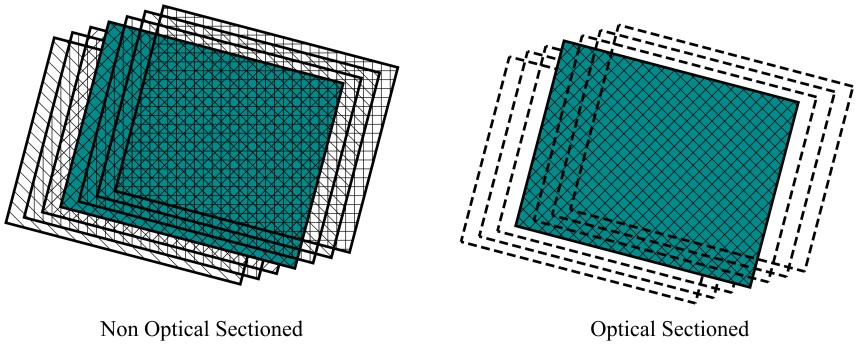

Figure 2.7: Comparison of Optical Sectioned and Non Sectioned Images.
In non-optical sectioned microscope, all planes contribute to the final image obtained while in optical sectioned microscope only the plane of interest is emphasize and contributes to image formation.

In general, optical sectioning technique could be divided into three different categories based upon various principles used to achieve the sectioning effect:

i Physical optical sectioning technique

ii Digital optical sectioning technique

iii Hybrid optical sectioning technique

2.3.1 Physical optical sectioning technique

The physical optical imaging method refers to optical microscopy techniques that leans on physical or optical property of light interaction to achieve optical sectioning.

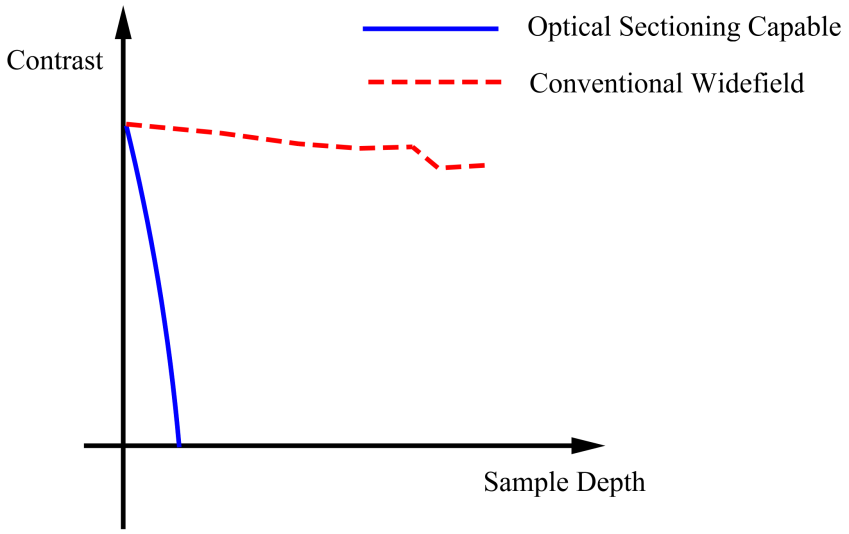

Figure 2.8: Optical sectioned and non sectioned contrast transfer function. OTF(Optical Transfer Function) of non-optical sectioned microscope transmit in all depth while in optical sectioned microscope only depth close to focal plane is transmitted without deterioration.

Method classified under this categories include confocal microscopy (CM), multi-photon microscopy (MPM) and optical coherence microscopy (OCM). A brief discussion will be given on the overview and distinction between each method. Deep tissue imaging performance and the corresponding shortfalls are evaluated.

Confocal microscopy

CM concept [12, 118, 126, 127, 128, 129, 130, 131] was first concieved by Marvin Minsky [132]. It relates a technique of focusing the excitation light onto focal plane and subsequently collecting the returning emission though precisely positioned apertures [131, 133, 134, 135] which physically reject light coming from out of focus regions of the sample. This entails the simultaneous focusing of both the excitation spot and pinhole aperture to the same spot. This focused spot is then rapidly moved through the sample via a scanning mechanism while maintaining in focus to both objectives. Hence the name "Confocal" is termed for the sharing of focal points.

In contrast to the conventional microscope, the light excitation and collection

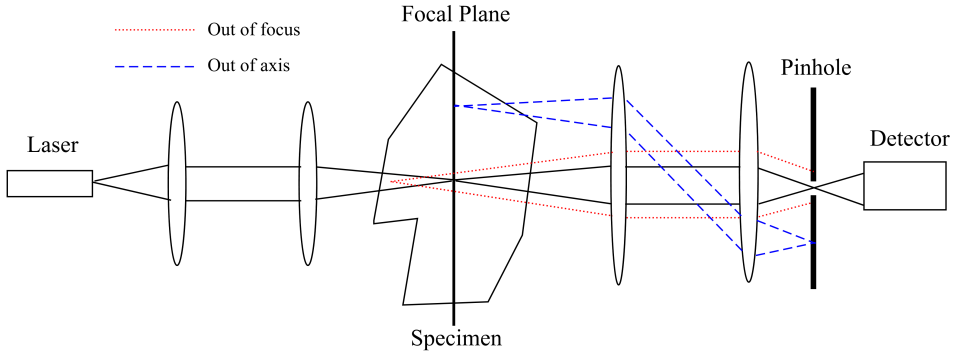

Figure 2.9: Confocal microscope and the filtering property of pinhole.
Out of focus(red-dotted) are being blocked by the pinhole. Only in focus light are being collected by the detector. Out of axis(blue-dashed) light do not really exist as it is not in the illumination path.

pathways are decoupled and independent from one another. The resultant system point spread function (PSF) is derived from the product of the excitation and collection PSF [12, 127, 131]. Henceforth, CM provides superior axial (≈1.05 times better) and lateral resolution (≈1.4 times better) [136, 137] compared to conventional microscope system. The ensuing point spread function could be expressed by the following relationship.

$$h_{eff} = h_{ill} h_{em} \tag{2.1}$$

The confocal microscope has often been considered as the "gold" standard in microscopy. The previous section 2.2.3 has suggested that the spatial filtering afforded by the pinhole helps to eliminate scattering [128, 138]. However, multiple scattered stray photons are not discarded completely and can leak through the pinhole [139, 96, 140, 141, 142]. Image contrast and SNR [143, 144, 145] erodes under elevating background level from increased multiple scattering when imaging deep tissue. This imposes a fundamental limit on the confocal microscope imaging depth [146, 147]. This problem cannot be straightforwardly corrected through increasing illumination throughput as there are practical sample exposure limits to high power illumination. Under the rising scattering effect, the pinhole size has to be reduced [96, 140] to

boost the spatial gating strength and to curtail spatial resolution loss. There is a reduction in the amount of collected signal that could be utilised for subsequent image reconstruction. An additional gating measure [148, 149] has to be devised to remedy the CM shortcoming.

Multi-photon microscopy

Multi-photon microscopy [25, 150, 151, 152, 153, 154] is a microscopy technique which relies on the property of multi-photon (or 2-photon) excitation and is practiced in the nonlinear regime. The multi-photon phenonmenon arises from the simultaneous absorption of two photons in a single quantitized event [155]. A laser with twice or multiples of the fluorophore's absorption wavelengths excites the fluorophore. As the condition for absorption time interval between consecutive excitation is short, the probability for this non-linear interaction is extremely minimal [156]. A femtosecond laser [157, 158] which has short pulse width, coupled with high focusing objectives, is then exploited to produce and fulfill the necessary high photon density and flux condition for two-photon absorption. Hence, fluorophore excitation is constrained to the focal spot where the criterion for two photon absorption could be satisfied. A spatial pinhole [159, 160, 161, 162] is not mandatory as the nonlinear interaction site acts as a virtual aperture for imaging. As there is little to nil two photon excitation at a non-focal interaction site, MPM has effectively diminished out of focus flare and a reduced photobleaching effect [127, 143].

MPM has a better penetration depth [163, 164, 165, 166] than CM as a longer wavelength (usually in the water window) illumination source is employed. Subsequently, the loss via absorption/scattering is reduced. With little or diminished out of focus flare, there is less background contribution from multiple scattered photons from non-interaction sites. However, TPEF excitation beam suffers from the same amount of scattering [26, 167, 168] when it transverses through the specimen. This may significantly reduce the TPEF signal at the focal point. Excitation point spread function broadening has been reported [24]. In the roundtrip, a secondary series of

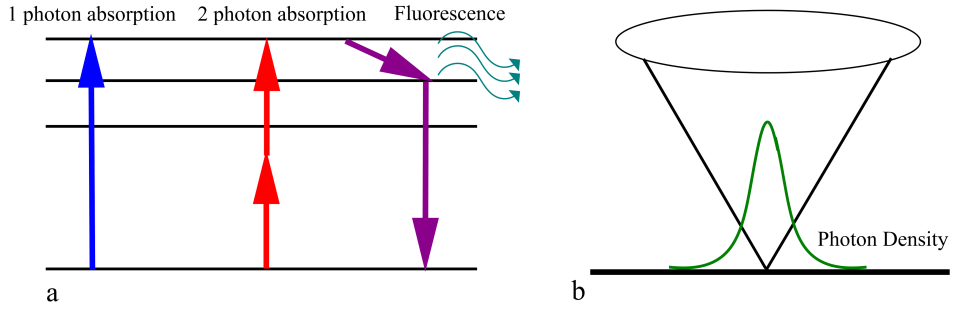

Figure 2.10: (a)Two photon excitation and (b)the requirement for high photon density

(a)Instead of absorbing a single photon to reach excitation level, two photon excitation simultaneously absorbed two photons at one excitation instance. (b) High photon density is required for MPM.

scattering deteriorates the returned fluorescence. Multiphoton microscopy has an inhibitory setup cost (in terms of laser cost) and is limited by the available fluorophores. In addition, heat damage often occurs with photon absorbing pigments in tissue.

Optical Coherence microscopy

Optical coherence tomography [14, 28, 29, 169] is an interferometric imaging method that offers millimeter penetration with improved axial resolution. It works through the principle of low coherence interference. A wide bandwidth white light source with low coherence length is engaged to achieve "coherence gating". Reference light and the back-scattered light from the specimen are brought to interfere at the detector. The interference contrast signal drops off significantly when sample and reference optical path length difference exceeds the coherence length. Hence OCT works well with low coherence light which enhances its axial cross-sectional selectivity. A reflectivity map (of varied intensity level) is produced, resulting from the interference effect. Various forms of the OCT are practiced in the time domain [170, 171, 172], frequency domain [173, 174, 175, 176] and full-field format [177, 178] and are depicted in Figure 2.11.

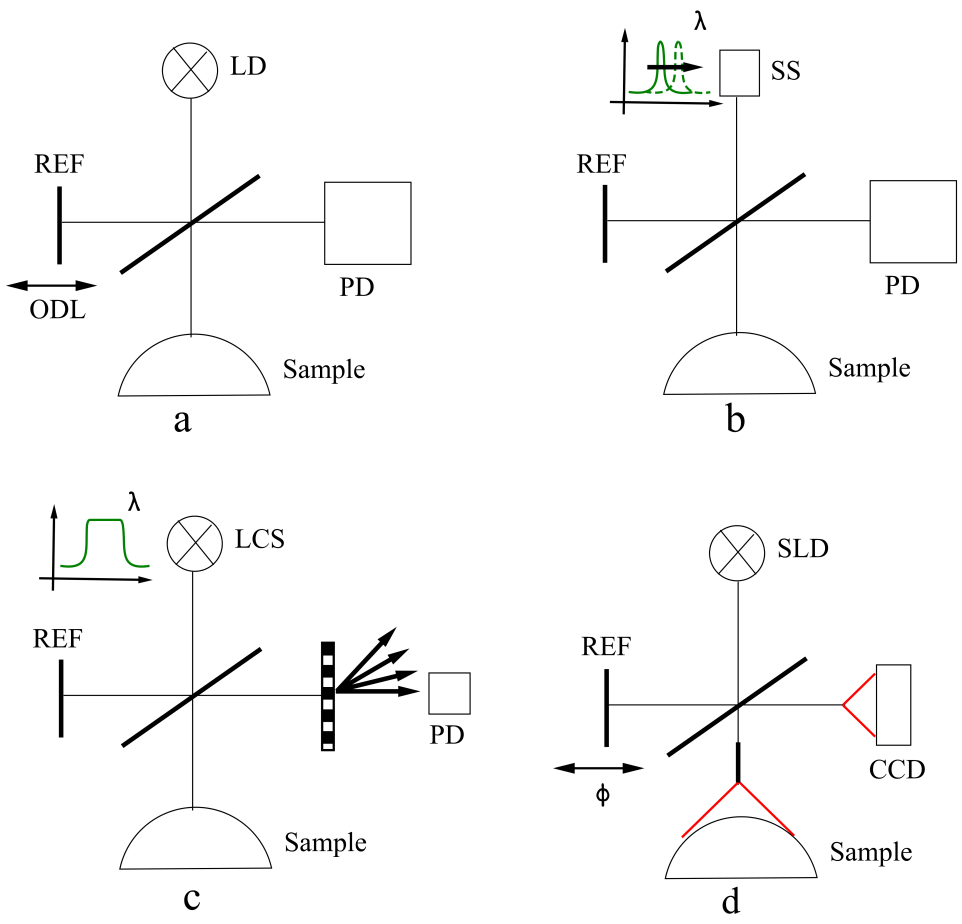

Figure 2.11: Various implementation of OCT

CCD - Charged Coupled Device, LCS - Low Coherence Source, LD - Laser Diode, ODL - Optical Delay Line, PD - Photodiode, REF - Reference & SS - Swept Source (a)Time domain OCT. Reference beam is modulated with a Doppler frequency f, and modulated intensity is collected and demodulated via scanning (b) Fourier domain OCT -implementation with a grating. Backscattering interferometry with a wide range of spectra is being sorted by a spatial grating and recorded via a CCD (c) Fourier domain OCT - implementation with a swept source. Instead of a grating, a fast changing wavelength source is used to achieve the former. Detection achieved by photo detector. (d) Full-field OCT. Somewhat similar to time domain OCT, reference is shifted through various phase. Individual pixel in CCD picks up the individual interference effect from the sampling point, demodulated by removing contribution from scattered component.

OCT has superior depth penetration, and high axial spatial resolution is maintained even for imaging of thick and highly scattering tissue [179, 180, 181]. The

coherence gating gives OCT a strong ability to selectively detect ballistic photons amidst back scattered light.[1] With the ability to render high quality 3D structural images even in deep tissue imaging, OCT is rapidly adopted into clinical imaging application such as in the eye [182, 183, 184, 185, 186], vascular tissues [187, 188] and gastrointestinal tracts [189, 190, 191].

However, like most scanning microscopy methods, OCT has to rely on complex and demanding setup for lateral fast scanning. Another drawback for OCT imaging is the inability to utilise fluorescence for imaging. OCT imaging solely provides physical information or the scattering coefficient of the biomedical specimen with scant detail to allow for in-depth functional study. Light's coherence is destroyed in the inelastic fluorescence excitation process. In addition, polarization and angular information is likewise lost in the process. With the dearth of a contrast agent, differentiation of tissue types becomes intractable with OCT while imaging morphologically or optically identical tissue types. For this reason, OCT [192, 193] is often deployed in combination with other imaging techniques in order to reveal "hidden" specimen spectroscopic information.

2.3.2 Digital optical sectioning technique

The deconvolution method [194, 195, 196] permits image refocusing via software based approach. Optical imaging can be viewed as a linear shift invariant operation (Figure 2.12). A point is not imaged directly to a point in image space but instead mapped to an extended space. In an imaging convolution process, the image obtained is undesirably smeared by out-of-focus contribution. Image-useful resolution is severely reduced and further exacerbated by deleterious noise eg. from scattering.

Deconvolution attempts to circumvent this process and reconstruct the specimen

[1] It is possible, however for OCT to detect quasi ballistic photons which could participate in interference. Quasi ballistic photons are photons which experience a small number of scattering events but with only a slight deflection from their trajectory. Due to the highly forward-directed scattering nature, the photons would still carry imaging information on the tissue optical properties. Certain amount of resolution could be obtained from quasi ballistic photon imaging in OCT.

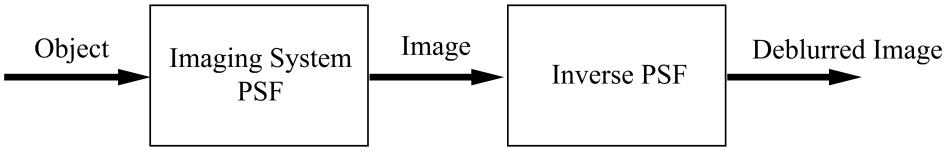

Figure 2.12: A simplified treatment cycle in deconvolution microscope.
An inverse PSF is used to retrieve the actual object from the blurring imaging process. External noise effect is not considered.

from a blurred image. Knowledge of the PSF is expedient to imaging characterisation and the blurring model. A precise PSF model can be gained either through experimentation [197, 198] or theoretical computation [198, 199, 200] to achieve optimum deconvolution result. Deconvolution algorithms can be grouped under two main groups: deblur and restorative. The main distinction between these two forms of algorithm rest in the way noises are treated by the algorithm. Restorative type algorithm extracts light from out of focused region and reassigns them to perform image clean up, while deblur algorithm simply discards such noises and retains only the in-focus portion. A comparison between the two algorithm types is shown in Table 2.2 below.

Types	Deblur	Restorative
Method	Blur is subtracted from experimental result with PSF knowledge	Image equation used to estimate objects
Algorithm	Constrained Iterative Approach. Fast and less computation intensive	Nearest Neighbour Approach. Slow and more computation intensive
Result	Higher contrast trade off with lower SNR	Conservational approach. SNR increase as attempt is made to deal with noise
Quantification	Only qualitative study is possible	Result can be used for quantification

Table 2.2: Differences between deblur and restorative deconvolution algorithm

The digital sectioning microscope possess the advantage of higher SNR, as it attempts to reassign out of focus light to its point of origin. In contrast, out-of-focus light is routinely discarded by the physical sectioning method ie CM. Consequently, digital sectioning microscope is capable of working with weak fluorescing object. However, the digital microscope necessitates lengthy setup time and is adverse to imaging strongly diffusive medium. More than often, a physical gating microscope [201, 202] is coupled with digital sectioning technique for imaging highly scattering sample. The deficiencies in imaging highly scattering tissue does little to promulgate this method's popularity in imaging thick tissue.

2.3.3 Hybrid optical sectioning technique

The hybrid optical technique is a breed of microscope technique that either relies on (i) both optical and digital sectioning technique or (ii) one that combine two complementing optical sectioning techniques into a single setup [203, 204]. Deficiencies in individual component microscopy techniques are compensated for the latter variants. The current discussion will direct the attention to the former hybrid optical sectioning definition.

One hybrid technique that has seen rising popularity in the recent years is known as structured illumination microscope (SIM) [205, 206, 207, 208, 209]. Usage of structured light is not uncommon and is often utilised in interferometry testing and surface topology [210, 211]. However, the technique implemented in microscopy setting is slightly different. The technique depends on the optical property that a grid pattern is imaged in strength onto the in-focus plane, or conversely that solely the in focus plane is rigourously modulated by an projected grid pattern. In contrast, the out-of focus image contribution is merely mixed with a smeared image of the grid pattern which contributes wholly to the average intensity and does little to alter spatial details.

A few distinct forms of structured illumination are practised for diverse goals [205, 208, 212] with moderately varying acquisition and processing methods [213, 214]. For

a general SIM, gratings are spatially shifted and projected onto the sample (Figure 2.13) to obtain 3 phase shifted stripes modulated images. Subsequent digital processing eliminates the background blur and retrieves the optically sectioned images.

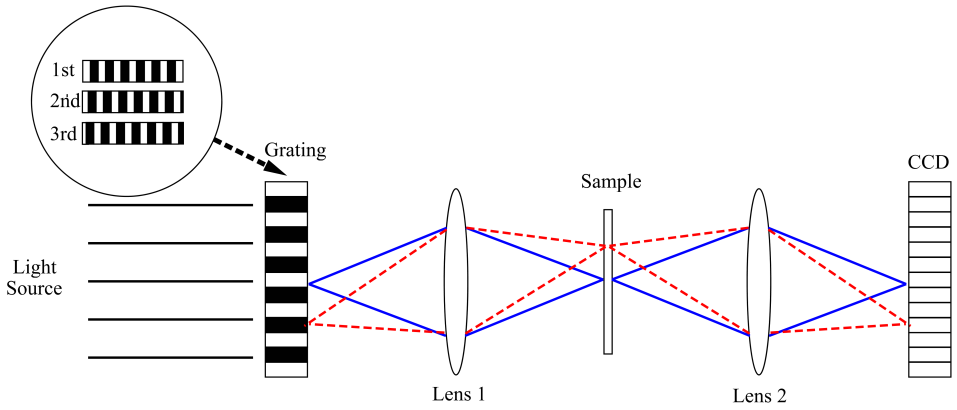

Figure 2.13: Conventional SIM implementation via moving grating.
Grating is shifted by a $\frac{\pi}{3}$ period and is projected onto the image. The image interlaced with stripes is captured by the CCD. A successive of 3 images are required for processing to obtain optical sectioned image.

Under minimal scattering condition, SIM demonstrates higher SNR and faster acquisition speed over conventional physical sectioning methods such as CM [215, 216]. This is attributed both to the adoption of a CCD (higher QE) for imaging as well as the wide-field nature of acquisition (faster speed and higher signal). In addition, SIM offers reduced setup complexity and cost over CM, MPM or OCT. However, with increased scattering while imaging in turbid medium, SIM performance is severely degraded as it primarily behaves akin to that of a conventional microscope [217]. SIM makes little or no effort in rejecting out-of focus light, making it an unsuitable candidate for deep tissue imaging.

2.3.4 Comparison between optical sectioning methods

The disparity between different forms of microscope is summarised in the Table 2.3 below. From the table, despite the fact that the physical sectioning method has lower acquisition speed and poorer SNR, the physical sectioning method commands deeper imaging capability. The physical sectioning method directly attempts to eliminate or reduce scattering unlike the digital and hybrid method. Among the physical sectioning methods discussed, coherence gating with heterodyne detection offers the best prospect in enhancing imaging depth.

	Physical			Digital	Hybrid
	CM	MPM	OCT	Deconvolution	SIM
Speed	Slow	Slow	Slow	Fast[1]	Moderately Fast
Cost	High	Very High	High	Low	Low
Light Efficiency[2]	Low	Very low	Low	High	Moderate
Imaging depth	≈100-200um	400-600um	Up to 1mm	<100um	<100um
SNR[3]	Low	Moderate	Moderate	High	High

Table 2.3: Differences between deblur and restorative deconvolution algorithm.
[1] Acquisition time discount the time required for calculation of PSF.
[2] Light Efficiency refers to the amount of light that is utilised for imaging.
[3] SNR in the absence of noise such as scattering.

2.4 Noise & detector

Scattering has a detrimental influence upon microscope system performance. There are two other major noise sources in an optical system: optical noises and detector/electronic noise. The former relates to noise contribution from misaligned optics, surface reflection and stray light noises which could be eliminated or mitigated with

corrected optical light path and anti-reflection coating. The latter noise source is associated with the detectors and electronics deployed in recording the measurement signal. A working knowledge on detector modules with their associated detector noise contribution is essential for any microscopist.

2.4.1 Detector system

The general detector signal generation in an optical system is described by the equation accompanied with the flow diagram in Figure 2.14 below [218].

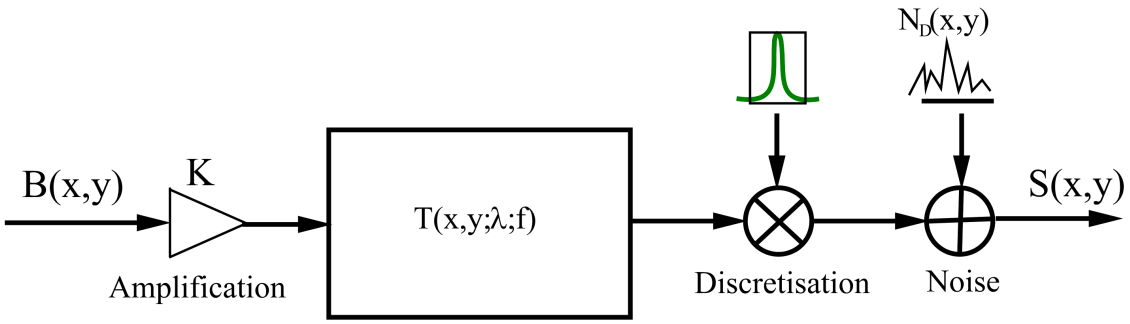

Figure 2.14: Signal flow diagram in optical detectors
Input signal(light) is given by B(x,y) and is convolved with the spatial frequency response of the detector $T(x, y; \lambda)$, assuming a linear response between the detector and input light signal. K gives the signal amplification factor. $N_D(x, y)$ gives the noise expression for the detector. Discretisation is characterized with the comb function to denote the scanning or the equivalent detector array function.

A biological microscopy system has to operate routinely in low light levels. On the other hand, a fluorescence microscope would have to contend with the bleaching problem if operating under high power exposure over prolonged periods. This restricts the exposure level or laser power that one could input to generate a signal. Detectors with high sensitivity and low noise behaviour are therefore instrumental in obtaining satisfactory SNR for deep tissue imaging. The amount of signal collected is determined by the light conversion efficiency as well as the detector area. The former

is dictated by the detector material used and is varied by the associated bandwidth. Signal quantity increments with the detector size at an expense of lower spatial resolution. Various detector parameters which are critical in the choice of detector are laid out in Table 2.4 below.

Parameter	Remarks
QE, Quantum efficiency	Energy from incoming photon is used to release an electron its electronic bond to supply to the free electron flow. The percentage in which the electron is released is known as quantum efficiency.
Sensitivity	Expressed as (V/W) in most data sheet to denote the amount of optical power to incite a voltage response. Gives a measurement of how small a signal input is detectable
Detector size	Large detector size increase signal collection but at a cost of lower spatial resolution
Spatial resolution	Inversely proportional to the detector size. Determines signal resolution based on Nyquist theorem
Linearity	A detector is considered linear if its response towards signal is given by product of input and a constant: Output = K ×Input. Necessary parameter for quantification study
Time response	The rate of the detector response towards signal. Essential for measuring rapid changes in experiment, especially in FLIM. Sometimes it is defined in terms of rise time
Dynamic range(DR)	Ratio between the highest and the lowest possible detection range. Define the range of detector operation
Noise	Noise generated by detector electronics and usage. Generally stated as NEP in data sheet. Detector shunt resistance and dark current are sometimes stated as alternative measurement of the same parameter
SNR	Sometimes referred to as detectability. The measurement of the ratio of signal to noise ratio relates the capability to differentiate signal from noise

Table 2.4: Detector parameter

For deep tissue imaging, despite the low quantum efficiency, the PMT remains the prime choice for detectors selection [127, 219, 220, 221]. The PMT offers higher sensitivity due to the photon multiplication effect, enabling it to generate and extract appreciable voltage differences with minute fluctuation in photon numbers. Little to no Johnson noise is associated with PMT operation making it immune to variance in operation temperature. However, PMT is still afflicted with shot noise. For low light measurement, careful design of PMT is demanded to reduce dark current generated in PMT operation.

However as depth imaging becomes increasingly reliant on NIR light, PMT usage becomes a challenge. PMT spectrum responsivity drops drastically for wavelengths beyond visible light. The main reason for such behaviour lies in the poor photocathode quantum efficiency. The PMT advantage over CCD is less distinct at low NIR light level as CCD quantum efficiency remains high for wavelength up to 1100nm. However, PMT's excellent time resolution means that it continues to be the prime choice for experiments which features fast signal variation with low photon count.

2.4.2 Noise

In general, photon limited microscopy [220, 221] is challenging in practice, as noise undermine the sensitivity (SNR) and the dynamic range of the microscope system. It is therefore essential to understand the nature of individual noise components and their contribution in order to utilize an equitable strategy to mitigate their deleterious effect. Noise in a detector system can be classified according to the following in Table 2.5.

Typically, three types of noises are of primary concern in any implementation of optical microscopy [222, 223, 224] technique/instrumentation comparison namely, shot noise, thermal noise and dark current. No detector is immune to shot noise. Hence the "holy grail" of every optical detector system is to attain shot noise operation via complete elimination of thermal noise and dark current. The former can be mitigated with reduction in operation temperature or utilization of low energy

Parameter	Remarks
Shot Noise	Quantum noise or shot noise is the result of the Poisson random statistics of discretely arriving photon resulting in signal reading fluctuation. $I^2_{shot} = 2qI_{DC}\Delta f$
Flicker Noise	Flicker noise is a partially understood phenomenon. A simple model suggested that flicker noise is the statistical product of spontaneous external photoeffect emission and internal photoeffect recombination in the semiconductor devices. Flicker noise is closely related to the DC signal supplied and has a 1/f noise spectrum. Could be minimized with lower supply power.
Fixed Pattern Noise	Fixed pattern is related to the detector architecture and refers to the uniformity of detector for the former. Could be reduced with careful design of detector/system architecture.
Read out Noise	Noise produced through the transferring of charge carriers. Could be reduced with careful design of detector/system architecture.
Dark Current Noise	Reverse bias current leakage due to randomly generated charged carrier by high reverse electric field gives rise to dark-noise $J_{dark} = J_0.T^2.e^{-\Delta E/k_BT}$
Thermal Noise	Thermal noise is generated via thermal agitation of the electrons and occurs at any reference voltage with a noise voltage. $\langle U^2_R \rangle = 4k_BTR$
Amplifier and Quantization Noise	Amplifier and quantization noise refers to post processing associated noise. This noise could often be mitigated with the usage of quality amplifier and ADC.

Table 2.5: Noise classification

Parameters: ΔE - work function, Δf - bandwidth over which noise is measured, I_{dark} - dark current, I_{DC} - average current, I_{shot} - shot noise current, J_o - nominal signal current, k_B - Boltzman constant, q - elementary charge, U_R - noise voltage

consumption devices while the latter can be minimized with add-on circuitry and carefully designed and laid-out architecture [225, 226].

Chapter 3

Theory of focal modulation microscopy

3.1 Organisation

The chapter begins with an intuitive explanation towards the theory of focal modulation, aiding the layman to acquire an implicit understanding and appreciation for this method simplicity and elegance. A brief review on lens and confocal theory which formulate the theoretical derivation of the focal modulation microscope will be presented. Investigation using scalar diffraction theory will then be used to formalise the theory in the next section. The transfer function as well as the intensity point spread function will be evaluated subsequently. The influence of the pinhole on Focal Modulation Microscopy (FMM) will be discussed.

3.2 An intuitive approach towards focal modulation

The main innovation behind the focal modulation approach is to capitalize on the ballistic light coherence property to extract solely the unscattered signal contribution from the focal volume. The split field approach manipulates the excitation beam

to generate focal region intensity modulation. The resultant fluorescence emission from this region has an ac component with the corresponding modulation frequency attributed to the ballistic photons. Such modulation would be absent from the background signal generated by the scattered photons. The fluorescence signal is collected via the collection lens through a pinhole, analogous to the confocal microscope detection path. Only the main lobe intensity fluctuation is detected. Utilising the fourier transform signal processing technique, the modulated signal can be extracted from the collected signal spectrum. Since the origin of the ac signal is confined within a small volume defined by the ballistic excitation light, the resolution and contrast can be retained for a greater imaging depth than confocal microscopy. In a way, focal modulation microscopy can be regarded as a combination of coherence gating (provided by two beam interference) with spatial gating (via the pinhole). The method described could be summarized by Figure 3.1 below.

One simple pupil function we can adopt is the annular shaped function in which the center portion is phase modulated. The pupil function could be parameterized by the radial value a and b:

$$P(r) = \left\{ \begin{array}{cc} exp(-i2\pi ft) & if \quad r \leq a \\ 1 & if \quad a \leq r \leq b \\ 0 & otherwise \end{array} \right\} \tag{3.1}$$

The focal intensity attained by the modulation (in-phase, 90°, 180° & 270° out of phase shift) is simulated with Matlab [227] and is depicted in the Figure 3.2 below. By further restricting the intensity selection region to the central lobe and detecting its variation, we can detect a specific ac signal which varies with the corresponding excitation modulation frequency (Figure 3.3). The signal from the scattered photons can then be rejected accordingly using a band-pass filter.

The benefit of this selective excitation property could likewise be extended towards imaging in a turbid medium. With the focal point of the microscope positioned within the turbid medium, both the ballistic photons and scattered photons contribute to

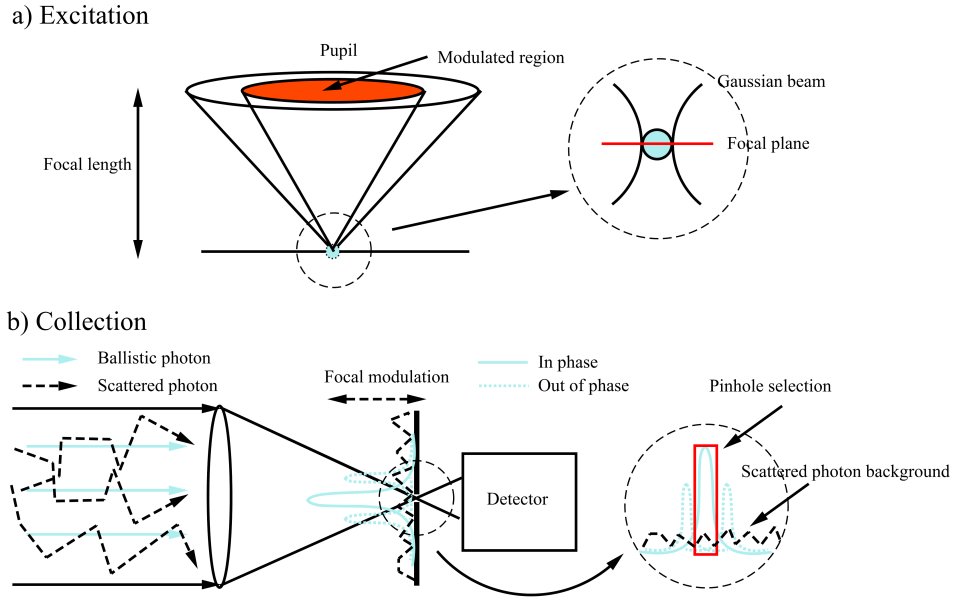

Figure 3.1: Method of focal modulation.
(a)Excitation pathway: In the pupil plane, a segment(annular for this case) is modulated. Via the focusing property of objectives, the modulation is restricted to the blue shaded region(as shown in the inset). The rest of the region is unmodulated (b)Collection pathway: Both ballistic and scattered photons are focused to the pinhole. Only the main lobe region is collected while the side lobes are spatially filtered off. The collected signal consists of ballistic and scattered photons. The former is retrieved for FMM image formation.

the excitation of the fluorescence particles. However, only ballistic photons, and to a certain extent quasi-ballistic photons, can interfere to produce an excitation signal with the modulated frequency. Fluorophores excited by this modulated excitation frequency will reemit the fluorescence signal linked to the corresponding excitation frequency.

3.3 Foundation theory

This section introduced some basic concepts in diffraction and extends it to give a basic description for lens imaging via linear system theory. Lens imaging theory subsequently aids in the development on the principle and theory behind CM imaging

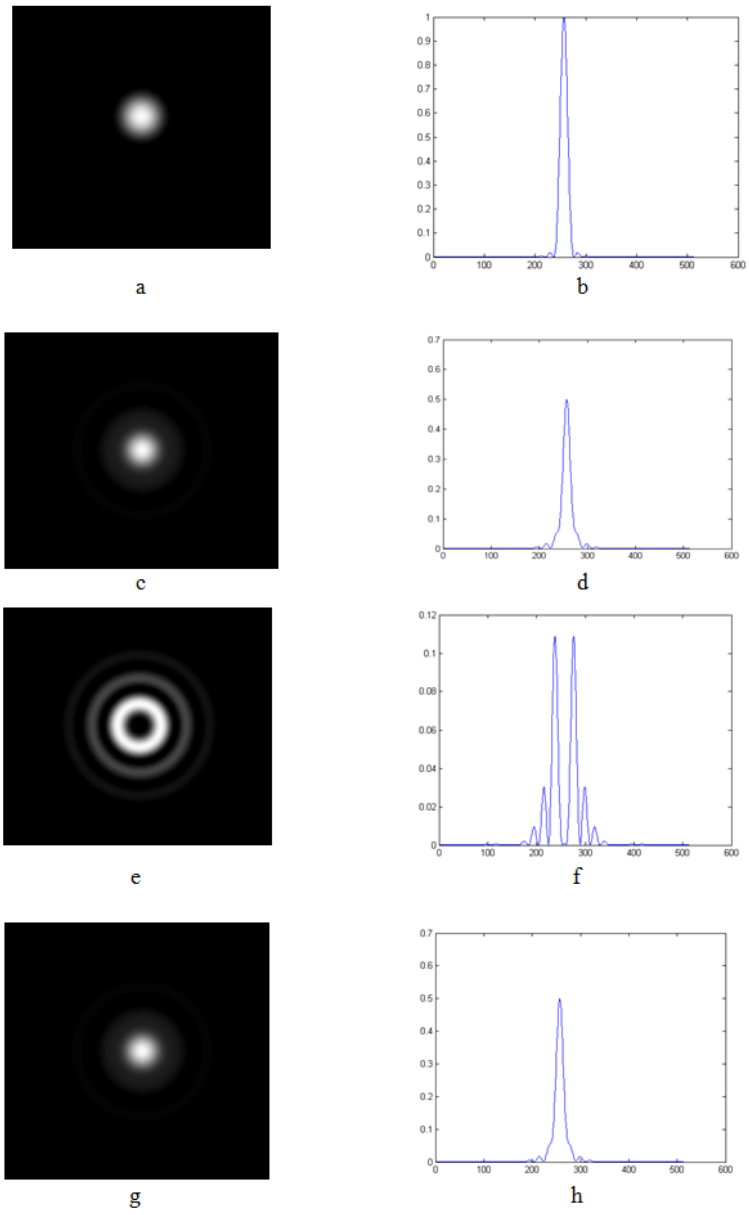

Figure 3.2: MATLAB focal plane intensity simulation result.
Simulation is based on a circular aperture and 2D intensity diagram and their respective cross-sectional intensity profile are shown for 0°(a,b), 90°(c,d), 180°(e,f) & 270°(g,h). Simulated 2D intensity diagram are normalised by a logarithmic function to clearly display the image while the cross-sectional intensity profiles are normalised by the maximum intensity from the 4 images to provide a comparison.

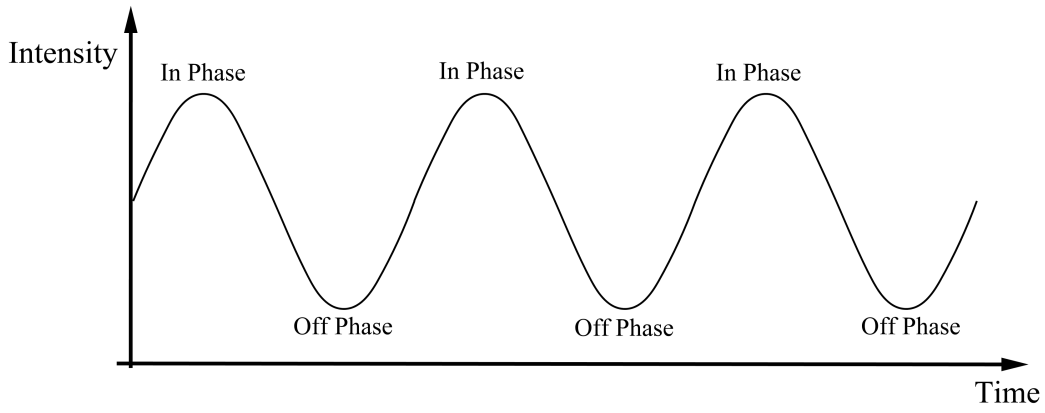

Figure 3.3: Hypothesized signal readout from FMM.
By training the detector on the main lobe, using the pinhole to remove signal from side lobes, sinusoidal signal readout can be obtained with the same frequency as the modulation rate of the pupil. The signal cycles from maximum to minimum in correlation to pupil in phase and off phase state.

theory. CM is antecedent to a number of optical sectioning microscopy such as MPM & 4 Pi and similar theoretical treatment of the former is used to derive the latter governing imaging theory. Likewise, a similar approach will be taken in expressing FMM in next section, using ground works laid in this section.

3.3.1 Diffraction theory

Geometrical optics presents a rudimentary method to understand imaging. However, geometrical optics breaks down when its assumption of near-zero wavelength fails and is altered whenever travelling light meets an obstacle. Likewise, the distribution of light near the focal region is not considered ideal because of light diffraction and has to be evaluated rigorously by a diffraction formula [228, 229](Figure 3.4). From Maxwell's equations, a scalar solution to the diffraction problem is developed by applying appropriate boundary condition, such as the Kirchhoff boundary condition. Other descriptions of the diffraction effect are construed likewise via knowledge of the incident wave distribution and its derivative.

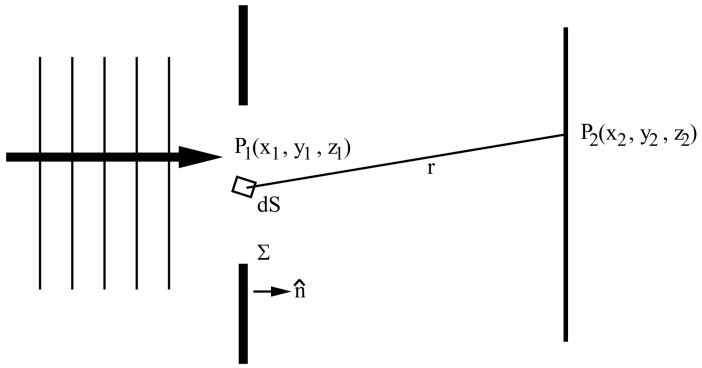

Figure 3.4: Diffraction at an aperture.
$U(P_1)$ & $U(P_2)$ are the amplitude at the aperture and the observer plane output respectively.

$$U(P_2) = -\frac{i}{\lambda}\iint_{\Sigma} U(P_1)\,\frac{exp(-ikr)}{r}\cos(\hat{n},\hat{r})\,dS \tag{3.2}$$

where $\hat{n}, \hat{r}$ are the normal and directional unit vectors respectively and r is the distance between the aperture point P_1 and the screen point P_2. Applying the paraxial approximation ($\cos(\hat{n},\hat{r})$ being set to unity and r replaced by z, the distance from the aperture to screen along optical axis) and constraining our study to points or regions near the optical axis, the above solution is greatly simplified. In the case of general microscopy, a further approximation, the Fraunhofer approximation, assumes the observation point to be in the far field and allows the Fourier Transform to be utilised in diffraction analysis. A diffraction pattern is merely the Fourier Transform of the input light distribution at the aperture coupled with a nonlinear phase term:

$$U(x_2,y_2) = -i\frac{exp(-ikz)}{\lambda z}\iint_{-\infty}^{\infty} U(x_1,y_1)\,exp\left[\frac{ik}{z}(x_2x_1+y_2y_1)\right]dx_1dy_1 \tag{3.3}$$

with z being the distance along optical axis from aperture to screen. Detailed treatment of the diffraction effect can be found in [229, 131].

3.3.2 Lens imaging theory

Fraunhofer diffraction theory simplifies diffraction calculation and allow for the introduction of Fourier Transform theory to efficiently calculate the observed diffraction pattern. The observation plane is however required to be located at infinity. The introduction of the lens however allows one to focus the light onto a plane and obtain the Fraunhofer diffraction pattern.

Therefore a lens behaves like a spatial fourier transformer that transforms a spatial domain signal into a spatio-frequency domain signal. The transmittance $T(x, y)$ or the aperture light distribution of the single lens is modelled in Figure 3.5.

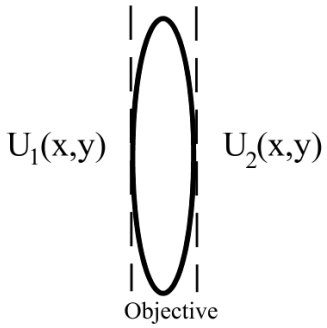

Figure 3.5: Lens as a transmittance function.
$U_1(x, y)$ & $U_2(x, y)$ are the input and the output respectively.

$$T(x, y) = P(x, y)\, exp\left[-j\phi(x, y)\right] \tag{3.4}$$

with $P(x, y)$ & $\varphi(x, y)$ describing the amplitude and phase function respectively according to the lens geometry in Cartesian coordinates (x, y). The paraxial approximation is utilised to provide a reduced interpretation via the more familiar geometrical optics analysis. The thin lens complex function is reinterpreted as [131]

$$T(x, y) = P(x, y)\, exp\left[\frac{jk\,(x^2 + y^2)}{2f}\right] \tag{3.5}$$

The Fourier Transform treatment of the diffraction effect introduces another associated property "linearity", which can be exploited for rapid calculation of the focal profile. The associated lens imaging operation can be treated as a space invariant, linear operation. This treatment provides an efficient and familiar means to describe the diffraction effect produced by the lens as described by Figure 3.6.

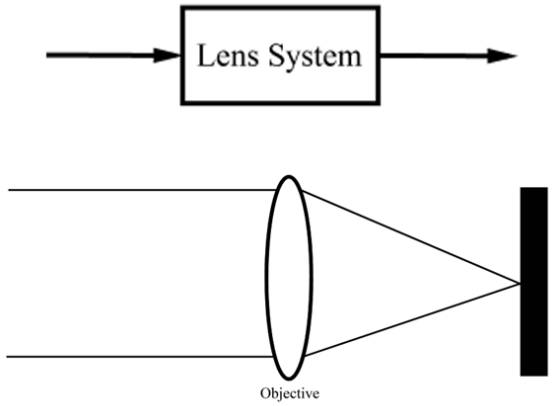

Figure 3.6: Lens imaging operation treated as linear system operation.
Adoption of paraxial assumption allows the diffraction effect produced by lens system to be regarded as linear system operation. This approach enables Fourier theory and transforms to be employed for analysis.

A detailed treatment of diffraction in terms of Fourier Transform can be found in [228]. For a general imaging expression, as in the defocused case, the circular lens PSF [131] is given by

$$h\left(x_2, y_2\right) = \iint P\left(x, y\right) exp\left[\frac{-jk}{2d_1}\left(x^2 + y^2\right)\right] exp\left[\frac{jk}{2d_2}\left(x_2 x + y_2 y\right)\right] dxdy \qquad (3.6)$$

where (x_2, y_2) & (x, y) describes the spatial coordinates in the image and pupil planes respectively. d_1 & d_2 represents the distance between source to lens and lens to image plane respectively. Essentially the equation describes the 3D image of a point

described by the parameters: x, y and defocus distance. Assuming circular symmetry, the above notation can be reduced to

$$h(\nu,\mu) = \int P(\rho) J_0(\rho\nu) exp\left[\frac{-j\mu\rho^2}{2}\right] 2\pi\rho d\rho \tag{3.7}$$

The parameter ρ is the normalised pupil radius $\left(\rho = \frac{r}{a}\right)$ and a is the pupil radius while ν, μ are optical coordinates and are given by

$$\nu = kr\sin\alpha \qquad and \qquad \mu = 4krsin^2(\alpha/2) \tag{3.8}$$

3.3.3 Confocal microscope imaging theory

The key differences between a CM (Figure 3.7) and conventional microscope lies in three aspects: (i) point source (ii) point detector (formed by a pinhole mask) & (iii) scanning system. A scanning microscope does not necessarily form a CM but a scanning microscope coupled with (i) & (ii) will form what is known as a Type II scanning microscope or CM [12].

CM imaging is a coherent process and strong optical sectioning property is demonstrated. Unlike the conventional microscope, CM illumination and the detection pathway of a CM are independent from one another. Therefore the image point formed is given by

$$\begin{aligned} U(x_2,y_2) &= \iint_{-\infty}^{\infty} \delta_S(x_0,y_0) exp[ik(z_0-z_1)] h_i(M_1x_1+x_0, M_1y_1+y_0) \\ &\quad \times o(r_s-r_1) exp[ik(-z_1-z_2)] h_d(M_2x_2+x_1, M_2y_2+y_1) \\ &\quad \times \delta_D(x_2,y_2) dr_0 dr_1 \end{aligned} \tag{3.9}$$

Where $h_i(M_1x_1+x_0, M_1y_1+y_0)$ & $h_d(M_2x_2+x_1, M_2y_2+y_1)$ denotes the illumination and detection point spread function respectively and can be obtained from

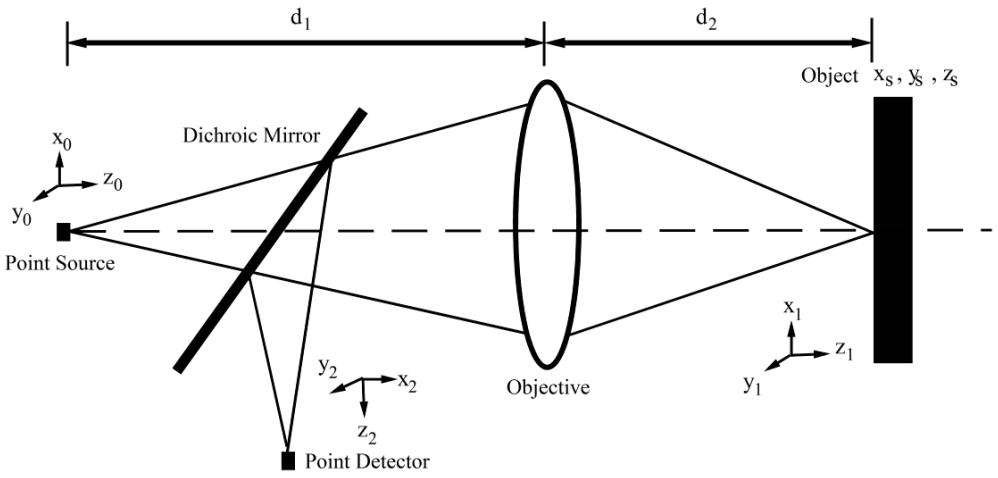

Figure 3.7: Schematic diagram of a reflection confocal microscope.
$r_0 = (x_0, y_0, z_0)$, $r_1 = (x_1, y_1, z_1)$ and $r_2 = (x_2, y_2, z_2)$ represent the positions in the illumination, object and collection space respectively. The scanned point has its coordinates given by $r_s = (x_s, y_s, z_s)$.

Eqn. 3.7. $M_1 = \frac{d_1}{d_2}$ & $M_2 = \frac{d_2}{d_1}$ refers to the magnification. By taking the source $\delta_S(x_0, y_0)$ as a point source, and the detector $\delta_D(x_2, y_2)$ as a point detector with no offset, the imaging equation can be expressed under linear system theory as

$$U_2(\nu, \mu) = [h_i(\nu, \mu) h_d(\nu, \mu)] \otimes o(\nu, \mu) \tag{3.10}$$

v, u in this case is measured in the scanning space [131] and calculated by Eqn. 3.8. Likewise, the equivalent point spread function within the square bracket $h_i(\nu, \mu)$ & $h_d(\nu, \mu)$ denoting the illumination and detection point spread function respectively in optical coordinates.

The fluorescence imaging process is however incoherent. The difference between the coherent and incoherent CM imaging process is subtle and is manifested through the linearity of the imaging operation. An incoherent system is linear in intensity

while the coherent system exhibit amplitude linearity. CM fluorescence imaging corresponds to incoherent imaging process; the intensity point spread can be represented by the analytical expression.

$$h_{cm}(\nu,\mu) = |h_i(\nu,\mu)|^2 |h_d(\nu,\mu)|^2 \tag{3.11}$$

Substituting Eqn. 3.7 into Eqn. 3.11, we obtain the following figure Figure 3.8. A narrower FWHM is observed for CM over the conventional microscope, indicating a sharper lateral and axial PSF.

The introduction of the pinhole provides an additional "gating effect" and offers CM a distinct edge over the conventional microscope, providing superior axial and lateral resolution in addition to the optical sectioning capability. An infinitesimal pinhole is considered for the derivation of the above result. In practice, a finite sized pinhole is employed, and in addition affects the resolution and optical sectioning strength [133, 134].

CM's OTF is likewise given by the Fourier Transform of the PSF given in Equation 3.11,

$$\begin{aligned} H_{cm}(t,w) &= F\{h_{cm}(\nu,\mu)\} \\ &= F\left\{h_i(\nu,\mu)^2 h_d(\nu,\mu)^2\right\} \end{aligned} \tag{3.12}$$

t & w are the normalised lateral and axial spatial frequencies in Eqn. 3.8. The corresponding CM's OTF is then given by the Figure 3.9 and is compared with the conventional microscope's OTF.

From the OTF in Figure 3.9, the dearth of optical sectioning ability in the conventional microscope is self-evident. Information is not transmitted in the axial direction,

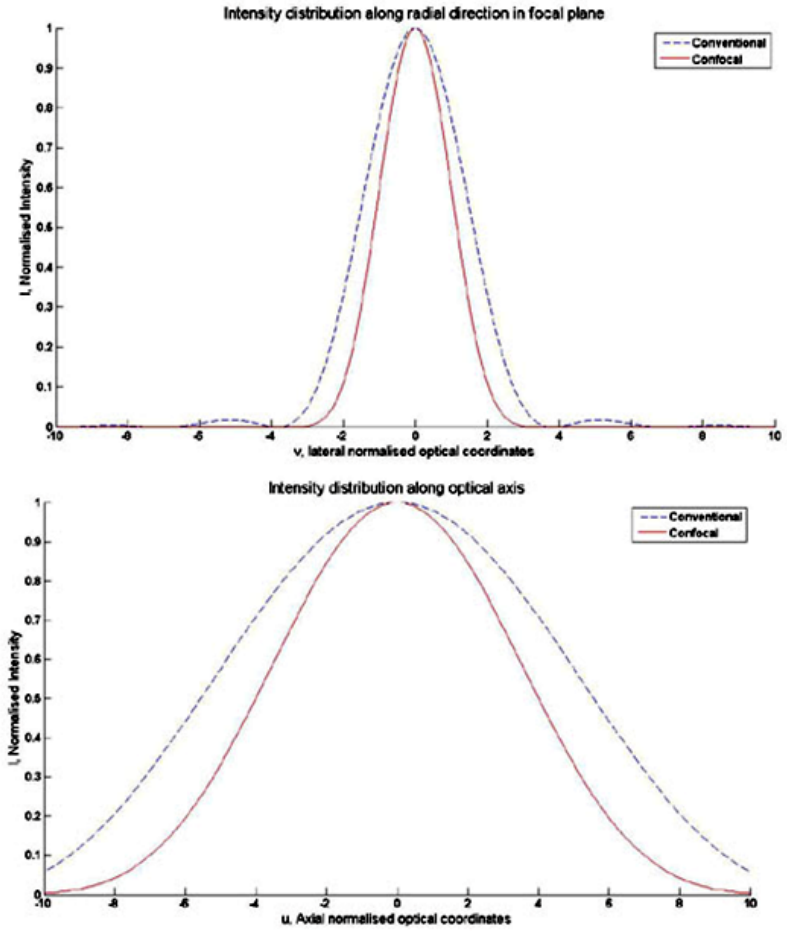

Figure 3.8: Intensity distribution of the confocal and conventional microscope in the lateral and axial direction.

The confocal microscope shows a thinner spread function in both the lateral and axial direction which translate to better resolution in both direction respectively.

suggesting the deficiencies in distinguishing information through the object layers beyond the focal plane.

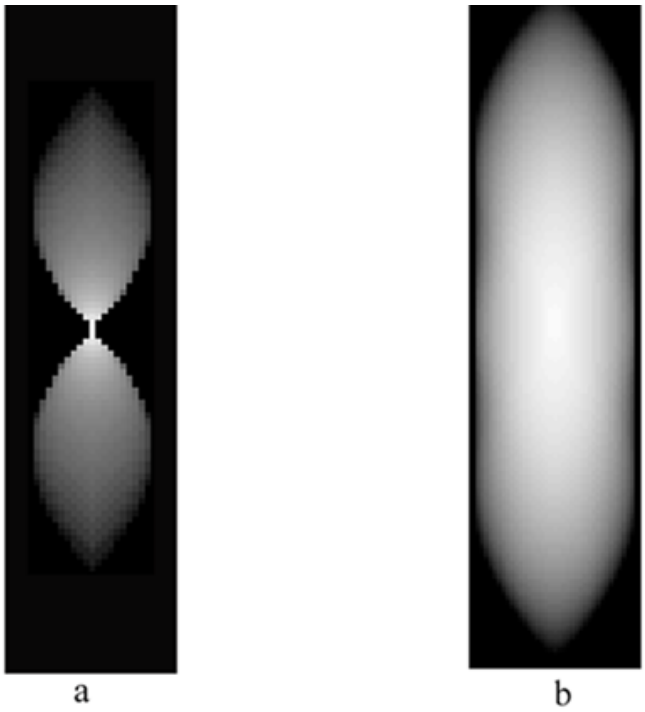

Figure 3.9: CMs vs conventional microscopes OTF.
Conventional microscope(a) exhibits a "missing cone" in the axial frequency direction. This suggests that the conventional microscope is not particularly suited for axial imaging since no information is passed by the OTF. This missing information set is however passed by CM's OTF(b) as traced by the red outline in the figure.

3.4 FMM theory

The FMM schematic diagram is presented in Figure 3.10, to investigate the focal modulation effect on imaging process. The fundamental difference between CM and FMM microscope lies in the manner the sample excitation field is achieved. In FMM, the sample excitation field is modulated via interference while the CM focal profile is directly proportional to the illumination field. A similar analysis method to that adopted for CM analysis is applied here. The FMM imaging process can be evaluated by independently considering individual illumination and detection effects and subsequently collating their combinatorial effect. Unity magnification for illumination and detection optics is assumed.

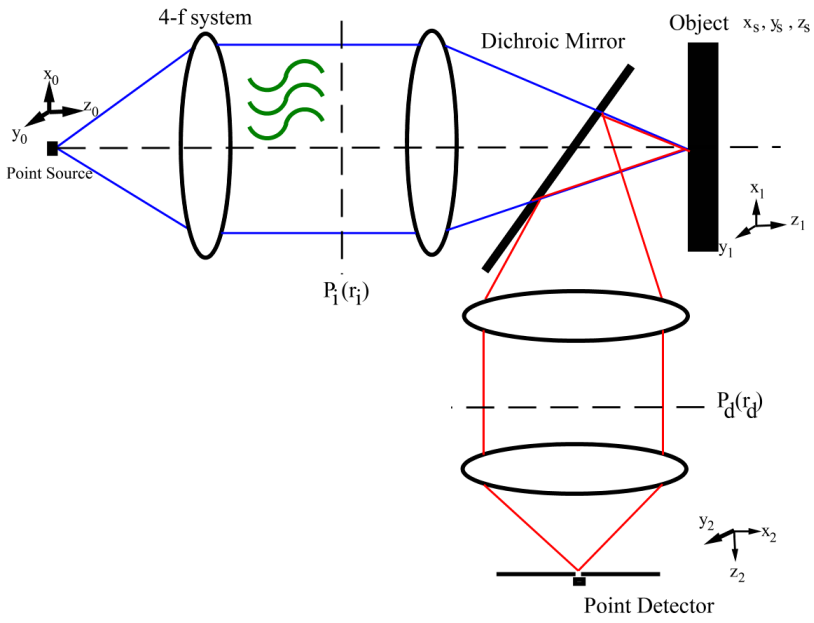

Figure 3.10: FMM schematic diagram(reflection mode).
FMM utilising fluorescence is shown with the blue optical lines indicate the illumination while red lines indicate the returning fluorescence optical path. The green curvy line indicating the modulation in the illumination pupil function.

Fluorescence imaging is an incoherent process and the system is expressed by an intensity point spread function (intensity-linearity). For ease of analysis, the source and detector are modelled by an infinitesimal point. This reduces analysis complexity and the resulting point spread function is solely dependent on the lens point spread function. Unity magnification is assumed for both illumination and detection optics.

Illumination

The illumination IPSF is shaped by the interference between the light contributed from both the unmodulated and modulated aperture region. According to the interference equation, the sample excitation field can be expressed as,

$$E_i(r_1) = h_{i1}(r_1) + h_{i2}(r_1)\exp(j2\pi ft) \tag{3.13}$$

where h_{i1} & h_{i2} are the point spread functions of the modulating and reference aperture regions and $\exp(j2\pi ft)$ is the introduced phase modulation. r_1 denotes the radial coordinates at focal point and is used to describe the spatial distribution of the intensity. The equivalent intensity is given by modulus of the focal field. Unity magnification is assumed.

For an on-axis point illumination source ($r_0 = [0, 0, 0]$),

$$\begin{aligned} I_i(r_1) &= |h_{i1}(r_1)|^2 + |h_{i2}(r_1)|^2 + 2Re\left[h_{i1}(r_1)\, h_{i2}^*(r_1)\, exp(-2j\pi ft)\right] \\ &= |h_{i1}(r_1)|^2 + |h_{i2}(r_1)|^2 \\ &\quad +2\left|h_{i1}(r_1)\, h_{i2}^*(r_1)\right| \cos\left(-2\pi ft + \angle h_{i1}(r_1)\, h_{i2}^*(r_1)\right) \end{aligned} \tag{3.14}$$

The 1st and 2nd term are the DC terms from the interference while the last term is the modulation terms with the modulation frequency f which is directly equivalent to the rate at which the phase is modulated in the modulating region.

Since FMM relies on a modulation frequency detection technique for improved scattering rejection capability, only the modulation component of the illumination intensity is considered for the imaging process computation. We simply drop the frequency term and utilise the in-phase component for calculation:

$$\begin{aligned} I_{illuminationin-phase}(r_1) &= 2\left|h_{i1}(r_1)\, h_{i2}^*(r_1)\right| \cos\left(\angle h_{i1}(r_1)\, h_{i2}^*(r_1)\right) \\ &= 2Re\left[h_{i1}(r_1)\, h_{i2}^*(r_1)\right] \end{aligned} \tag{3.15}$$

The total specimen emitted fluorescence for a point source is dependent upon its object function $f(r_1)$.

$$H_{emission-modulated}(r_1) = \left[K_i Re\left[h_{i1}(r_1)\, h_{i2}^*(r_1)\right]\right] f(r_s - r_1) \tag{3.16}$$

where K_i is given as a constant factor in illumination strength and $r_s(x_s, y_s, z_s)$ describes the scanned position coordinates. $H_{emission-modulated}(r_1)$ is the fluorescence emission generated by a point illumination source.

3.4.1 Detection

The FMM detection segment does not greatly differ from CM. The detection PSF portion can be attained by the convolution of the collection lens PSF with the detector function. The detector function plays an insurmountable role in determining the sectioning and imaging capability of FMM. The detector function is trained onto the excitation main lobe for observation of its temporal variation. Subsequent demodulation allows one to indirectly measure via extracting the ballistic intensity.

In the detection pathway, fluorescence intensity is detected incoherently. The detection PSF, or rather the detected intensity, can be given by the integration of the intensity over the detector $D(r_2)$:

$$\begin{aligned} H_d(r_1) &= \int |h_d(r_1 - r_2)|^2 D(r_2)\, dr_2 \\ &= |h_d(r_1)|^2 \otimes_2 D(r_1) \end{aligned} \tag{3.17}$$

For an infinitesimal pinhole, the collected intensity for point fluorescence source is

$$H_d(r_1) = |h_d(r_1)|^2 \tag{3.18}$$

3.4.2 FMM modulation aperture

The modulation aperture in the FMM microscope is comprised of two regions, one unmodulated portion acting as a reference source while the other is phase modulated. The modulation signal is generated through interference when the light signal from

the two separate pupil region is brought overlapping with a lens at the focal region exclusively.

In theory, several variants of the aperture configuration can be adopted, each offering different distinct point spread function and hence varied modulation zone and spread. An annular modulation pattern offers simple analysis due to its symmetry, demanding reduced computational complexity. Figure 3.11 below depicts the manner on which the FMM pupil can be based, the inner ring functions as the reference while the shaded exterior region depicts the phase modulated sector.

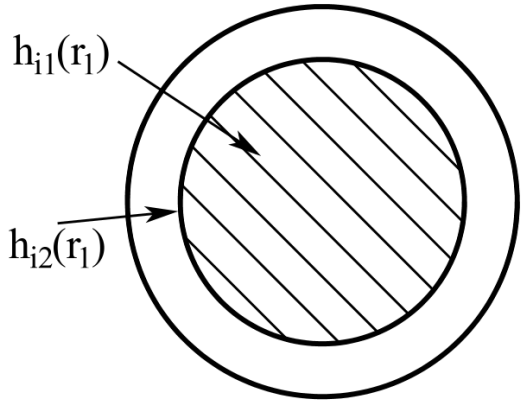

Figure 3.11: Ring shaped aperture.
The aperture is divided in the manner that the shaded and unshaded region are of equal area. Shaded region denotes the modulated region.

The pupil function can be described by the following equation.

$$P(\rho) = \left\{ \begin{array}{cc} 1\,(modulated) & if \quad \rho \leq \alpha \\ 1 & if \quad \alpha \leq \rho \leq 1 \\ 0 & otherwise \end{array} \right\} \tag{3.19}$$

where ρ is the normalised radial coordinates. The above matrix describes a sum of two distinct pupils, defined as $P_{i1} = 1$ for $\rho \leq \alpha$ and $P_{i2} = 1$ for $\alpha \leq \rho \leq 1$. Therefore

the 3D amplitude PSF for the illumination component $h_{i1}(r_1)$ & $h_{i2}(r_1)$, with the vector $\vec{r_1} = \langle \rho, \nu \rangle$, is given by

$$h_{i1}(\vec{r_1}) = \int_0^{\alpha} J_0(\rho\nu)\, exp\left(-\frac{1}{2}\mu\rho^2\right) 2\pi\rho d\rho$$

and

$$\begin{aligned} h_{i2}(\vec{r_1}) &= \int_{\alpha}^{1} J_0(\rho\nu)\, exp\left(-\frac{1}{2}\mu\rho^2\right) 2\pi\rho d\rho \\ &\quad - \int_0^{\alpha} J_0(\rho\nu)\, exp\left(-\frac{1}{2}\mu\rho^2\right) 2\pi\rho d\rho \end{aligned} \tag{3.20}$$

The integration limit variable, α, is established by setting the modulated and unmodulated region area to be equal and hence maximising the interference contrast.

$$\begin{aligned} \text{Area of modulated region} &= \text{Area of unmodulated region} \\ \pi(\alpha)^2 &= \pi(1)^2 - \pi(\alpha)^2 \\ &\Rightarrow \alpha = 0.707 \end{aligned}$$

The value of $\alpha = 0.7$ offers a convenient working approximation to our calculation and is adopted in calculation hereafter. Expressing $h_{i2}(r_1)$ in a more convenient manner (essentially regarding the PSF generated by the annular region as the difference of the PSF produced by two circle of dissimilar radial size),

$$h_{i2}(r_1) = h_{i2a}(r_1) - h_{i2b}(r_1) \tag{3.21}$$

with

$$h_{i2a}(r_1) = \int_0^1 J_0(\rho\nu)\, exp\left(-\tfrac{1}{2}\mu\rho^2\right) 2\pi\rho d\rho$$
$$and$$
$$h_{i2b}(r_1) = \int_0^{0.7} J_0(\rho\nu)\, exp\left(-\tfrac{1}{2}\mu\rho^2\right) 2\pi\rho d\rho$$

3.4.3 FMM IPSF

FMM detected intensity can be expressed as the integration of the fluorescence emission $Re\left[K_i h_{i1}(r_1) h_{i2}^*(r_1)\right] f(r_s - r_1)$ and detection IPSF $|h_d(r_1)|^2$ (assuming infinitesimal detection pinhole) over the r_1 domain.

$$I_i(r_2, r_s) = \int_{-\infty}^{\infty} Re\left[K_i h_{i1}(r_1) h_{i2}^*(r_1)\right] f(r_s - r_1) |h_d(r_2)|^2 dr_1 \tag{3.22}$$

The above relationship resembles a convolution relationship. Depicting the 3D convolution relation over r_2, one can simplify the above equation.

$$\begin{aligned} I(r_s) &= \int_{-\infty}^{\infty} I_i(r_2, r_s)\, dr_2 \\ &= \int_{-\infty}^{\infty} \left[\int_{-\infty}^{\infty} Re\left[K_i h_{i1}(r_1) h_{i2}^*(r_1)\right] |h_d(r_2)|^2 dr_2\right] f(r_s - r_1)\, dr_1 \\ &= h_{eff}(r_s) \otimes_3 f(r_s) \end{aligned} \tag{3.23}$$

where $\otimes_3$ denotes the 3D convolution operation. $h_{eff}(r_s)$ is the 3D effective PSF for the FMM microscope and given by

$$h_{eff}(r) = K_i Re\left[h_{i1}(r) h_{i2}^*(r)\right] |h_d(r)|^2 \tag{3.24}$$

The assumption has been taken that FMM utilises an infinitely small pinhole and the effect of Stoke shift ($\lambda_{ex} < \lambda_{em}$) is ignored for the fluorescence case. A simple

method for the FMM IPSF simulation can be obtained from the difference between the in-phase and out-of-phase IPSF of a CM. Under low modulation frequency assumption, the difference can be regarded as the modulation contrast:

$$h_{FMM-eff}(r) = K_i \left[|h_{in-phase}(r)|^2 - |h_{off-phase}(r)|^2 \right] \times |h_{det}(r)|^2 \tag{3.25}$$

Detailed derivation and simplification is found in the Appendix A. Simulation results for the FMM illumination PSF and the FMM PSF are found in Figure 3.12 and 3.13 respectively.

From the simulation, FMM has a lateral PSF comparable to CM. The FMM PSF is slightly sharper as shown in the region around the radial optical coordinates v = -2. A slight negative dip is detected around the first zeros. A slight contrast reversal might be expected if there is lateral offset of detector or source. For the axial PSF, FMM has a demonstratedly distinct superiority over CM. However, a certain portion of the PSF display extends into negative values, indicating an intensity inversion. Ultimately this is undesirable as false image intensity will lead to error in object recognition.

3.4.4 FMM OTF

The above equation relates a superposition of the light intensity through a sample in an incoherent imaging process. Another analysis test for the FMM properties is via its 3D OTF given by the 3D Fourier Transformation of the intensity point spread function. The OTF portrays and delineates the frequency pass band of the microscope. The transmission efficiency of each intensity component is given. The 3D OTF for FMM can be thus described by

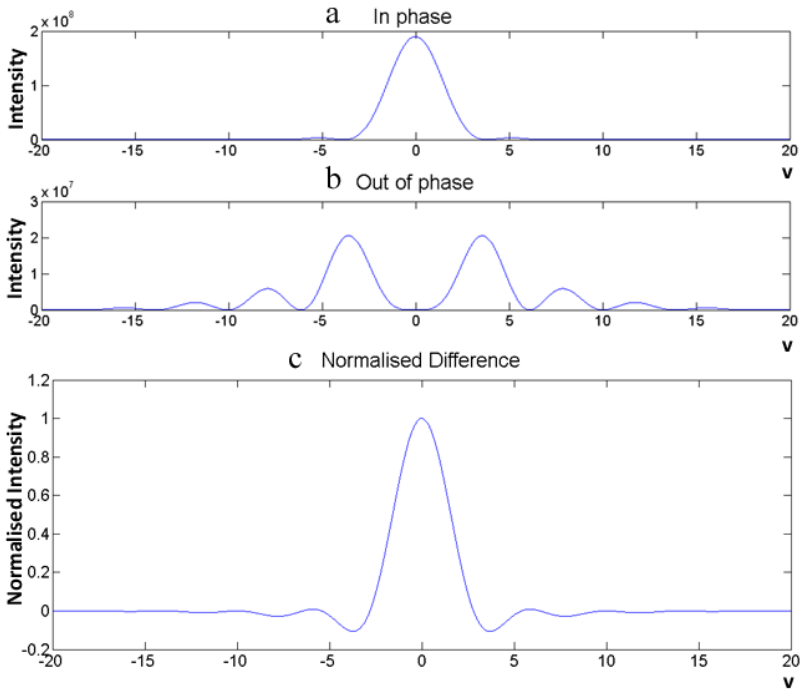

Figure 3.12: FMM illumination PSF.
(a) The in-phase PSF (b) The out-of phase PSF (c) The PSF obtained using the illumination portion of Equation 3.25 with normalisation to the maximum intensity.

$$\begin{aligned} O(l,s) &= F_3\left[h_{eff}(r)\right] \\ &= F_3\left[Re\left[h_{i1}(r)\,h_{i2}^{*}(r)\right]\right] \otimes_3 F_3\left[\left|h_d(r)\right|^2\right] \end{aligned} \tag{3.26}$$

Detector OTF

The OTF of a circular lens [131], representing $F_3\left[\left|h_d(r)\right|^2\right]$ is given by

$$C_d(l,s) = F_3\left[\left|h_d(r)\right|^2\right] = \frac{2}{l} Re\left[\sqrt{1-\left(\frac{|s|}{2}+\frac{l}{2}\right)^2}\right] \tag{3.27}$$

with l & s being the transverse and axial normalised spatial frequency. l is normalised

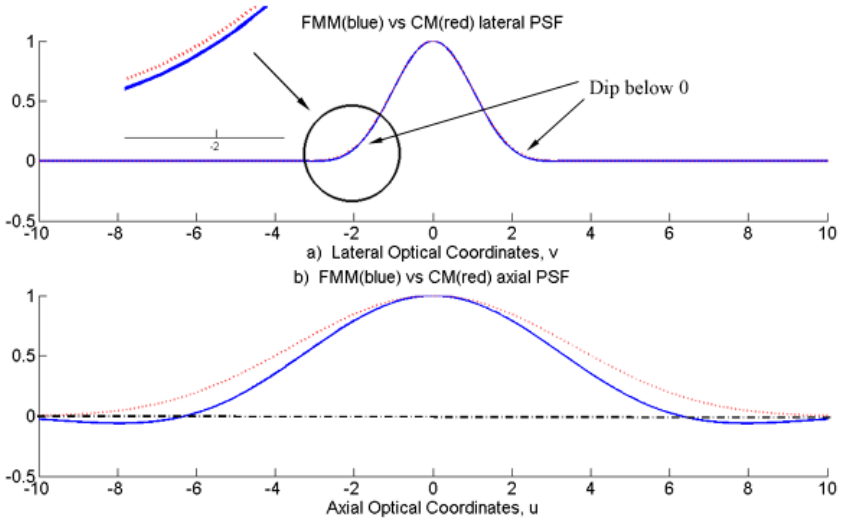

Figure 3.13: FMM vs CM PSF.
(a) Lateral & (b) Axial. FMM is represented in the blue line while CM is represented in the red line. In the lateral PSF, the red line is covered over by the blue line. The insert shown an exploded view of the simulated line at region v=-2, showing a sharper FMM PSF in lateral region. A slight negative dip is detected.

by $\frac{\sin\alpha}{\lambda}$ while s is normalised by $\frac{4\sin^2(\alpha/2)}{\lambda}$.

Illumination OTF

The OTF of a illumination portion, representing $F_3\left[Re\left[h_{i1}\left(r\right)h_{i2}^{*}\left(r\right)\right]\right]$ is given by

$$C_i\left(l,s\right) \quad = \quad F_3\left[Re\left[h_{i1}\left(r\right)h_{i2}^{*}\left(r\right)\right]\right] \tag{3.28}$$

Using the identity $Re\left[Z_1Z_2\right]=\frac{1}{2}\left(Z_1Z_2^{*}+Z_2Z_1^{*}\right)$, and

$$\begin{aligned} C_i\left(l,s\right) &= \frac{1}{2}\times\left(F_3\left[h_{i1}\left(r_1\right)h_{i2a}^{*}\left(r_1\right)\right]+F_3\left[h_{i2a}\left(r_1\right)h_{i1}^{*}\left(r_1\right)\right]\right) \\ &\quad -F_3\left[h_{i1}\left(r_1\right)h_{i2b}^{*}\left(r_1\right)\right] \\ &= C_{i_{positive}}\left(l,s\right)-C_{i_{negative}}\left(l,s\right) \end{aligned} \tag{3.29}$$

The definition of $h^*_{i2a}(r_1)$ and $h^*_{i2b}(r_1)$ was given previously in Eqn.3.21. The Fourier Transform of each individual parts $F_3[h_{i1}(r_1)h^*_{i2a}(r_1)]$, $F_3[h_{i2a}(r_1)h^*_{i1}(r_1)]$ and $F_3[h_{i1}(r_1)h^*_{i2b}(r_1)]$ are equivalent to the 3D reflection CTF of a confocal system with unequal pupil. The general unequal pupil CTF derivation are given in Appendix B.

Illumination OTF - Negative Portion

The negative contribution $C_{i_{negative}}(l,s)$ or $F_3[h_{i1}(r_1)h^*_{i2b}(r_1)]$ is equivalent to the 3D CTF of equal pupils with normalised radius:

$$h_{i1}(r_1) = h_{i1}(r_{i2b}) \tag{3.30}$$

Hence this is the equivalent of a CM CTF with equal pupils:

$$\begin{aligned} C_{i_{negative}}(l,s) &= F_3[h_{i1}(r_1)h^*_{i2b}(r_1)] \\ &= \frac{2}{l}Re\left(\sqrt{(\epsilon)^2 - \left(\frac{s}{l}+\frac{l}{2}\right)^2}\right) \end{aligned} \tag{3.31}$$

where ϵ is the normalised pupil radius, in this case is equal to 0.7. The simulated result is depicted below in Figure 3.14.

Illumination OTF - Positive Portion

The positive contribution to the illumination OTF is $C_{i_{positive}}(l,s)$ or in turn given by $\frac{1}{2} \times (F_3[h_{i1}(r_1)h^*_{i2a}(r_1)] + F_3[h_{i2a}(r_1)h^*_{i1}(r_1)])$, and is shown in Figure 3.15.

Resultant OTF

The optical transfer function (OTF) describes the spatial (angular) variation as a function of spatial (angular) frequency. As pointed out in Eq. 3.26, the resultant

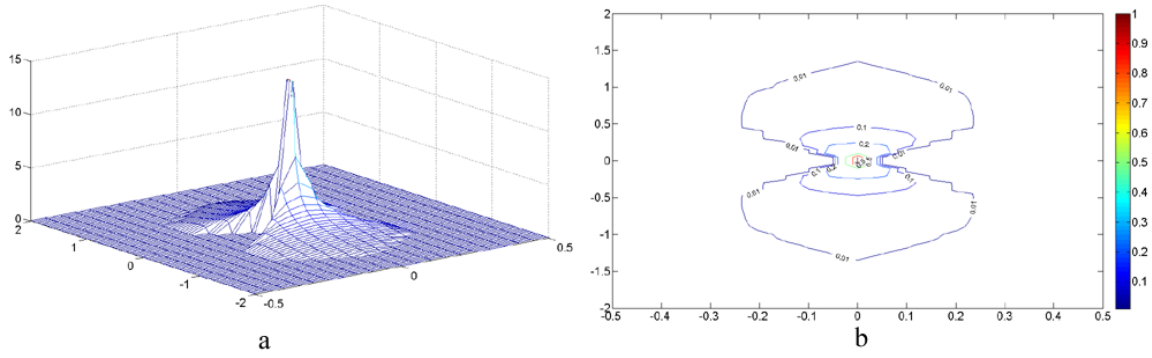

Figure 3.14: Negative portion of illumination OTF
(a) Solid 3D view & (b) Contour View. Result is normalised to the maximum intensity in the simulation result.

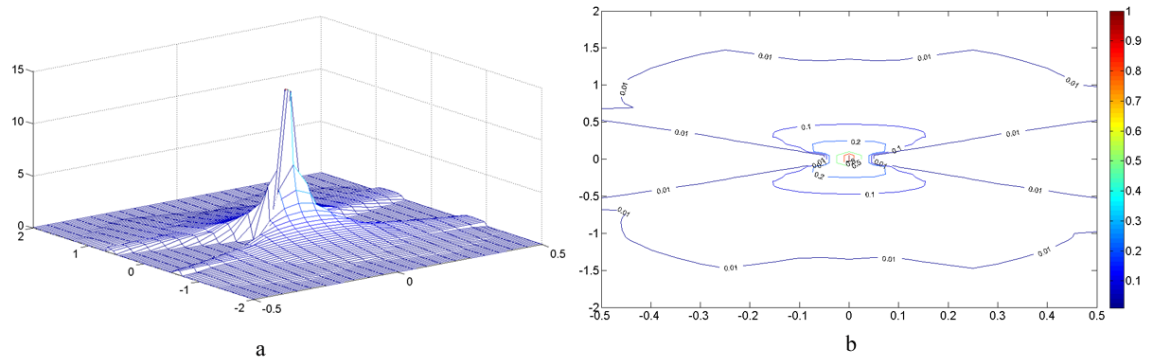

Figure 3.15: Positive portion of illumination OTF
(a) Solid 3D view & (b) Contour View. Result is normalised to the maximum intensity in the simulation result.

OTF is calculated by the 3D Fourier Transform of FMM IPSF [131]. Likewise in a 2D Fourier Transform, the 3D Fourier Transform of the IPSF product could be obtained by the 3D convolution of individual Fourier Transform IPSF components (namely, the illumination and detection IPSF):

$$\begin{aligned} O(l,s) &= F\left\{h_i(\nu,\mu)^2 h_d(\nu,\mu)\right\} \\ &= C_i(l,s) \otimes_3 C_d(l,s) \end{aligned} \tag{3.32}$$

where $C_i(l,s)$ is given by $C_{i_{positive}}(l,s) - C_{i_{negative}}(l,s)$ and l & s denotes the radial and axial normalised spatial frequency. The simulated result is presented below in Figure 3.16. CM OTF simulation is presented in conjunction to provide comparison.

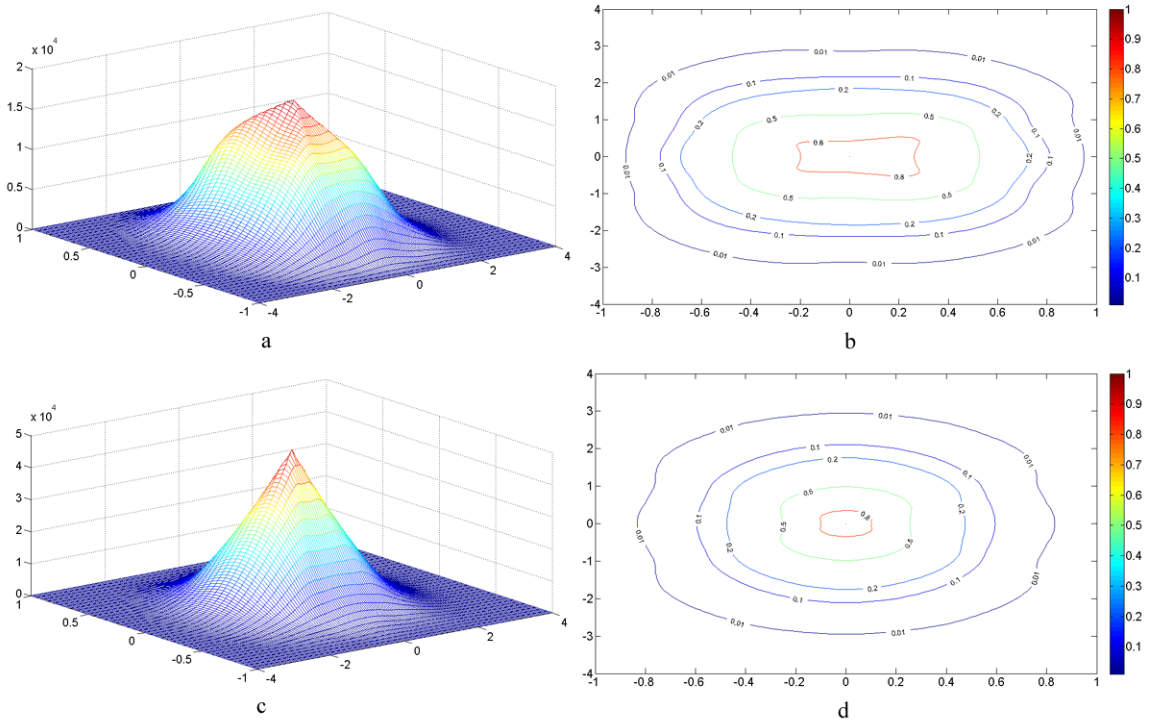

Figure 3.16: FMM OTF with infinesimal pinhole
FMM OTF (a) Solid 3D view (b) Contour view and CM OTF (c) Solid 3D view (d) Contour view. Contour view result is normalised to the maximum intensity in the simulation result.

From the OTF solid view and contour map, a slight difference between CM and FMM in the boundary extent is detected. This is in agreement with the PSF simulation result (Section 3.4.3) obtained earlier. However, this improvement is marginal at best. A more interesting observation lies in that the FMM OTF has higher central weight when compared to CM OTF. The observation bears significance as it provides an explanation on why FMM has better imaging depth. Signal that is transmitted through the imaging system is imaged more strongly in FMM than CM due to the higher OTF magnitude. For the annular based aperture simulated, the boost in the

lateral direction is almost doubled in extent while there is barely any noticeable axial strengthening.

3.4.5 Pinhole influence on FMM

Similarly to CM, enlarging the pinhole, introduce in more signal to the detector. Yet at the same time, a larger pinhole reduces optical sectioning strength and has a deleterious effect on CM lateral and axial resolution. Pinhole enlargement is speculated to have even a greater impact on the method's viability. In FMM, it is imperative that solely the main lobe signal and nothing else is to be collected.

IPSF

For evaluation of finite pinhole effect on the IPSF, it obtained could be evaluated by the following formula [131]. The detector IPSF is convolved with the detector function which is no longer given by a infinitesimal function. It is hence enlarged by the detector function.

$$h_{FMM-eff}(v) = K_i \left[\left| h_{in-phase}(v) \right|^2 - \left| h_{off-phase}(v) \right|^2 \right] \times \left[\left| h_{det}(v) \right|^2 \otimes_2 D(v_d) \right] \tag{3.33}$$

where v & v_d is the normalised radial coordinates of lens and pinhole respectively. $D(v_d)$ is the pinhole function and is taken to be circular. $h_{in-phase}(v)$ & $h_{off-phase}(v)$ is given in the Appendix A. The above equation is then used to simulate for pinhole of various size. The contour plot is shown in the Figure 3.17 while the individual lateral and axial IPSF is shown in Figure 3.18.

The contour plot shows an expanding trend in the IPSF with increasing detector size. This indicates deteriorating resolution as the pinhole size is incremented. For pinhole size v_d= 6 & 8 , the boundary extent is almost equivalent, pointing towards a diminishing return in performance gain when the pinhole is enlarged. Similar trend occurs in the lateral and axial axis simulation. However the difference is not as

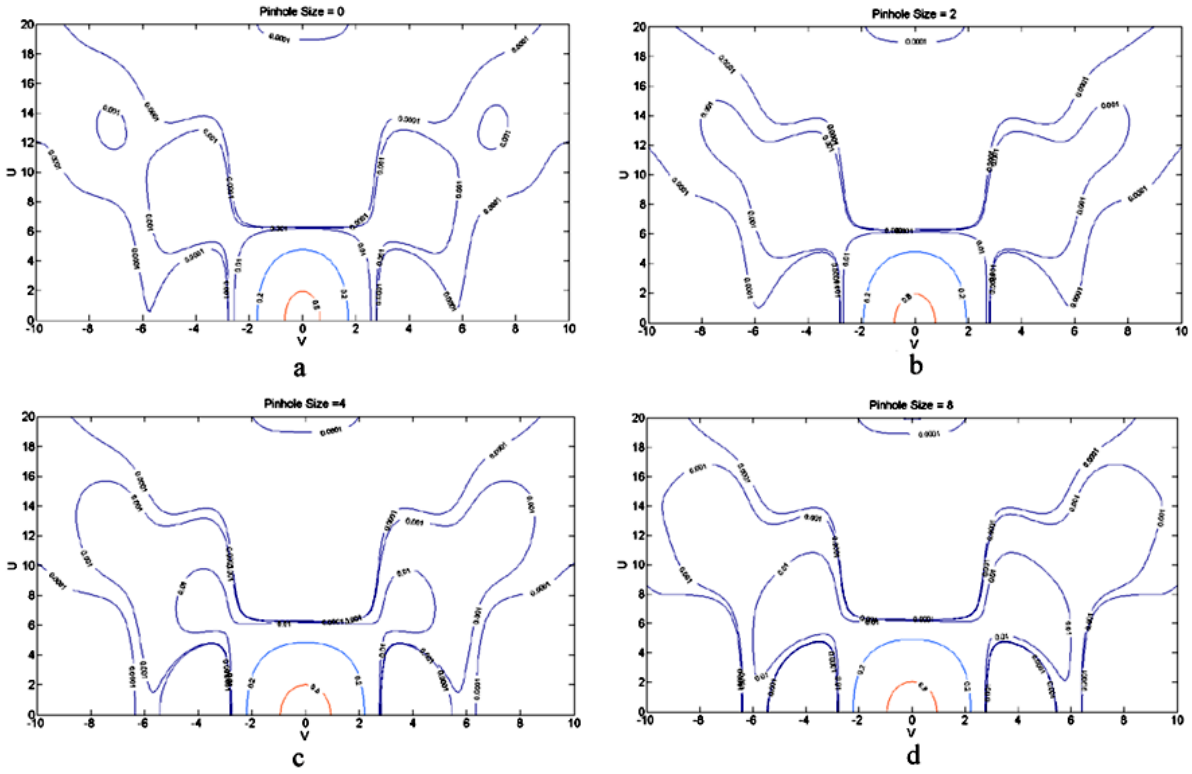

Figure 3.17: Pinhole influence on FMM IPSF (contour map with v and u axis). (a), (b), (c) & (d) represent the pinhole diameter v_d=0,2,4 and 8 respectively

significant as suspected. Only slight resolution loss is found with increasing pinhole size. Ringing effect is further aggravated with the presence of stronger side lobes. At the same time, contrast reversal effect encountered for the case of infinitesimal pinhole is diminished.

OTF

The OTF is likewise obtained from the Fourier Transform of the IPSF. In particular, the collector OTF is modified by

$$C_{d_{new}}(l,s) = C_d(l,s) \times C_{pinhole}(l) \tag{3.34}$$

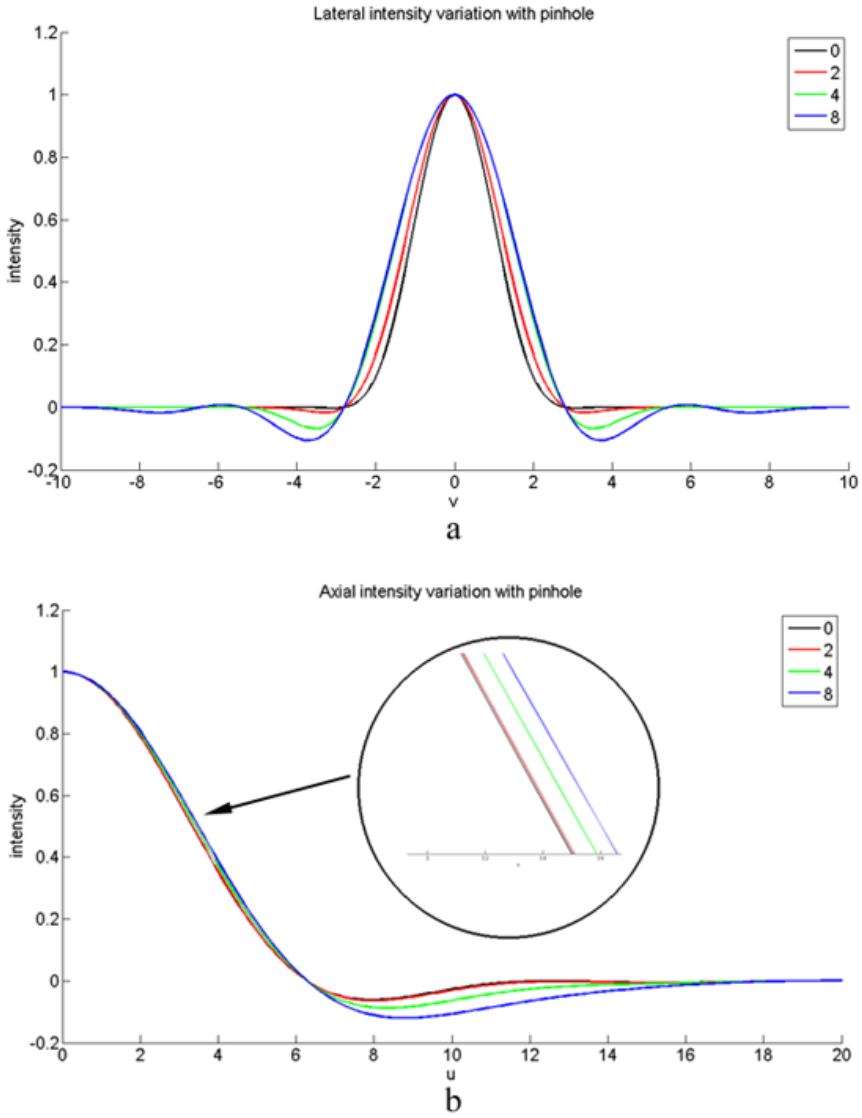

Figure 3.18: Pinhole influence on FMM IPSF
(a) lateral and (b) axial resolution. The exploded view in (b) shows the slight differences in the axial intensity

l & s denotes the radial and axial normalised spatial frequency. Hence the full OTF is calculated by

$$O_{pinhole}(l,s) = C_i(l,s) \otimes C_{d_{new}}(l,s) \tag{3.35}$$

The simulated result is given below in the Figure 3.19 & 3.20

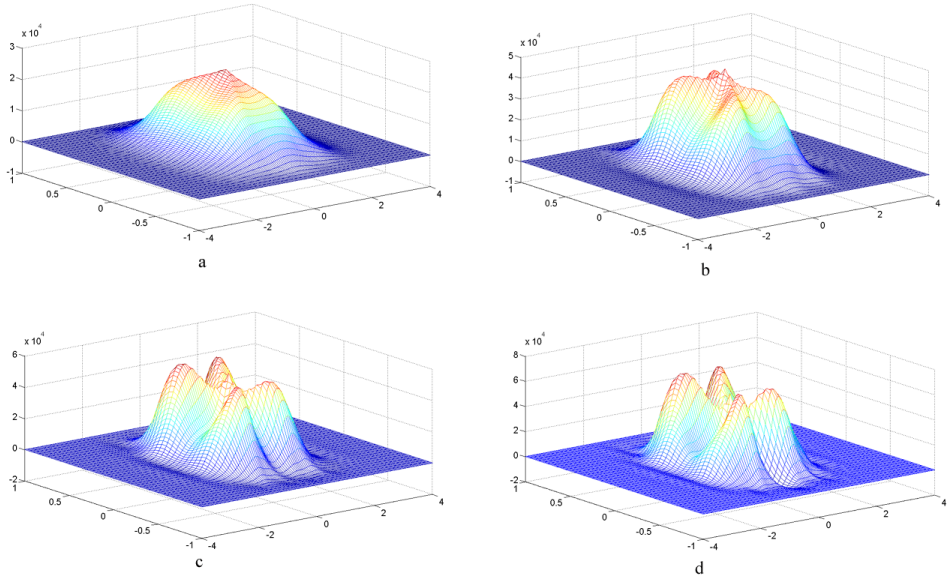

Figure 3.19: FMM OTF under pinhole influence - Solid View
Pinhole size v_d(a) 2, (b) 4, (c) 6 & (d) 8 is shown

From the simulation result obtained, two trends are observed. With increasing pinhole size, the OTF boundary perimeter withdraws towards the center, signifying a decline in spatial resolution. Poorer lateral and axial resolution is expected. Secondly, an OTF magnitude decrease is detected, especially in the central region. With increasing pinhole size, the presence of peaks in the diagonal direction to the axial and lateral direction is found. This suggests that the FMM OTF, as a matter of fact, is formed by the summation of pupils. The role of the FMM pinhole is to suppress the contribution of sidelobes. With increasing pinhole size, FMM tends to CM with multiple pupils. It is likewise noted that for pinhole size $v_d = 2$, the boundary extent decrement is less telling, suggesting that there is a limiting pinhole size in which FMM behaviour holds. A probable theoretical pinhole value that FMM still holds is at the first zero of the illumination PSF or $v_d = 2.717$.

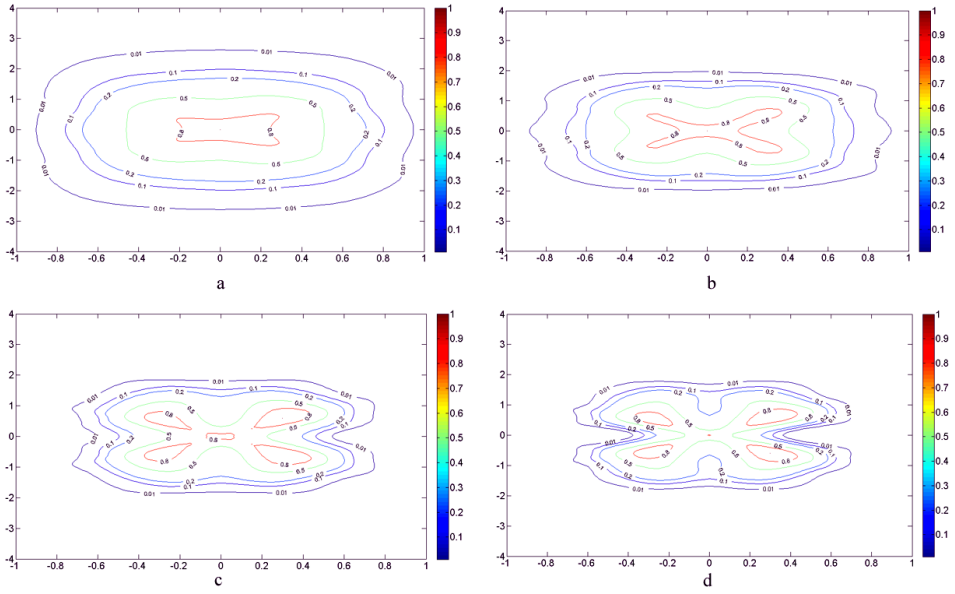

Figure 3.20: FMM OTF under pinhole influence - Contour View
Pinhole size v_d(a) 2, (b) 4, (c) 6 & (d) 8 is shown

Sectioning Strength

FMM sectioning strength with pinhole variation is investigated for this section. The sectioning strength of FMM can be obtained by the imaging of a thin fluorescence object devoid of any features in the transverse direction. The Fourier Spectrum equivalent of a featureless object is given by $C_{FMM}\left(l=0,u\right)$ in which no spatial information is contained in the transverse direction:

$$I_{FMM}\left(u\right)=\int_{-\infty}^{\infty}C_{FMM}\left(l=0,u\right)\exp\left(ius\right)ds \tag{3.36}$$

The simulated result is shown in Figure 3.21.

Apart from the pinhole size, $v_d = 8$, the general axial intensity decreases with increasing axial depth. This is an indication that axial imaging strength decreases with defocus. This is somewhat in keeping with the general trend as expected. For the pinhole size $v_d = 8$, a "disturbing" line plot is noticed. An axial intensity maximum

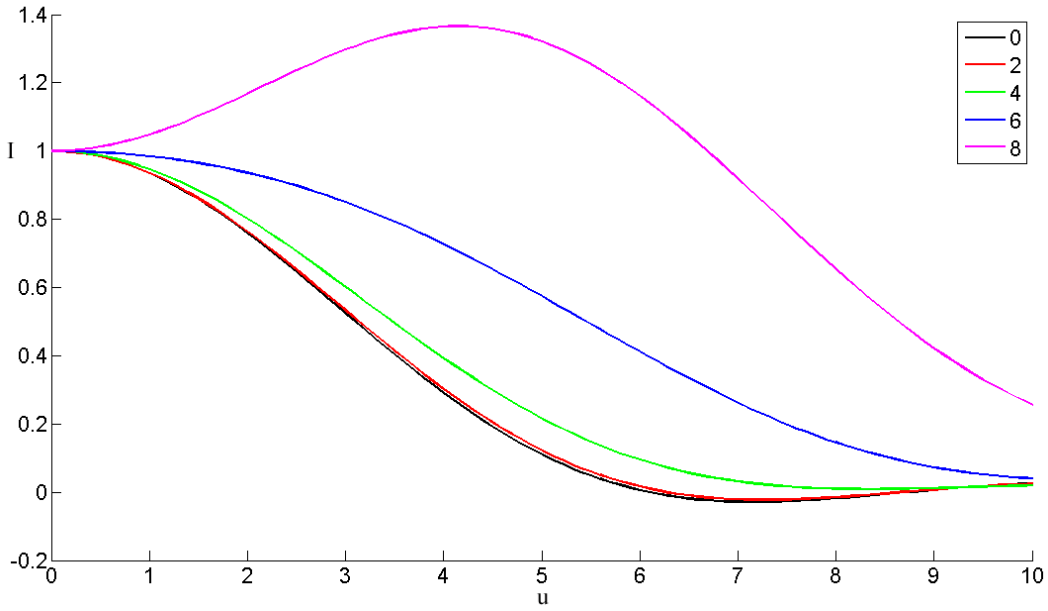

Figure 3.21: Sectioning strength variation with normalised axial depth
Pinhole size v_d 0,2,4,6,8 is being simulated. All readings are normalised against $I_{FMM_{pinholesize}}(0)$ of each pinhole size

is found to be between $u = 4$ and $u = 5$. An axial shift in the focal point appears to have occurred. The discrepancies in the readings could be due to the fact that opening up the pinhole draws in the negative sidelobes into detector.

SBR

A simple background noise measure can be obtained by calculating the total volume intensity of a featureless volume or C_{FMM} $(l = 0, u = 0)$ through integrating the whole CM OTF volume. The SBR is in turn measured by the ratio of the FMM intensity in the focal plane over the background volume. The formula is as given below.

$$SBR = \frac{Signal \quad from \quad the \quad focal}{Volume \quad Background} \tag{3.37}$$

The calculated SBR is displayed in the Table 3.1 below.

Mode	SBR Value
CM	0.0212
FMM	0.0317
FMM(pinhole = 2)	0.0311
FMM(pinhole = 4)	0.0273
FMM(pinhole = 6)	0.018
FMM(pinhole = 8)	0.0099

Table 3.1: Comparison of SBR ratio for CM, FMM and varied pinhole mode.

From the table reading, FMM has much better SBR in comparison to CM. In fact, FMM performs substantially better than CM even with an enlarged pinhole, up to a pinhole size $v_d = 4$. For CM, the optimal pinhole size is often set to be around $v_d = 2.7$ and beyond which, CM resolution and sectioning strength drop drastically. Combined with the coherent gating and heterodyne detection, the maximum allowable pinhole size has increased, allowing for more signal to enter while rejecting the background noise with improved gating techniques.

3.5 Conclusion

This chapter has introduced FMM - a new optical sectioning technique with long imaging depth. An intuitive explanation for the technique is given to provide a working knowledge for the technique. The chapter has also formalised the theory for FMM which provides a new method to achieve optical sectioning in the midst of a highly scattering medium. The simulation result demonstrates that the technique has higher lateral and axial resolution. Improved signal to background ratio is also shown in the simulation for FMM.

Chapter 4

Experimental Setup

4.1 Introduction

This chapter recounts on the ground development of the FMM prototype system. The prototype system serves as the test platform from which further FMM theoretical studies can be conducted. A general system overview will be presented together with a brief description of the system optical pathway. Description of the individual subcomponents or modules will be subsequently outlined for further elaboration and discussion.

4.2 Overview of system

The prototype system is assembled from commercially available components. The FMM system closely resembles a conventional confocal microscope scanning system except for the modification of the illumination aperture. A 640 nm laser, measured 20mW output from CrystaLaser is used as the primary fluorescence excitation source. A scanning system similar to that of the CM system is implemented to provide point by point scanning. Axial scanning and positioning are achieved with a 3D translation stage via computer control. Appropriate source wavelength filtering optics is erected to filter off the stray light sources and the point signal is collected via a highly sensitive detector system. The whole optical setup is mounted on the top of an

optical breadboard for improved stability. The schematic layout of the system is shown in the Figure 4.1 below.

4.2.1 Optical pathway description

The laser output from the CrystalLaser (640nm laser, measured 20mW output) is first expanded through a beam expander and is reflected by a mirror set at 45 degree angle. Part of the light is then modulated through the phase modulator (in a half circle manner). A small portion of the light is transmitted by the dichroic mirror (Omega Optical 660DRLP, cutoff at 660nm) and directed to the phase bias control and detection segment of the setup. Light in the phase bias sampler segment is focused onto a pinhole formed by an optical fiber and a photodetector subsequently convert the light signal into an electrical one to be read out and observed from an oscilloscope. The majority of the excitation light (below cutoff at 660nm) is subsequently reflected by the dichroic mirror towards the sample end. A two dimensional scanning system provided by a galvomirror system (fast scanning mirror FSM CD300 from Newport) formed a beam scanning system through an objective (Olympus LUCPLFLN 20X, a 20X magnification and 0.45 NA objective). Pre lateral and axial specimen positioning is accomplished with the DC motorized 3D translation stage (Thorlabs Inc, MC110 DC motorized stage XYZ/M) via PC control. The emission fluorescence from the each point scan point is descanned through the same scanning system and is transmitted through the revisited dichroic mirror. A filter (Omega Optics, 3RD 670LP) discards stray light noise and permits only the light spectrum in the fluorescence region to enter. A collection lens is utilised to focus the light through the pinhole system formed by a fiber (core size 3-5μm). Conversion of the light signal is done via the highly sensitive PMT (Hamamatsu Photonics, R928) and is amplified with an appropriate electronics system. Subsequent digitisation is performed by NI-DAQ card (NI DAQ USB 6212) and the collected data is processed and reproduced as digitised images.

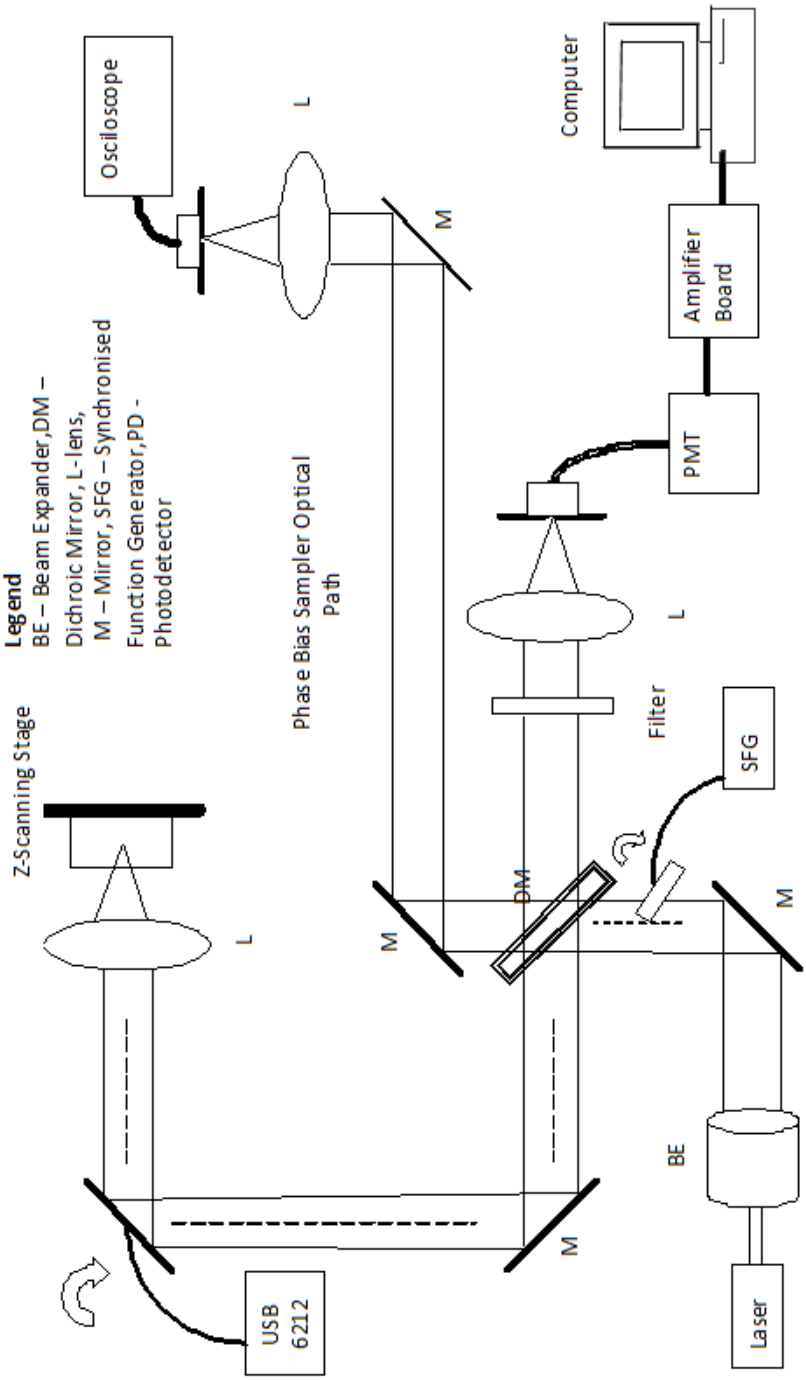

Figure 4.1: Prototype optical system layout.
Setup varies with the mode of the phase modulator being used. A tilted plate phase modulator is being utilised for this diagram. The setup closely resembles a reflection confocal fluorescence microscope.

4.3 Phase Modulator

FMM is a novel technique that utilises coherence gating in the excitation beam to augment the spatial gating provided by a pinhole detector [230]. The main difference between CM and FMM is that a segment of the excitation pupil is periodically phase modulated, with the remaining portion serving as a stationary phase reference. With this technique of altering the illumination phase front, focal spot modulation is established with strong fluorescence intensity modulation arising solely from the focal spot. FMM image quality is partially determined by the effectiveness of the modulation scheme. A stable modulation scheme is crucial to limit the signal fluctuation due to vibration and mechanical drifts.

For practical implementation of the FMM phase modulation scheme, a circular bisected excitation pupil is elected as the choice aperture mode (shown in Figure 4.2). The semicircular pupil applied in this actual realisation should not overtly influence the outcome when compared with the theoretical annular pupil formulation presented in Chapter 3. From scalar diffraction theory, it is conjectured that resolution improvement is asymmetrical in comparison [135, 231] with the uniform improvement furnished by annular aperture. However, such difference is treated as trivial for establishing the confirmation that FMM focal modulation enhances imaging depth. A simulation for the semicircular focal plane intensity result is illustrated in Figure 4.3.

4.3.1 "Double Mirror Reflective Phase Modulator"

Two different forms of phase modulator are developed for the duration of the study [232]. One of them is the "Double Mirror Reflective Phase Modulator", shown in Figure 4.4. The modulator consists of two mirrors, each reflecting half of the excitation beam with a varying phase difference. The two mirrors are positioned close to each other, and their reflecting surfaces are parallel aligned. A sinusoidal driving signal is then supplied to the PZT actuator to generate the phase difference.

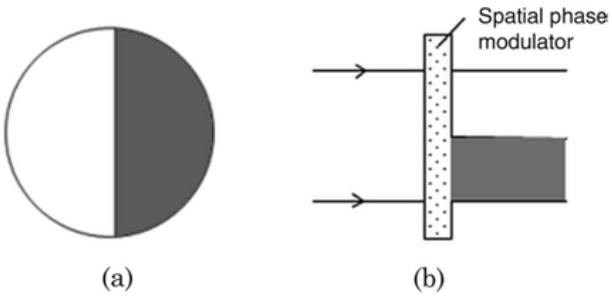

Figure 4.2: Bisected/Semicircular pupil aperture and phase modulator
(a) Bisected back aperture of the pupil. (b) Excitation light path in FMM with a spatial phase modulator. Half of the beam (shaded areas) is subject to periodic phase modulation.

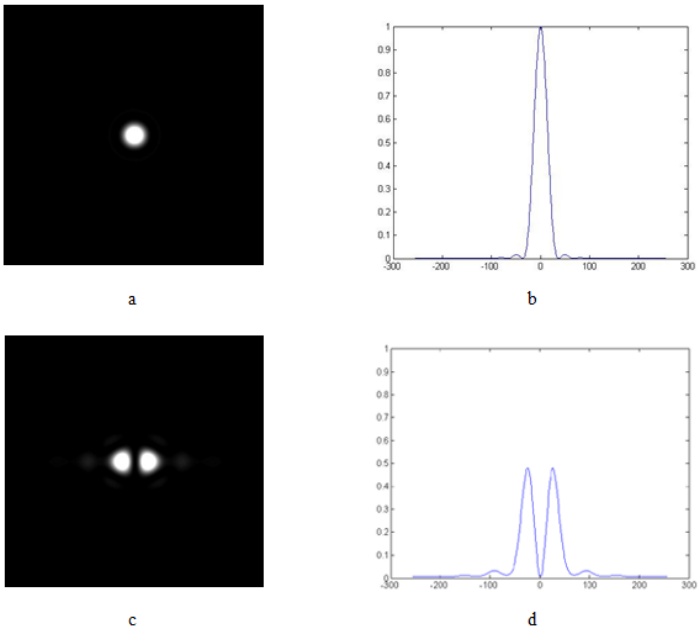

Figure 4.3: MATLAB focal plane intensity simulation result for bisected pupil plane.
Simulation is based on a circular aperture and 2D intensity diagram and their respective cross-sectional intensity profile are shown for $0°(a, b), 180°(c, d)$. The cross-sectional intensity profile are normalised by the maximum intensity from the 2 images to provide a comparison.

Two major problems excluded its usage in the final implementation. Firstly, parallelism between the two beams is difficult to sustain over an extended temporal

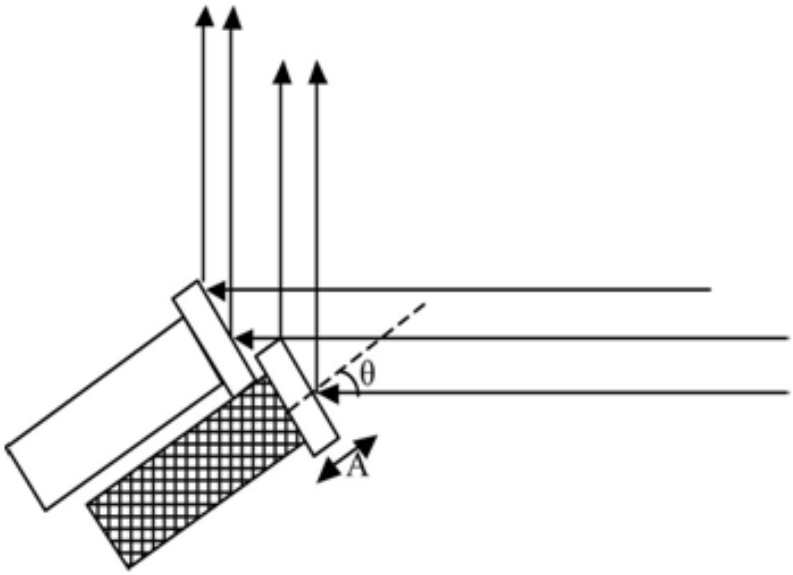

Figure 4.4: Schematic for Double Mirror Reflective Phase Modulation.
The phase difference is given by $\frac{2\pi}{\lambda}(2Acos(2\pi ft)cos(\theta)+L_0)$, where λ is the excitation wavelength θ is the incidence angle, f is the modulation frequency, L_0 is the initial optical path length difference, and A is the amplitude of the PZT displacement proportional to the driving voltage.

duration. Occasional orientation drifting occurs, causing detected oscillatory fluorescence signal to drop significantly. Secondly, the modulated intensity is a mixture of fundamental harmonics and higher harmonics order which drain the power from the zero order. Maximisation of zeroth order harmonics entail precise and consistent configuration of the initial path difference. Once the optimal condition is achieved, most of the ac signal strength is concentrated around the fundamental frequency as shown in the power spectrum (Figure 4.5b). However, the two separate mirror plate architecture is unwieldy for adjustment. The problem is further compounded by mechanical drifting and oscillation which often necessitate regular tweaking to the phase modulator. The optical path length drift is depicted in the simulation result shown below in Figure 4.5 c & d.

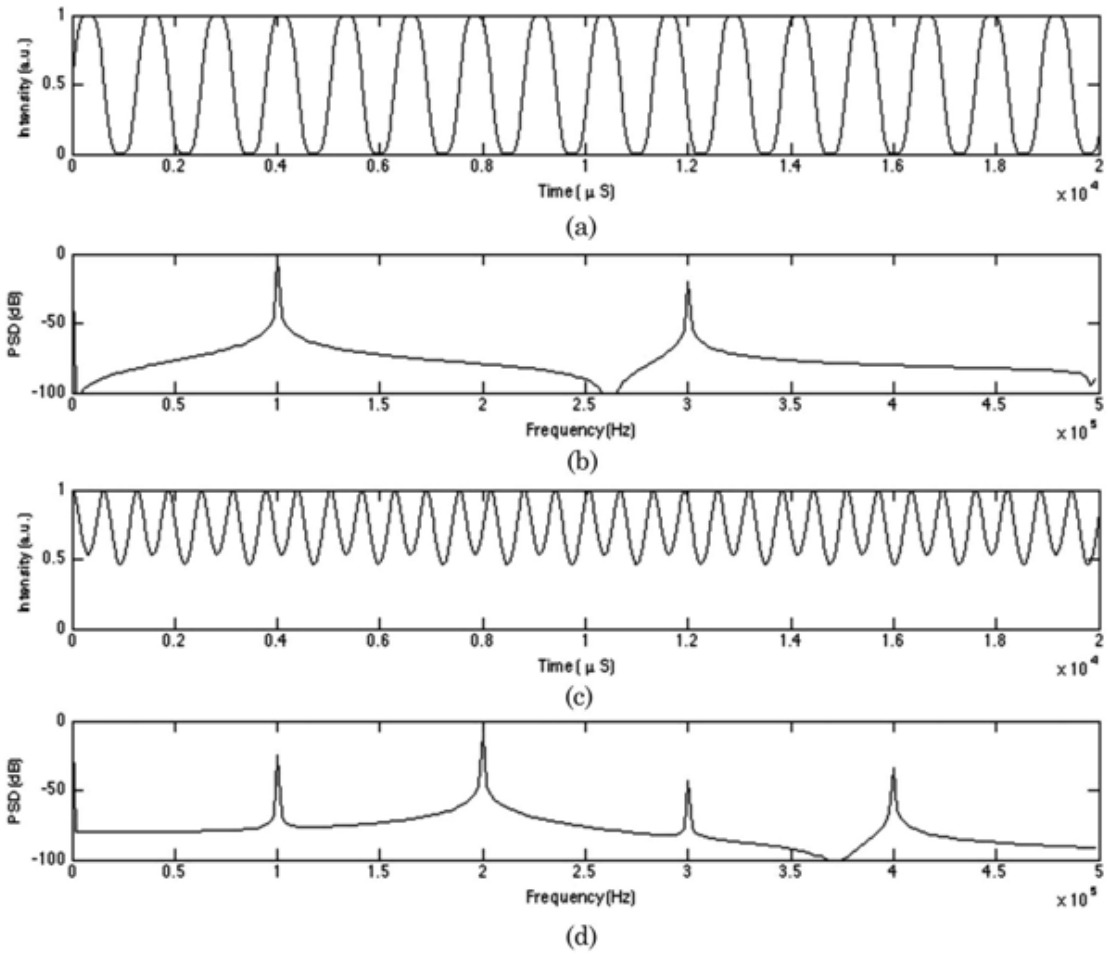

Figure 4.5: Simulation result for Double Mirror Reflective Phase Modulator
(a) Simulated focal excitation waveform and (b) its power spectrum from an ideal two-mirror modulator are compared with the (c)waveform and (d) power spectrum when the optical path length difference drifts away.

4.3.2 "Tilting Plate Phase Modulator"

An improved modulator setup is shown in Figure 4.6. A glass plate mounted on a galvanometer is inserted into the optical path, bisecting the light beam in half. This subjects half of the optical beam to a phase delay determined nonlinearly by the driving signal while the remaining portion remains unperturbed. Given that the glass plate surfaces are parallel and homogenous, the two half beam could be kept parallel to one another- an advantage not found in the previous implementation.

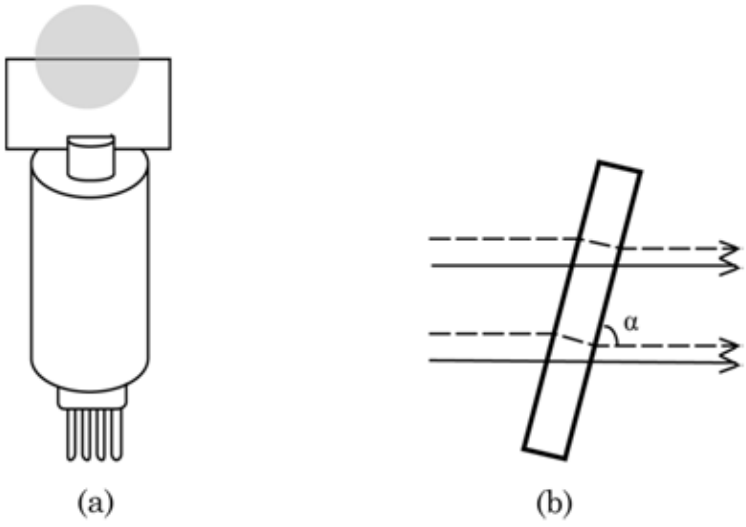

Figure 4.6: Schematic for Tilting Plate Phase Modulator
(a) Glass plate mounted on a galvanometer, intersecting half of the excitation beam whose cross section is indicated by the gray circle. (b) Optical paths of the half-beam propagating through the glass plate (dashed lines) and the half-beam propagating in the air (solid lines).The corresponding phase modulation is given by $\frac{2\pi}{\lambda} D \left(\sqrt{n_2^2 - \sin^2 (triangle\,(\omega t))} - \cos (triangle\,(\omega t)) \right)$ where D is the glass plate thickness, λ is the excitation wavelength, n is the refractive index of glass, and α is the tilting angle as a function of time. *triangle* denotes a triangular wave function. Detailed derivation is given in the Appendix D.

Individual modulator parameter values are determined by operation and mechanical constraints. These values indirectly dictate the modulation strength and frequency. The phase modulation operation is nonlinear and quasi-linear operation

requires the operation tilting angle to be minuscule. The total optical path length change within one period of angular scan is hundreds of multiples of the wavelength. Hence, unlike the old design, the initial phase difference has little impact on the interference signal spectrum. The new modulator is also much more versatile in adjustment in comparison to the old design. Tuning for better modulation strength is achieved simply by adjusting a single glass plate and strong stable modulation strength is much more easily achieved.

4.3.3 Phase bias sampler

Due to the thermal expansion and mechanical instability of the excitation beam path, the phase modulation can become unstable and drift over time. A beam sampler was set up along the excitation pathway to direct a small portion of the modulated beam that is focused via a collecting lens to a fiber pinhole. A New Focus balanced receiver (Model 2107) subsequently converts the light modulation into an electrical signal, which is captured by an oscilloscope visually. One of the sampled output of the "Tilted Plate Phase Modulator" is shown in Figure 4.7.

The phase bias sampler serves as a detection and supervisory control mechanism to detect for the irregularities in the phase modulator. Manual correction is made to the SFG amplitude and phase control after inspecting the waveform output from oscilloscope. The optical path of the phase bias control serves as a secondary alignment path for the focusing and collimation of various optical elements. The source, object plane, and image and phase bias plane pinhole, are kept in focus with one another. Minor adjustment could be effected by observing the signal readout from the photodetector connected to the phase bias plane pinhole without disturbing the main optical pathway.

4.4 Scanning mechanism

The scanning mechanism is accomplished with the aid of a fast scanning mirror FSM CD300 from Newport. Previous implementation of the scanning system consists of a

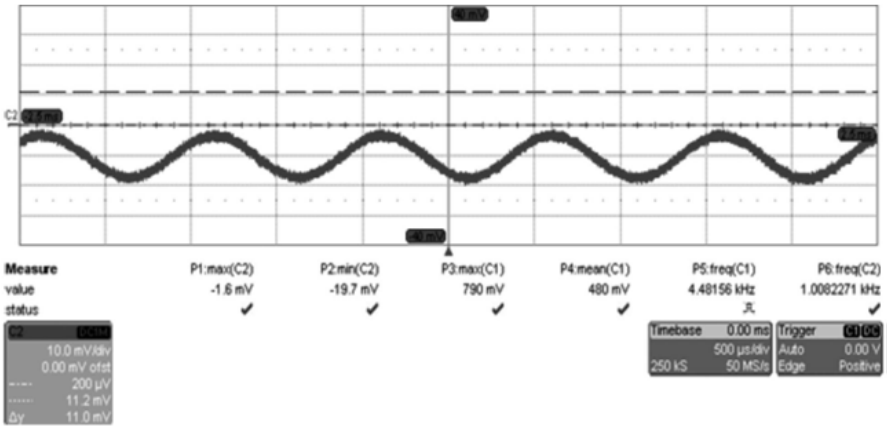

Figure 4.7: Observed output with the phase bias sampler
The operational parameters slightly differ from the simulated parameters in Appendix D. The galvanometer is driven by a 5 Hz triangle wave and the initial tilting angle of the glass plate is about 45°. The modulation frequency was measured around 1 kHz, which can be adjusted by varying the galvanometer driving frequency and/or amplitude.

simple 1D scanning galvomirror (fast axis) working in conjunction with a translation stage (forming the slow axis) to provide a 2D enface scan. In comparison, the fast scanning mirror system provides dual axis x-y scanning at a maximum speed of 10 rad/sec, eliminating the synchronization required between the stage and galvomirror system. The scanning mirror is first aligned by centering the beam to the optical axis of the scanning mirror. Subsequently the scanning mirror is tilted at 45° so that the optical beam goes through a corresponding 90° right angled deflection as shown in Figure 4.8 below. This reduces any ambiguities in the uniformity of the beam phase.

NI USB 6212 is utilized to furnish the command voltage for the FSM mirror control unit which governs the mirror motion (shown in Figure 4.9). FSM rotation step size is determined by the USB 6212 step voltage applied and can be calculated with the following formula: $\frac{Maximum\ rotation\ angle}{Max\ voltage\ supplied} \times step\ size$. For the x-axis scanning, a continuous triangle signal wave is supplied, while in the y-axis scanning, the step size voltage is incremented in a discrete manner. Signal voltage variation is reproduced in Figure 4.10 a & b below. The complete scanning motion is carried out in a raster

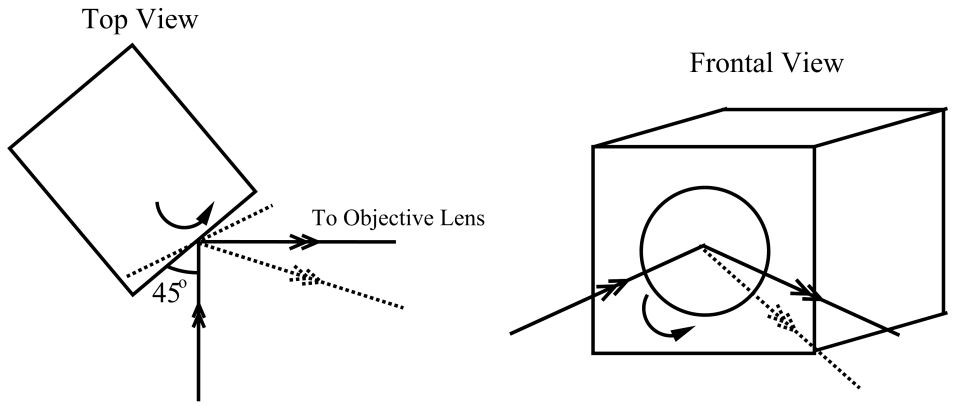

Figure 4.8: Alignment of the FSM300.
FSM is aligned to be at 45° tilted towards the incoming optical beam so that the reflected beam goes through a right-angled deflection.

manner in Figure 4.10 c.

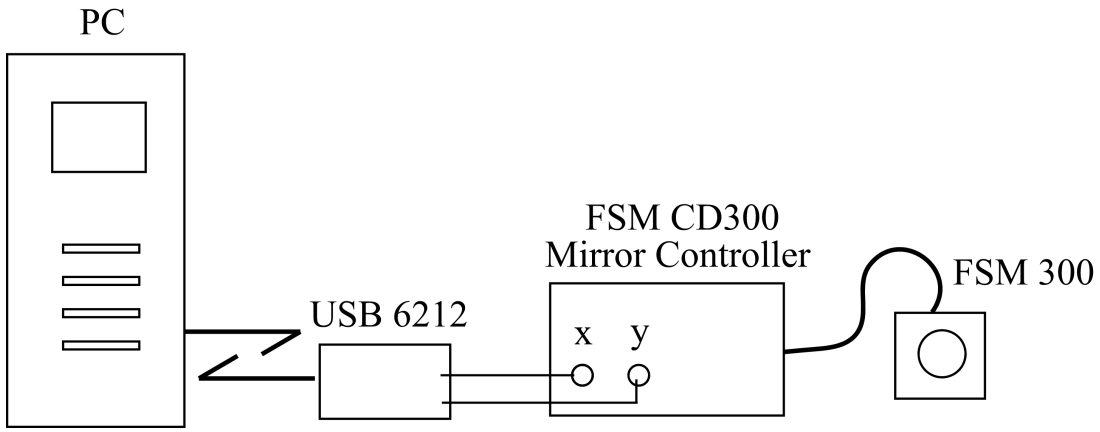

Figure 4.9: Electrical connection and control of FSM 300.
Rotation command in terms of voltage is supplied by USB 6212 to drive the controller unit and indirectly the FSM300.

A simple geometrical optical model approximates the lateral step size generated by the scanning mirror deflection angle shift. The lateral step size δy is calculated by $\delta y \times tan(\delta\varphi)$, with f being the focal length and $\delta\varphi$ the scanning mirror deflection

angle shift. The approximation holds by taking the assumption that the focal length is long with minute operation deflection angle shift.

4.5 Z-Stage control and lateral positioning

Specimen axial and lateral positioning is managed via on MC110 DC motorized stage with a PCI controller board (DCX-PCI100, PMC) installed within a PC. The manufacturer-provided software "Motion Controller" is applied for independent positioning control for the stage. The recommended manufacturer settings parameters are set for each individual working channel as shown in Figure 4.12. Previous scanning system implementation utilises the translation stage acting as one of the scanning axes (generally set as the slow scan axis). The DC motorized stage operation poses backlash problems that have to be corrected with post image processing operation. Therefore, the stage scanning system was replaced with the glavomirror beam scanning system.

4.6 Detection optics and electronics

The chief objective of FMM is to acquire deep imaging capability amidst strong photons scattering within the turbid medium. Hence the detection optics/electronics presents the last avenue to augment the signal quality either by eliminating the stray signal or by boosting the converted electrical signal obtained. The sequence and schematic flow of the detection optics/electronics is shown in Figure 4.13.

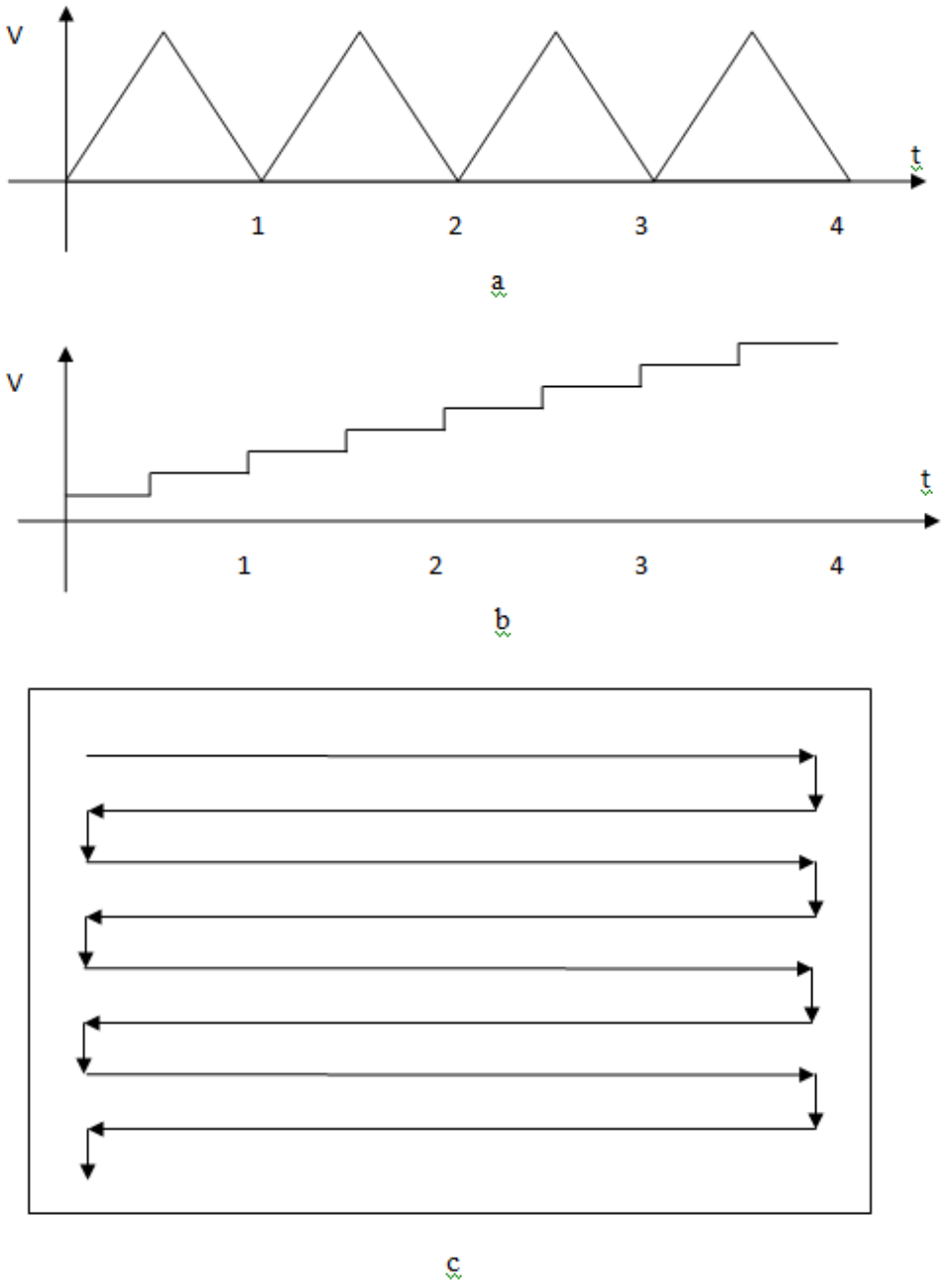

Figure 4.10: Voltage output from NI-USB 6212 for X,Y axis control.
(a) X-axis scanning axis command voltage (b) Y-axis scanning axis command voltage (c) Raster scan pattern achieved by the command voltage supplied to the controller unit.

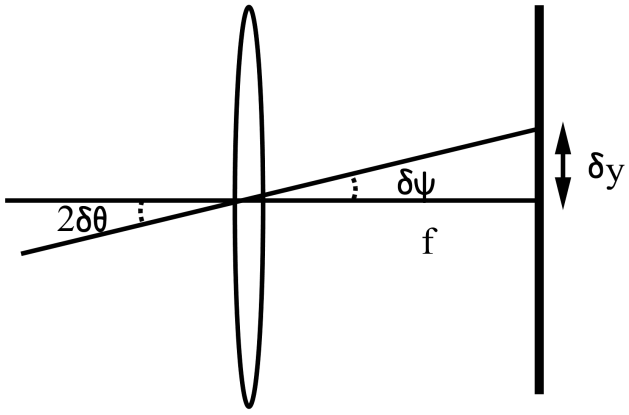

Figure 4.11: Simplified model for calculating lateral scan step.
The scan step is given by$y = f \times tan(\delta\varphi)$ where f is the focal length, $\delta\varphi$ is the beam tilt angle, $\delta\phi$ is the FSM tilted angle and $\delta\varphi \approx 2\delta\phi$.

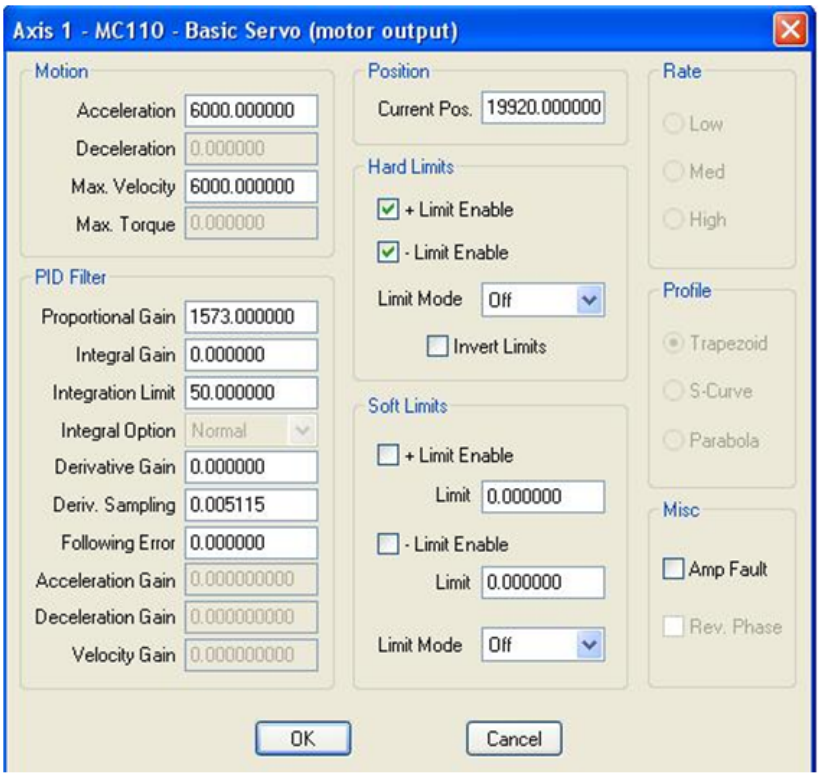

Figure 4.12: Manufacturer recommended settings for translation stage
Similar values are set to all three axis(X,Y,Z).

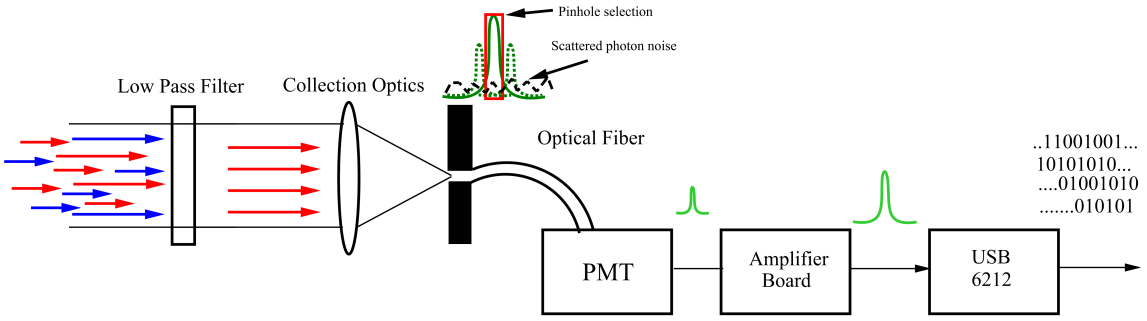

Figure 4.13: Schematic flow of the detection optics/electronics.
Optical beam is filtered by the low pass filter to extract the fluorescence light. Collection optics collects the modulated/unmodulated fluorescence and is spatially filtered by the pinhole formed by the fiber. Optical beam is converted into electrical signal by the PMT and is amplified by the amplifier board. Digitisation is performed by the NI-USB 6212.

4.6.1 Detection optics/filters

The excess excitation signal and autofluorescence appear as system background noises. Filters and a dichroic mirror are utilized to discriminate the wanted signal from these noises. The following filters set is applied for the corresponding dyes in Table 4.1. The filtered light signal is subsequently collected by the collection optics which focused it onto the pinhole.

Label	Excitation(nm)	Emission(nm)	Filter Used	Dichroic Mirror Used
Alexa Fluosphere	645	680	3RD 670LP	Beam Splitter
'DiR'; DiIC18(7)	750	780	3RD 670LP	DRLP660
'DiD'; DiIC18(5)	644	665	3RD 670LP	DRLP660

Table 4.1: Dyes with their respective excitation and emission wavelength and the corresponding filter and dichroic mirror used for the study.

4.6.2 Optical fiber

The core of the single mode fiber serves in a manner similar to that of a conventional pinhole. Hence the pinhole can be replaced with an optical fiber. In order to ensure that most of the fluorescent light is captured, an equivalent core diameter size of about 1 optical unit is adopted instead of the confocal criterion of 0.5 optical units [134] under uniform magnification settings. The optical fiber diameter is expressed in optical units by the following equation:

$$v_p = 2\pi r_p sin\left(\alpha\right) \backslash \lambda \tag{4.1}$$

where v_p & r_p is the optical fiber core radius in optical units and real dimension respectively. $sin\left(\alpha\right)$ refers to the numerical aperture and λ is the returning fluorescence wavelength.

For the experimental setup, a single mode optical fiber ($\approx$ 0.1 NA) of 4.5μm core or an equivalent in optical units of 20.10 was used. However, the objective used has a 20x magnification and this effectively constrains the detection spot size to be $\approx$1.0.

4.6.3 PMT detection unit

The focused beam which consists of both modulated and unmodulated fluorescence signal is collected via an optical fiber which functions as the pinhole. This is sequentially linked to a side-on type PMT, R928 from Hamamatsu Photonics which is housed in a custom built detector housing unit as shown in Figure 4.14. The corresponding PMT voltage adjustment could be performed through the electrical adjustment control in Figure 4.15.

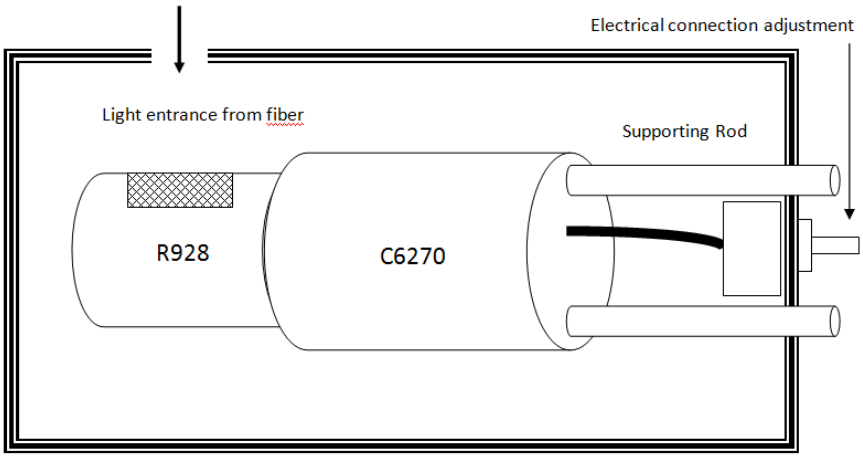

Figure 4.14: PMT box housing diagram
The PMT position from the light entrance window is calculated using geometrical optics and the fiber NA to ensure maximum coverage of the PMT detector window.

4.6.4 Analog Amplification

The electrical signal is amplified by an amplifier board, a multi-functional 2 channel board from twlux (TW30 series, gain bandwidth product of 1MHz). The phase modulating signal is fixed at 1Khz while the amplifier board gain is tuned to be ≈ 200. The amplified signal is read in through the DAQ card analog input port. Digitisation of the signal is achieved by the NI USB PCI-6212 DAQ card. A custom program was written in Labview 7.1 for transferring the digitized signal to computer memory for subsequent Fourier Transformation and modulated signal extraction. From the collected digitized signal, relevant processing is applied and the relevant signal is extracted from the spectrum at the modulated frequency point.

4.7 Software

Individual module control is achieved with the aid of the in-house developed software. NI Labview is the elected software platform adopted for software development because

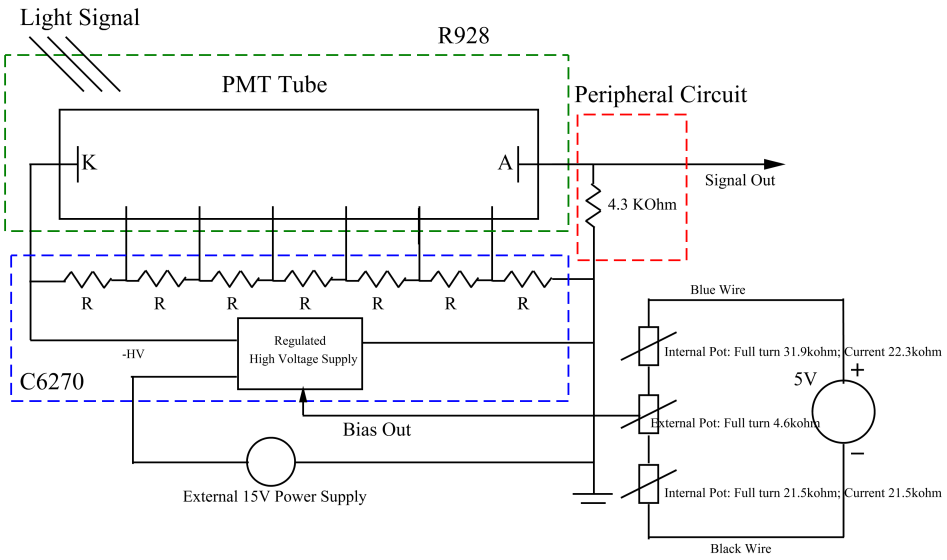

Figure 4.15: PMT global circuit diagram.
R refers to the internal resistor in the C6270 while K and A refers to the cathode and anode. - HV is the high voltage supply to the cathode. The Peripheral Circuit acts as a form of loading and current to voltage conversion circuit while the bias circuit control the -HV ouput of the C6270. Hence the PMT is constrained to operate at a particular voltage range and thus avoiding potential damage caused by large cathode voltage or input signal. Circuit is not drawn to real size.

of its numerous readily available algorithm and function for rapid data acquisition, signal analysis and hardware support. The graphical programming environment and numerous high-level programming tools allow for lower development time and less debugging problem compared to using text based programming languages.

The function of the in-house software can be divided into three portions:

i Data acquisition

ii Scanning mirror control

iii Data processing

The data acquisition function and scanning mirror control are performed synchronously to improve the acquisition speed while data processing is executed after the acquisitions are concluded.

4.7.1 Data acquisition

The main task of data acquisition is to initialize the analog acquisition, start the acquisition and finally the removal of the acquisition task, as shown in Figure 4.16. In the initialization process, a communication channel is opened between the measurement device (NI-USB 6212) and the PC. The number of channels to read and its associated parameters are set to the measurement device and the buffer (the amount dependent on timing settings) is allocated during this stage. Data from a single channel (amount controlled by user) are read into the memory in the start stage while in the end acquisition stage the buffer is cleaned up, releasing the device and memory space for next operation.

The data acquisition rate has to be at least to be double the modulation frequency to satisfy the Nyquist Sampling Criterion. Hence for the actual experiment, the data acquisition rate (10Khz) is tuned to be at 10x the modulation frequency ($\approx 1Khz$).

4.7.2 Scanning mirror control

Two analog output channels are created in the program to adjust the FSM tilt angle by varying the command voltage in the manner outlined in the earlier section, Section 4.4. The X-controller channel is initiated to write a continuous triangle wave while the Y-controller channel is written to only when one line scan is completed, or equivalently when the number of point scans in one line is fulfilled. In order to speed up the application, data acquisition and scanning mirror control is executed in parallel. A separate timing clock is allocated internally with synchronized trigger signal provided via the analog input channel to allow for simultaneous commencement of the data acquisition and mirror scanning. A typical parameter value set for the scanning mirror control is given in Table 4.2 below.

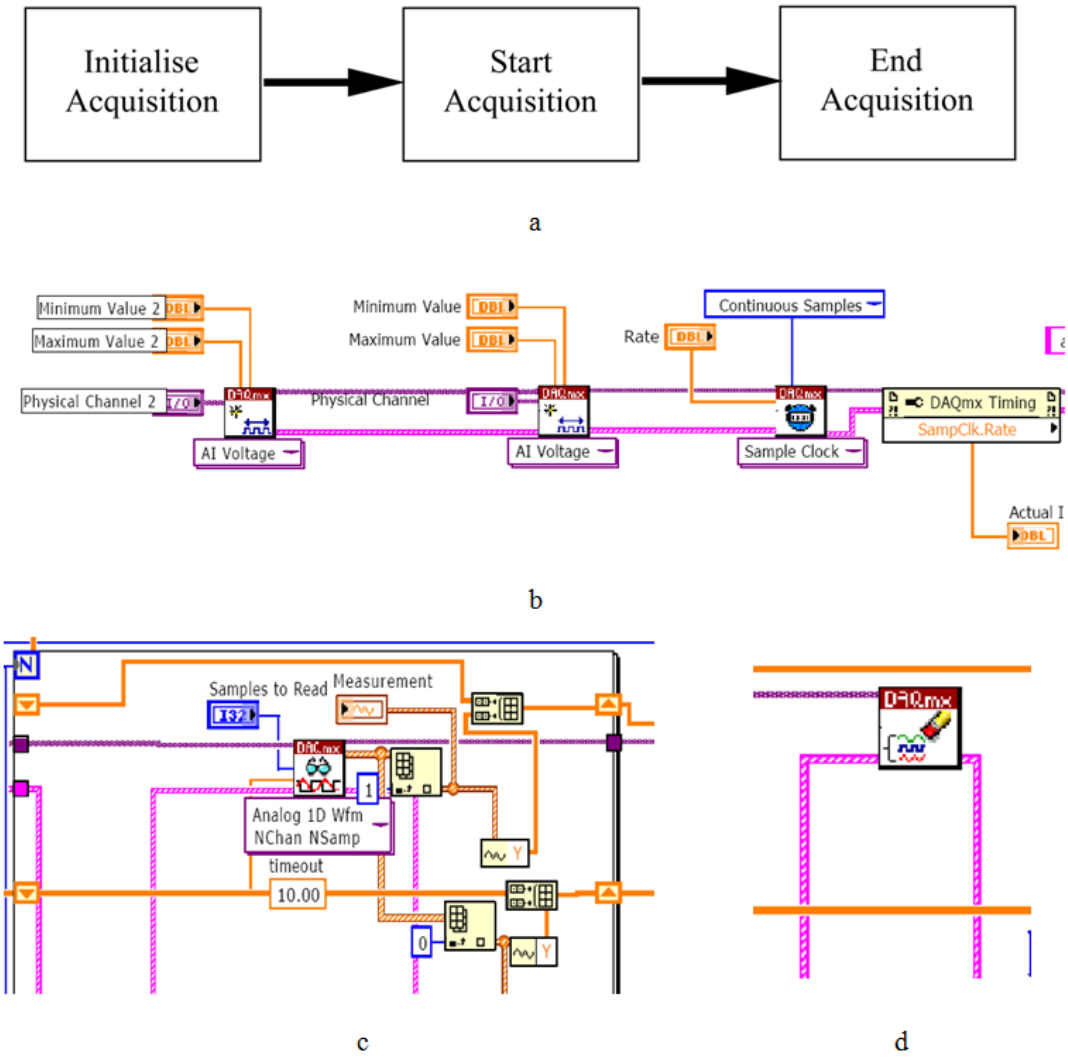

Figure 4.16: Flowchart and Labview snippet code for data acquisition.
a) The sequential programming flow of data acquisition in the program. Labview code for b) "Initialise Acquisition c) "Start Acquisition d) "Stop Acquisition.

4.8 Data process

The acquired data is subsequently processed by the program. For this program portion, MATLAB script is elected over Labview image processing VI for ease in testing. MATLAB scripts are embedded into the main Labview program through the usage

Channel	Frequency	Mode	Samples written
Analog Read	10000 samples/sec	Continuous	5000
Analog Write(X)	10000 samples/sec	Continous	5000
Analog Write(Y)	2Hz	Discrete	1

Table 4.2: Analog read in and write out parameter used.
Analog Write(Y) frequency is calculated by the time taken for 5000 samples to be completely read in.

of a script window. Data organisation and imaging processing operation are then accordingly handled by the script. The steps are summarized in the Figure 4.17.

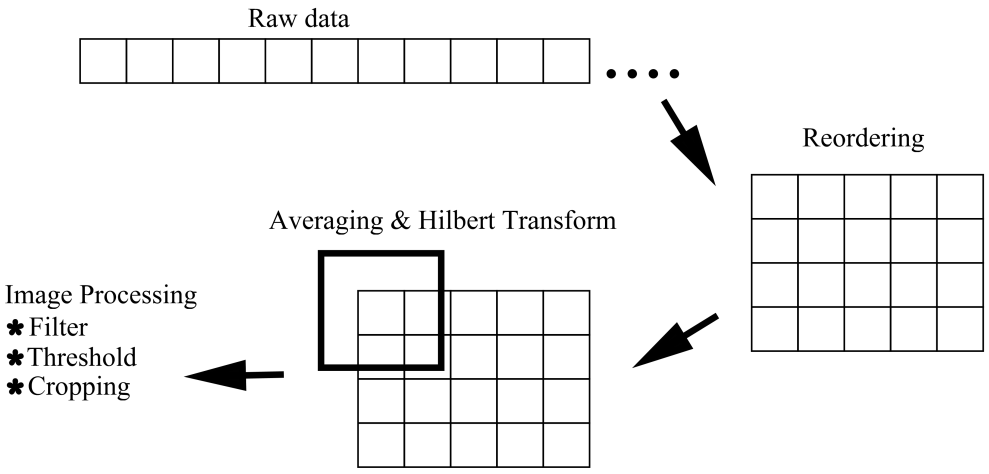

Figure 4.17: Steps in the image processing portion of the program.
Raw data is sorted, reordered and row-reversed to compensate for the raster scan. Averaging and Hilbert Transform are applied to obtain the DC and modulation results respectively. Final image processing done to improve on image obtained.

The acquired data is sequentially read in through the DAQ card. The acquired data stream is required to be sorted out and rearranged into a 2D matrix to represent the 2D image. The data stream is segmented to the number of vertical scan rows with each row containing the same number of data bits. Due to even-odd row reversal scanning pattern, the even row has to be reordered from right to left through the "fliplr" command.

After the proper ordering of the data stream, filtering is done to extract out the DC and heterodyne component. For every image pixel, x data bits are obtained for every image pixel. Obtaining the DC value is a trivial task. The mean is taken among these x data bits set to retrieve the DC component image. For modulated component extraction, a time domain sinusoidal filter of 1kHz of length 20 data bit is created. The filter is convoluted with each row of data. In each row, data is truncated to return the signal to its original time domain and Fast Fourier Transform is performed onto the truncated data. Subsequently, the individual row data are multiplied with the Hilbert row mask before taking the inverse fft. The Hilbert row mask pixel values are defined as:

- 1 for $i = 1$, $n/2$ +1
- 2 for $i = 2$, 3.... $n/2$
- 0 for $i = n/2$+ 2,.....n

where n is the length of the row data and i is the element index in the data row.

The modulated component is extracted by taking the average of the processed data in each row. The above operation is conducted for every single row. In order to compare the results, the result obtained from the modulated component has to be normalised against the data length of the filter.

Chapter 5

Experiments & Results

5.1 Introduction

Experimental results obtained with the prototype setup are discussed in this chapter. Varied samples were used and their preparation procedures are discussed in the next section. Images were then acquired with the prototype setup and discussion on the images obtained is mentioned in the following section. An integrated hybrid FMM-OCT setup will be presented together with the result captured. The last section summarises the outcome as well as dispensing an in-depth discussion from all the studies done.

5.2 Empirical PSF

Before embarking on FMM sample imaging, the FMM PSF is determined empirically. An empirical PSF is useful in validation of the system actual performance. Methods for collecting a PSF are described in [233]. In general, an empirical PSF is obtained by imaging a fluorescence bead that is smaller than the Rayleigh resolution limit, according to the formula: $resolution = \frac{0.61 * wavelength}{numerical\ aperture}$. Generally, a fluorescence bead of less than 3 times the resolution size is selected for gathering the empirical PSF.

For FMM PSF characterization, fluorescence spheres from Invitrogen, TransFluoSpheres carboxylate-modified microspheres, $0.1\mu m$, with an excitation wavelength of $0.488\mu m$ and an emission wavelength of $0.560\mu m$ were used. For the experiment, we have utilised Olympus 60x 1.2 NA UPlanApo water immersion objective lens. The calculated Rayleigh resolution limit is given by $0.28\mu m$, approximately 3 times the fluorescence bead size.

The microscope is adjusted so that the optics are properly aligned. A drop of the diluted liquid containing fluorescence beads is then dropped onto a glass slide and the samples are brought into focus by adjusting the axial distance. A stack of images is taken to chart the image transition from the top of the beads to below. From the images, a sphere close to the image center is chosen. The lateral intensity profile is plotted for all images in the stack and the intensity from the focal plane is chosen by picking the image which displays the highest intensity profile from the cumulated image stack. The axial intensity is selected from the point with the peak intensity at the focal plane. The intensity for the same point is tracked throughout the image stack. The lateral (x,y) and axial intensity profile is plotted in Figure 5.1 & 5.2 below.

From the experimental results, CM PSF is symmetrical for both the x & y direction. The FWHM of CM is approximately $0.32\mu m$ which differs from the theoretical CM resolution $\approx 0.21\mu m$. The differences could be due to aberration as well as the under-filling of the lens aperture. The FMM lateral PSF relates a more complicated relationship. Due to the usage of a non symmetrical modulation aperture (semi-circular), PSF FWHM is not uniform or symmetric. FMM FWHM in the x-direction and y-direction is $\approx 0.3\mu m$ & $0.2\mu m$ respectively. The result show a much greater PSF improvement over the theoretical calculation. The FMM PSF in the x-direction is somewhat skewed at one side. The skewing phenomenon may be the result of imbalanced modulation. One portion of the semi circle aperture could be slightly larger in radial extent over its counterpart. This contributes to the non symmetrical PSF. The above conjecture could likewise help to explain the slight shift in PSF observed in the FMM reading.

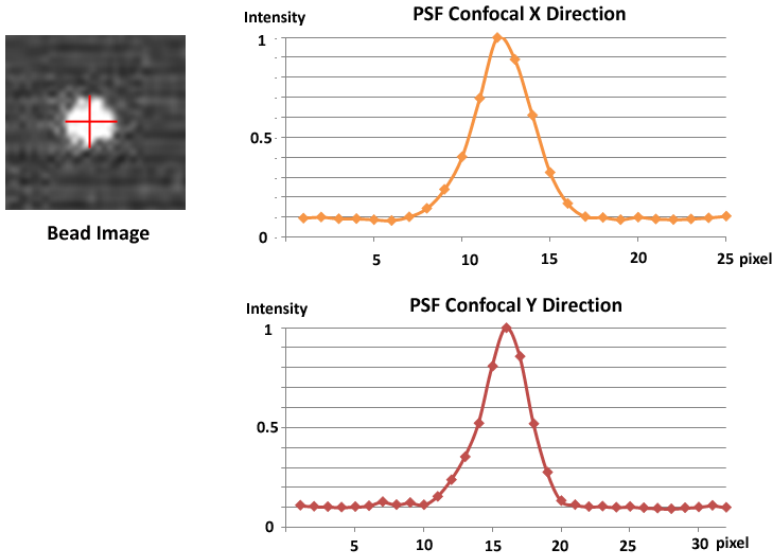

Figure 5.1: CM intensity profile for fluorescence bead.
Top left: Bead image. Right: The lateral intensity profile for fluorescence bead. Each pixel correspond to $0.084\mu m$.

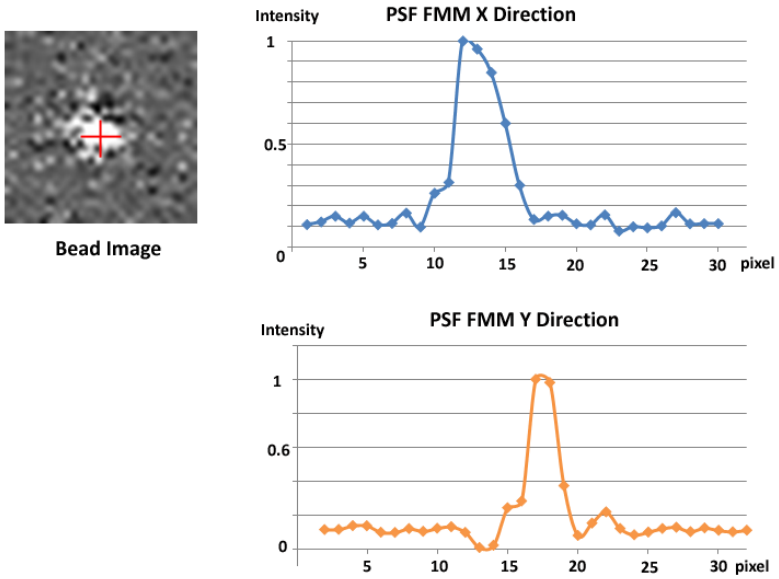

Figure 5.2: FMM intensity profile for fluorescence bead.
Top left: Bead image. Right: The lateral intensity profile for fluorescence bead. Each pixel correspond to $0.084\mu m$.

The axial result is shown in Figure 5.3 below. The plot is obtained from the same bead as above but 4 central pixels are selected and averaged to obtain the axial profile across all layers. The CM and FMM intensity plot obtained are normalized by the individual maximum. From the experimental result, FMM exhibits a sharper FWHM compared to CM ($\approx 4.6\mu m$ to $\approx 6.3\mu m$). This points to the stronger sectioning strength demonstrated in the theorectical computation. Interestingly, the FMM exhibits a number of pronounced asymmetric side peaks. On the contrary, these peaks are insignificant in CM. A plausible explanation for these peaks is due to the reflection from the glass slide surface. In FMM, the sharper FWHM made these peaks much more distinguishable.

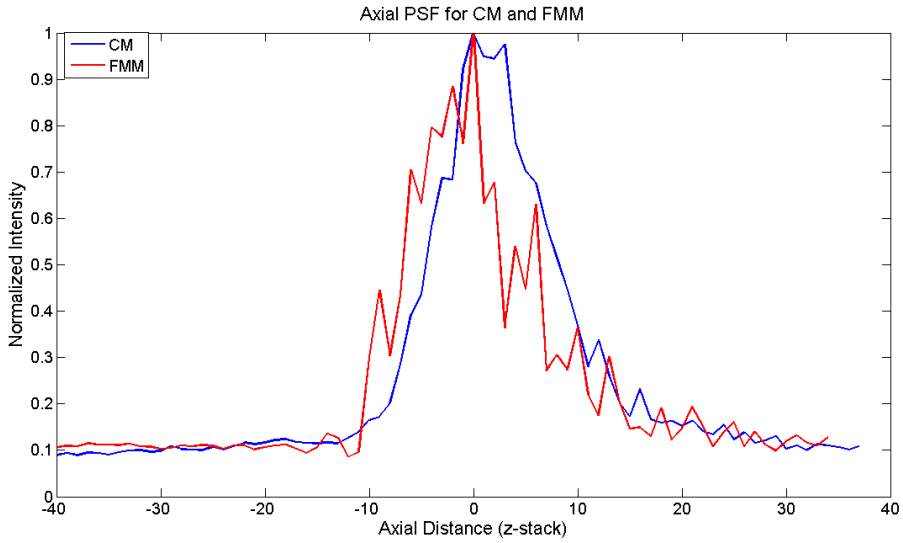

Figure 5.3: FMM and CM axial intensity profile for fluorescence bead.
Red: FMM. Blue: CM. Intensity reading presented in layer stack number, from the 40th layer above to the 40th layer below region from the point of maximal intensity(or focal plane). Each layer corresponds to a thickness of 0.5 μm.

5.3 Preparation of samples

Three different sample sets were examined in the experiment. Each specimen warrants a different processing preparation and test condition. The test study was conducted in an incremental manner such that the previous test serves as a guidance for the implementation of the successive test.

5.3.1 Schefflera Aribocola

The leaf specimen, Schefflera Aribocola (Figure 5.4), was selected as the test specimen. Chlorophyll within the leaves provides a readily available source of autofluoresence and is easily accessible. A 660nm light source can be utilised to excite the chlorophyll B within the leaf. Under lighting conditions, the chlorophyll in the leaf migrate to the mesophyll cell edge to maximise light collection efficiency. The emitted fluorescence from the chlorophyll forms a distinguishable ring-like structure that could be easily identified.

Figure 5.4: Schefflera Aribocola Plant.
Fresh leaves are plucked from the plant itself and then wet mounted onto a glass slide and covered with a cover glass.

5.3.2 Embedded fluorspheres in scattering medium

Alexa fluosphere 645/680nm is chosen as the test probe to be embedded underneath a layer of scattering medium. Formal control testing is conducted to ascertain the approximate imaging depth that could be achieved with the setup. In this experiment, the scattering medium scattering coefficient and depth were varied.

A glass based test target (Figure 5.5) is fabricated for the test. A few drops of fluospheres ($\approx 1 - 2uL$) were dropped onto the coverslip. The coverslip was left to dry in order to remove away the excess liquid medium. A layer of emulsion paint was used as the scattering medium and was painted onto the coverslip and sandwiched with a clean coverslip. In order to reach the necessary scattering medium thickness, the coverslips were slided along and offset to one another, exposing a offset layer of emulsion paint. This is washed off and the coverslip is slided along one another to achieve an even thickness layer. The sandwiched coverslip was then observed under an OCT microscope to determine the actual thickness of the scattering layer. Upon reaching the desired thickness, the "sandwiched emulsion paint" coverslip is then attached to the coverslip with the Fluosphere to form the test target.

5.3.3 Chicken Cartilage

The capability of focal modulation microscopy on an actual animal specimen is evaluated in this investigated. The lipophilic fluorescence DiR/DiD is used to bind to the phospholipids [234]. Phospholipids are a class of lipids and are a major component of all biological membranes. In particular, this investigation targets the chondrocyte present in the chicken cartilage. The labelled chondrocytes present a luminous ring image when excited with the appropriate light source.

Freshly slaughtered chicken was obtained from the market and chicken cartilage is then extracted from it. The cartilage is cut into thin slices between 1-2mm. The chicken cartilage was then washed with PBS and fixated in 4% paraformaldehyde solution. After a two days fixation period, the cartilage was rewashed again in PBS to clean off the paraformaldehye. It was then immersed in the dye liphophilic cyanine

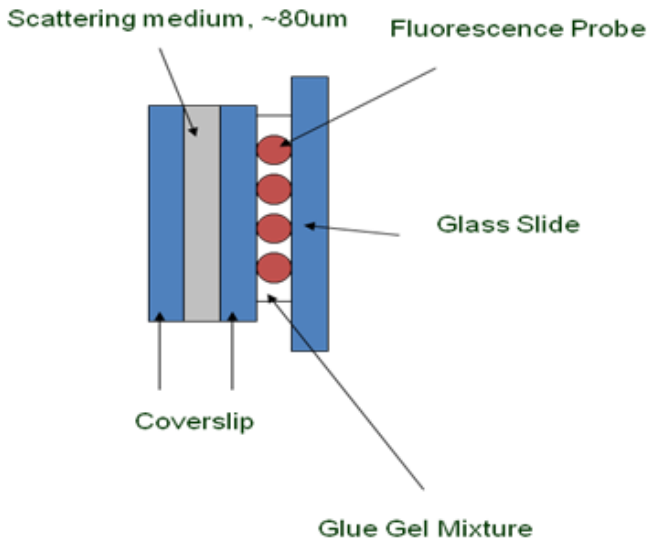

Figure 5.5: Probe Target.
Some amount of glue is added to the glassplate on which the fluorescence probe rests on to "immobilise" the probe

DiR/DiD for a duration of two days. Excess dye was subsequently washed off from the specimen with PBS and placed into the glass well formed by small glass pieces. Antifading PVA mounting medium from Fluka acts as the mounting medium to mount the enclosed specimen. The specimen was finally sealed underneath a grade 1.5 glass coverslip with nail varnish.

5.4 Imaging result

The prepared samples are then examined with the prototype setup. Images and results obtained are discussed in the following sections below.

5.4.1 Leaf autofluorescence

The autofluorescence experiment is a preliminary study undertaken to ascertain the system performance. Chlorophyll autofluorescence is observed at an imaging depth of

160um. From this depth, chloroplast autofluorescence (Figure 5.6b) could be observed clearly in the FMM image while the image obtained from the CM(Figure 5.6a) is badly marred by the multiply scattered light."Ghost" fluorescence image can be detected in the CM image (indicated via the red arrow in Figure 5.6b) while no such fluorescence signal is detected by the FMM. This provides indication that FMM has stronger sectioning capability over CM as the "ghost" image appears to be autofluorescence from cells in an out of focus region.

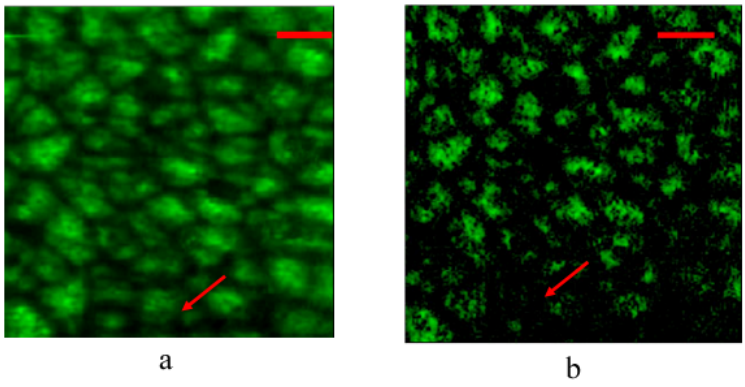

Figure 5.6: Autofluorescence from the Schefflera Aribocola
(a) Autofluorescence from DC reading by CM. (b) Autofluorescence from AC reading by FMM. Scale bar set at 50um.

5.4.2 Test probe fluorescence

Preliminary study via direct microspheres imaging with a 20X objective (LUCPLFLN 20X, Olympus Inc) showed trivial differences between the CM and FMM images in terms of lateral and axial resolutions (result not shown here). The embedded fluorescence bead under the 100μm thick (about 2 scattering length) scattering layer is moved into focus with the motorized translation stage (T25XYZ/M, Thorlabs Inc). As a form of backlash reduction measure, a minimal incremental mechanical stage axial motion of 50nm is utilised for each focusing step. CM microspheres images are acquired in Figure 5.7a with the excitation beam focused on to the smaller microspheres upper surface. The corresponding FMM image is captured and depicted in

Fig 5.7b, which unveils significant surfaces details and paints a strikingly different picture compared to CM image. The microsphere in the central FMM image appears hollow with only its boundary forming a ring-like luminescence. One plausible deduction is that the particular microsphere is much larger than the norm and its top surface is not in focus. The corresponding CM image shows the identical microsphere, solid in appearance and with similar intensity level compared to other microspheres in the same image.That CM has a longer axial depth of field over FMM can be inferred from this study.

In order to examine the optical sectioning capability, the test probe is scanned axially with a 4 micron incremental translation step. In Fig 5.7c the signal level, normalized to the peak value when the microspheres were in the focal plane, is plotted as a function of the defocus. The FMM reading indicates a FWHM of around 7 microns, which is comparable with the objective depth of field ($\approx$ 6.5 microns). The CM peak signal position is slightly displaced to the right, with the FWHM deteriorated to a coarse value of 23 microns.

The image transition from a shallower region to a deeper region is presented in the Figure 5.8. The observation pointed to a stronger axial sectioning capability in FMM over CM. In images ($c \rightarrow e$), the dark central portion of the large bead suggests that the top part of the bead is not imaged as the focus moves deeper into the sample. In contrast, the presence of the top part of the bead is present in the CM counterpart images.

5.4.3 Chondrocytes Imaging

The prototype FMM system scanned the specimen at various depths ranging from 220 to 400 microns. CM image acquired at a depth around 220 microns is shown in Figure 5.9a. Individual cell boundaries are blurred and shared a similar morphology. In contrast, the corresponding FMM image (Fig. 5.9b) shows an assortment of cell shapes with varying intensity. This gives evidence that FMM produces an image of

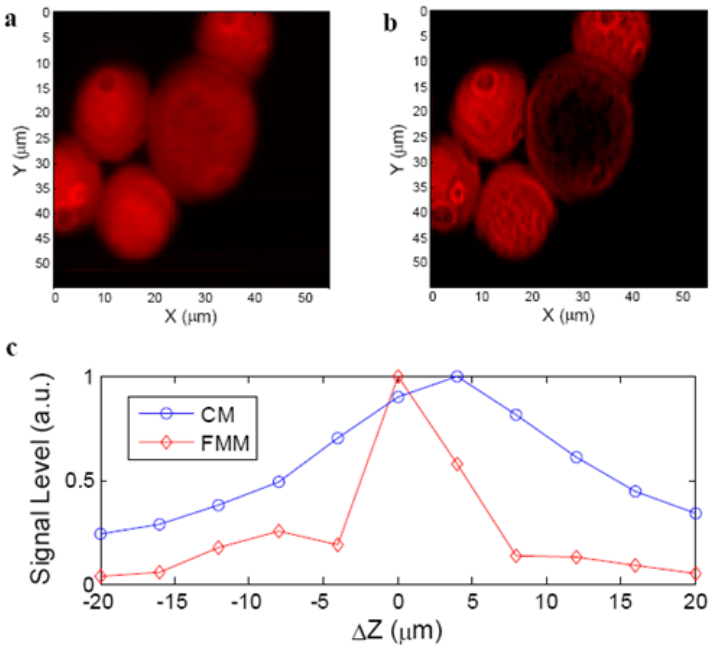

Figure 5.7: Test probe fluorescence
(a) Fluorescence obtained from CM readings (b) Fluorescence image from the FMM method. (c) CM(blue) and FMM(red) signal reading as a function of defocus. The much narrower axial profile of FMM indicates an optical sectioning capability not compromised by scattering. All readings are recorded from a fluorescence layer embedded under a 100um scattering layer

a higher resolution and improved contrast. At the depth of 280 microns, the background signal contributes to an even stronger influence in the CM image (Fig. 5.9c). Cells that are not in focus cast shadows that cannot be differentiated from the in-focused cells. In contrast, background influence is inconspicuous (Figure. 5.9d) and largely missing in the FMM image. This lends credence to the conclusion that FMM shows uncompromised optical sectioning capability and spatial resolution even under scattering when compared to CM.

The prototype FMM attains a maximal imaging depth of around 400 microns. Beyond this limit, SNR deteriorates to the noise floor level because of increased scattered signal reaching the detector as well as depletion of signal strength due to forward and backward absorption. The FMM and CM images obtained from the

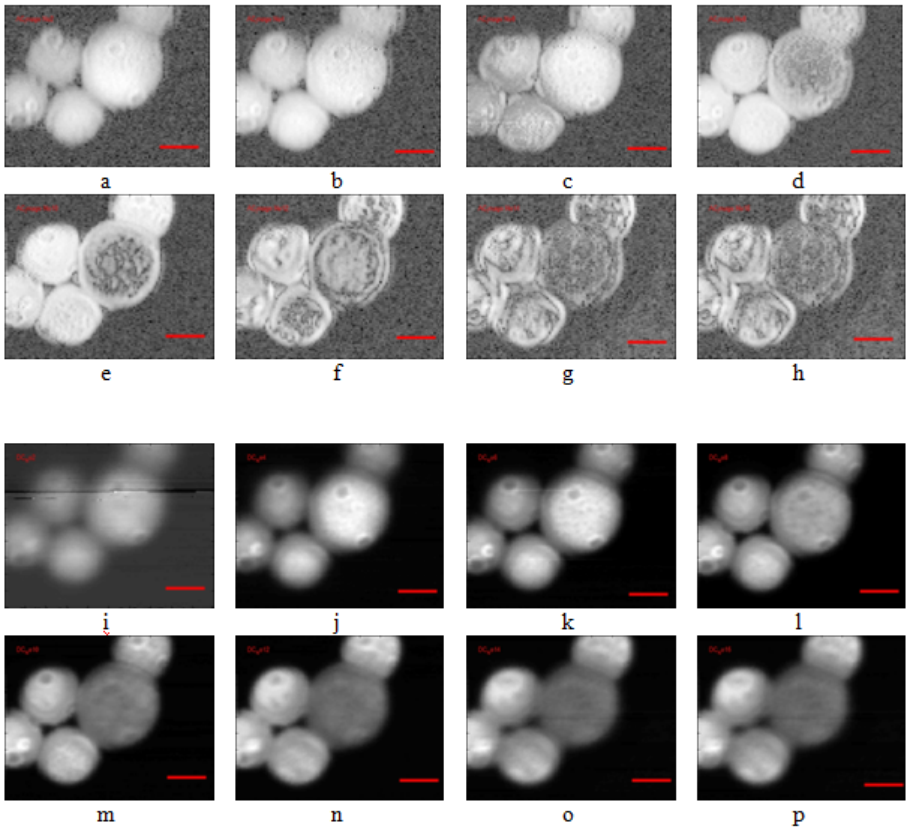

Figure 5.8: Image transition from shallow region to deeper region.
(a-h) Fluorescence images from the FMM method. (i-p) Fluorescence images from the CM method. The imaging spacing between successive images is about 10um. Imaging depth is around 100um. Scale bar: 10um

depth of 400 microns are shown in Figure 5.10. The cell density estimated from the FMM image (Figure 5.10b) is roughly equivalent to the result obtained from the shallower region. However the CM image (Fig. 5.10a) reveals a conflicting outcome, exhibiting an increased cell density. There is an exacerbation in the individual cell clarity for the CM image. A blown up image of the lower-left corner demarcated by the dotted lines is displayed in Figs. 5.10c and 5.10d for image qualities comparison. The FMM image still enables one to distinguish between individual cells and clumps of cells. However, in the CM image, it is wrecked by a cloud-like haze, offering little details and clues for characterization.

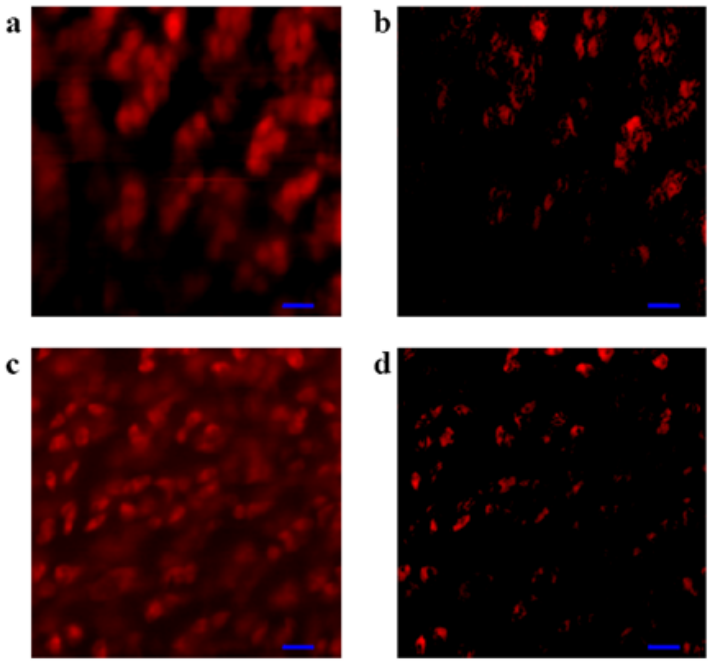

Figure 5.9: Fluorescence images of chondrocytes obtained from chicken cartilage At 220 (a and b) and 280 microns (c and d) depths. Confocal images (a and c) were acquired simultaneously with the corresponding FMM images (b and d). Scale bar: 20 microns.

5.5 Comparison with OCT

A comparison with OCT is done to authenticate FMM usefulness. This is done in conjunction with the development of an integrated dual mode microscope which adopt an hybrid imaging approach that marries OCT high depth imaging with FMM capability to provide molecular contrast. The dual mode microscope can equip clinicians and researcher alike with a better tool to trace biochemical variation as well as to elucidate the rationale behind the variations. The diagram Figure 5.11 below shows the conjugation of the OCT with the FMM system mentioned above.

Upon an imaging depth at approximately 217μm within tissue (refractive index of 1.38 assumed), collinear images of CM, FMM and OCM are presented. The fluorescence signal emitted from the liphophilic tracer stained on the cell membrane lit up

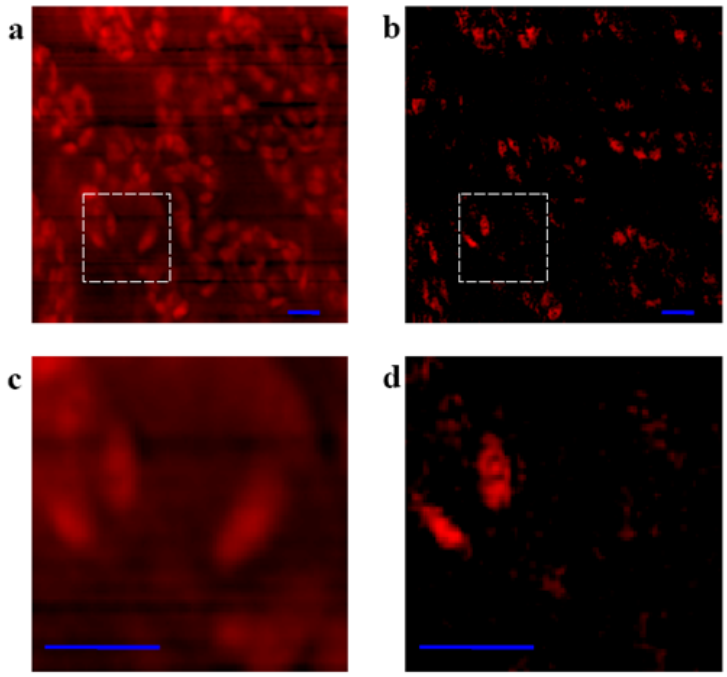

Figure 5.10: Images of chondrocytes obtained from chicken cartilage at a depth of 400 microns.
Confocal (a) and FMM (b) with (c and d) showing higher magnification view of the boxed regions in a and b, respectively. Scale bar: 20 microns

the images in CM and FMM (Figure 5.12 a & b). A ring like cluster was formed similar to the previous experiment done. The FMM image (Fig. 5.12 (b)) shows a high spatial resolution in comparison to that of CM, with stronger background rejection evidenced in the FMM cases. In the FMM image, the resolution and contrast of the image are restored owing to a stronger sectioning ability of the FMM. An alternative picture is depicted in the OCM image space (Figure 5.12c). Cells are instead identified by dark structures because the cytoplasm is non-scattering, and structures with relatively high scattering coefficient appear in the medial cell cluster region. However, the OCM depth of focus is almost twice as large as that of the FMM due to both the coherence length and confocal parameter, such that the cellular structures that are out of focus and rejected in FMM image appear in OCM image.

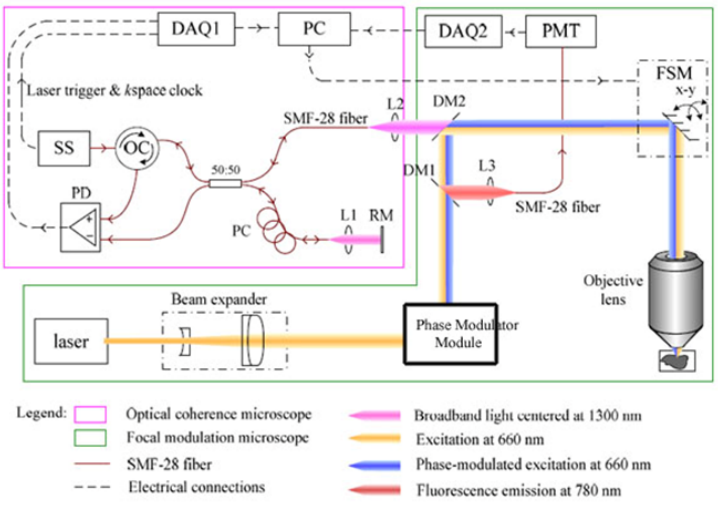

Figure 5.11: Dual mode microscope system layout.
Combination of a swept source OCT with the FMM. The fast scanning mirror is shared between the two setups. Certain optical mismatches between wavelength used is unfortunately present.

Figure. 5.13 shows collinear CM, FMM and OCM images of the same chicken cartilage at penetration depth of almost 300μm. In the CM imaging (Figure. 5.13a), cells are again shown as bright spots since the cell membrane is stained with the lipophilic tracer, with several cells forming a ring-like cell cluster. The FMM image (Figure. 5.13b) shows a high spatial resolution equivalent to that of CM, while much better background rejection is demonstrated in the FMM image. In the FMM image, the resolution and contrast of the image are restored owing to a stronger sectioning ability of the FMM than CM. In OCM image (Fig. 5.13c), cells are identified as dark structures because the cytoplasm is non-scattering, and structures with relative high scattering coefficient appear in the center of the cell cluster.

5.6 FMM advantages and limitations

Without usage of a long wavelength laser, FMM extends the imaging depth beyond that of the CM. FMM utilises single photon imaging and has access to a wide range of fluorescence dyes and probes that are denied to MPM or OCT (generally incapable of

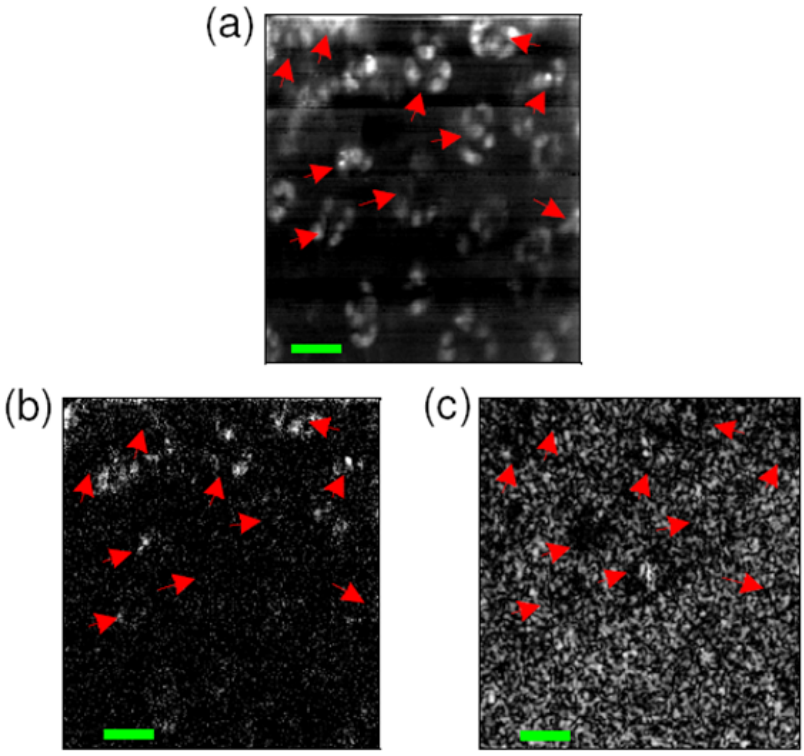

Figure 5.12: Images of chicken cartilage at the same location.
Acquired at depth of $\approx 200\mu m$ with (a) CM (b)FMM and (c) OCM Scale bar: $30\mu m$. Red arrows indicate the cell location. Cells appear as bright spots in FMM and CM while in OCM, cell is shown as dark structure. Speckles dominate in OCM image due to the presence of structure with high scattering coefficient.

fluorescence imaging). A key ongoing research focus is to derive dyes that fluoresce in the far red and near-IR spectrum. FMM could likewise benefit from such development. There would be a further gain in FMM imaging depth via adopting this far red dye.

MPM utilises expensive Femto second laser system which inhibits its widespread adoption due to high start-up and maintenance cost. FMM offers an inexpensive solution to the imaging depth problem. A simple modification to the CM illumination path and with further digital processing, one could derive the FMM signal. Direct FMM signal readint out can be easily obtained by incorporating a lock-in amplifier and read out the signal between the in-phase and off-phase signal. Such modification

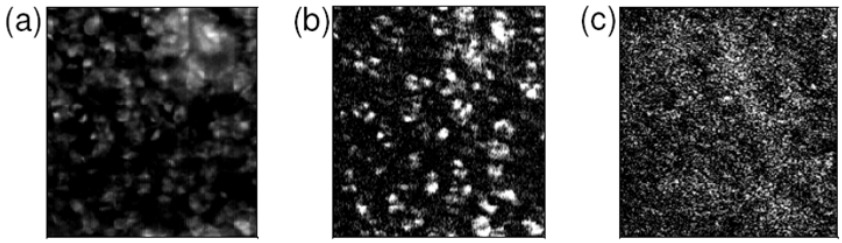

Figure 5.13: Images of chicken cartilage at the same location acquired at a depth of $\approx 300\mu m$ in air
with (a)CM (b) FMM and (c) OCM Image size: $200\mu m$ by $200\mu m$

could be implemented on an existing CM setup with add-on kits.

FMM usefulness lies in bridging the gap left open by problems faced in CM (low imaging depth) and OCT/MPM (lack of fluorescence, cost and complex setup). In samples dyed with multiple fluorescence labels, it is easier to utilise FMM over MPM as it is easier to find the matching label combination and to switch between lasers. It is not necessary for FMM to be utilised as a replacement technique but it could also be used to complement ongoing OCT research as shown in the study (Section. 5.5) above.

FMM is however, not without its limitation. FMM core technique rests on focal point modulation, spatial gating and heterodyne detection. FMM is a "non-suppression" technique ie it does little to inhibit scattering photon from exciting fluorescence. Focal modulation merely serves to "tag" ballistic photon with a temporal frequency marker and heighten detection selectivity. In contrary to MPM ("suppression" technique), fluorescence solely occur in the focal point where multi-photon interaction take place. Coupled with return detection path scattering, noise level is elevated and might threaten to overwhelm the detector with increase background, even with the spatial gating. Sifting for useful signal is no trivial task.

Modulation depth is an important criterion to determine the signal strength. The

FMM excitation signal is rated only at half CM excitation strength. In practice, less than half the excitation laser power goes into FMM. Further increase in laser power to improve signal strength eventually lead to bleaching and saturation. Laser power limitation imposes a ceiling to the maximal FMM signal for detection.

5.7 Discussion

From the study made above, the capability of the FMM is progressively tested. It is found to be consistently superior to CM with the above test results. The diverging of the point spread function due to scattering is averted by the selective excitation scheme utilised by FMM. Resolution and contrast integrity is upheld and its loss due to scattering is no longer the limiting factor for the imaging depth. On the other hand, CM images are plagued by loss of sectioning strength evidenced by the resolution loss and "ghost" image proliferation under increased scattering from deeper imaging region.

From the chicken cartilage test result, factors such as SBR and aberrations became predominant factor in determining the imaging depth. The FMM system SBR, as opposed to the much recognised parameter SNR, will ultimately determine the sensitivity and imaging depth. SBR is given as the ratio of signal against background noises. Background noises (from optical, electrical and sample) form the noise floor for practical microscopy system. Sample related noise is generally unavoidable. However, it would do well to improve imaging if one could economize the light usage and cut the accompanying noise found in laser and detection system. A high quality laser and low noise detector are essential to enhance the results obtained here.

The current study is still however lacking in quantitative measurement. A full complete study would require the measurement of the background (noise) as well as the signal. Thorough examination of the source, optical setup, sample and electronical noise, together with the signal generated, is required for a full bench marking and quantifying the FMM proficiency. Measures could then be taken to circumvent the

deficiencies introduced by the debilitating equipment.

Chapter 6

Conclusions and Future Directions

6.1 Introduction

For an emerging imaging modality to be fully adopted for clinical settings, stringent requirements have to be met. This chapter commences with a summary on the work done and the results achieved. The subsequent part of the chapter puts forth suggestions pertaining to the developmental direction that FMM could follow. Recommendations on fundamental research directions are given forth in the next section. Subsequent prototype system improvements are suggested. Finally, some novel developmental plans in new research areas where FMM could be adopted are raised.

6.2 Conclusion

The study has embarked forth by pointing out the limitation in optical imaging depth due to the scattering problem. From current literatures, various scattering "suppression" or "gating" methods have been reviewed. FMM is consequently proposed as an optical imaging technique which could vastly bolster the penetration depth without resorting to long wavelength excitation beam. An additional heterodyne "gate" is administered to complement the CM spatial gate. Both heuristic and theoretical model have been presented. Simulation studies have likewise demonstrated superior lateral and axial resolution as well as the higher SBR of FMM over CM. Through the

experimental study done with the prototype setup, the FMM superior depth imaging capability has been verified experimentally. Enhanced depth scattering rejection was shown in the images obtained in the Scheffelera Aribocola, embedded latex sphere and chicken cartilages. FMM has also been shown to complement imaging techniques such as OCT.

FMM therefore furnishes a novel technique in extending imaging depth without the imaging inhibitions faced by method such as OCT and MPM. However, in order for FMM to fully mature into a complete technique, numerous investigation and development works have to be carried out and these are pointed out in the following sections.

6.3 Fundamental Studies

Further theoretical studies works are required to explore and validate the FMM value and advantage. In order to gain further insights to FMM underlying mechanism, in depth theoretical studies on the coherence model with tissue should be done. Optimal operation parameters should also be uncovered to maximise FMM potential. Further analysis could be done in the following areas.

Abberation effect on FMM

Chapter 3 demonstrated the derivation of FMM OTF and PSF under an aberration-free assumption. In practical operation, laser light focused into a specimen of finite thickness, will incur aberration and results in wavefront distortion. This distortion is the consequence of the refractive index mismatch between medium and specimen.

Wavefront distortion alters the phase of the light field and in turn modifies the point spread function. In FMM, the spatial profile of the illumination and detection PSF are correlated to the modulation strength. With increasing aberration, the broadened yet reduced PSF would likely produce attenuated modulation strength and affect the imaging performance drastically.

FMM high numerical aperture performance is another promising direction that a researcher could investigate. The paraxial approximation allows for the simplification of OTF and PSF calculation through the application of Fourier Transform relationship. However, the apodization condition should be examined as the wavefront distribution differences in the spherical surface cannot be discounted. In addition, the deleterious effect of aberration is exacerbated with high numerical aperture objective. Some situations where aberration effects on FMM should be inspected include off-axis mismatched detector and lens defects.

Monte Carlo Study for multiscattered light

The theoretical study on FMM point spread function in Chapter 3 is a generalized method based on the first Born approximation. This approximation regards the specimen as a "weak object" in which propagating light suffers little absorption or scattering. In reality, this approximation does not hold with a thick specimen. Photons undergoes scattering in the following modes, leading to a broadened overall PSF.

i Photons propagating from light source to the focal spot.

ii Resultant fluorescence diffusing away from illumination spot back to detector.

Likewise in the detector plane, scattered photons are discriminated from the ballistic photons owing to the superior coherence gating mechanism. However, in practice, no gating mechanism is impervious to scattering effects. Multiscattered photons will nevertheless leak through, clouding out the detector to the point that the heterodyne signal blends into the background noise.

FMM effectiveness evaluation can be evaluated via rigorous quantitative study of the photons hit and miss rate through a Monte Carlo simulation. As pointed out in Chapter 2, Monte Carlo algorithms are a class of computer algorithm that rely on repeated random sampling to compute and derive possible outcomes. It is frequently used to simulate physical and mathematical system which cannot be modeled with

a deterministic algorithm. In optics, the Monte Carlo algorithm saw widespread application in calculation of photon transport, understanding their behavior in turbid media and for comparing experimental data to theory. Tissue characterization and optical system modelling can likewise be simulated and approximated through Monte Carlo multiple sampling trials.

The photon scattering effect can be measured in both excitation and the emission paths through Monte Carlo simulation. For the excitation path (shown in Figure 6.1), one major effect is that increased scattering leads to lower ballistic photons count, thus forming a broadened PSF (ballistic). Concurrently, there is an increment in diffuse photons reaching the in-focus region, resulting in an elevated background signal. Monte Carlo simulation could be utilised to predict the amount of scattered photons as well as analysing the ballistic photon number that could partake in the focal plane interference. Scalar diffraction is then used in conjunction to depict the interference effect and tag the interacting photons. The propagation of the tag photons (modulated) together with the background photon (noise) back to the detector could likewise be simulated by Monte Carlo simulation.

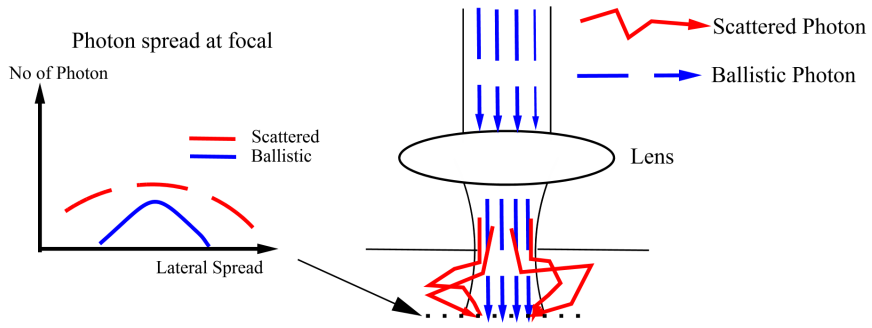

Figure 6.1: Scattering in excitation path

Pupil Excitation pattern optimisation

Different forms of pupil filters ie amplitude, phase and complex filters, have been introduced to improve the 3 dimensional resolution power of the optical imaging system. The main aim of the pupil filters are to improve the resolution either laterally, axially or both. This involves the creation of a narrow central irradiance lobe in either the lateral or axial direction or both. The resolution for an imaging system is dependent on the size of the main central lobes as well as the associated side lobes generated which introduced blurring. Lately, the polarization effect has been introduced to assist in the generation of the focal spot pattern.

For FMM, the system SNR depends on the modulation strength. Hence this solicits the generation of patterns which is alien to the normal conventional microscope and CM. A simple view of how the modulation is derived is via the difference of the in phase and out of phase peak intensity. Hence, for an in phase excitation pupil, intensity should be concentrated round the center lobe while for an out of phase excitation, irradiance divestment to the side lobes is required to achieve large deviation and subsequent high modulation strength. Optimised pupil design can be configured to cater to the specific requirement.

6.4 System design

The importance of the modulation scheme cannot be overly stressed. It is vital to design a stable modulation scheme which checks the noise introduced from nonlinearities and irregular motion. A shifting modulation frequency results in fluctuating fluorescence fringe signal which diminishes the useful signal. The FMM unique modulation scheme persists to be a main challenge in producing a viable FMM microscope system.

Annular ring based modulator

The modulator system forms the "heart" of the FMM modulation technique. The D-shaped phase pupil utilised in the prototype does not lend uniform lateral response compared to a ring annular based system. The ring annular system offers circular symmetric response, administering uniformity in the lateral and axial response.

The main trial in the modulator system development lies in the generation of the required modulation frequency. In order to conduct heterodyning, the modulation period has to be at least twice shorter than the scanning dwell time. For good signal response, the modulation frequency is required to be at least 5 times that of the scanning rate. A liquid crystal based phase modulator has the flexibility in the shaping the pupil but lacks the speed required for the FMM imaging purpose. A ferroelectric based modulator system boasts high speed modulation but lacks the phase variation flexibility.

6.5 Novel research direction

Fiber based FMM

The confocal pinhole can be replaced with a single mode fiber. Reciprocally, the fiber is operated as the instrument from which the excitation light is launched into the specimen. An optical fiber offers a great versatility in clinical bed side settings. Miniaturization of accompanying imaging components could allow for FMM to be employed for in-vivo optical imaging within inner organs of human beings.

The different fiber modes could be explored as another avenue to perform FMM. A variety of imaging modes exists from the mix and match which one could elect to choose to use for excitation and detection. This allows for different modulation pattern to be achieved.

Nonlinear FMM

One could regard FMM as an enhancement technique to the CM. Hence FMM techniques could likewise be applied in conjunction with non linear microscopy methods such as MPM, SHG and CARS microscopy technique. Non linear techniques appear on prima facie to give poor resolution due to the longer excitation wavelength used. However, these methods are not constrained by the want of a pinhole and the practical resolution offered by these methods often approaches the theoretical predicted value unlike in the case of CM. The combination of the two methods would allow for greater suppression of the scattering signal, offering greater depth penetration possibility.

Appendix A

Detailed derivation of FMM equation

The sample excitation field at the focal plane is given by

$$E_i(r_1) = h_{i1} + h_{i2} exp(2i\pi ft) \tag{A.1}$$

The equivalent intensity at the focal spot is then given by

$$\begin{aligned} I_i(r_1) &= |E_i(r_1)|^2 \\ &= E_i(r_1) \times E_i^*(r_1) \\ &= [h_{i1} + h_{i2} \exp(j2\pi ft)] \\ &\quad \times [h_{i1} + h_{i2} \exp(j2\pi ft)]^* \end{aligned} \tag{A.2}$$

Multiplying each components, we have

$$\begin{aligned} I_i(r_1) &= h_{i1}[h_{i1}]^* + h_{i2}\exp(j2\pi ft)[h_{i2}\exp(j2\pi ft)]^* \\ &\quad + h_{i1}[h_{i2}\exp(j2\pi ft)]^* + h_{i2}\exp(j2\pi ft)[h_{i1}]^* \\ &= |h_{i1}|^2 + |h_{i2}|^2 + 2Re(h_{i1}h_{i2}^* exp(j2\pi ft)) \end{aligned} \tag{A.3}$$

The equation above reduces to a form of an AM modulation. The demodulation can be retrieved through a physical circuit either in a coherent manner (synchronous detector) or incoherently (envelope detector). Hence the equation could be reexpressed by relating it to its envelope:

$$I_i(r_1) = |h_{i1}|^2 + |h_{i2}|^2 + 2|h_{i1}h_{i2}^*|\cos(2\pi ft + \theta_0)$$

where θ_0 is given by $\mathrm{Arg}(h_{i1}h_{i2}^*)$. Equivalently, the equation could also be reexpressed as

$$I_i(r_1) = |h_{i1}|^2 + |h_{i2}|^2 + 2Re(h_{i1}h_{i2}^*)\cos(2\pi ft) - 2Im(h_{i1}h_{i2}^*)\sin(2\pi ft)$$

Assuming that we have a ideal band pass filter and there is no other noise in the readout, we can likewise retrieve the signal magnitude through detecting the spectrum magnitude after converting the signal via Fourier Transform. The signal spectrum is shown in Figure A.1.

The DC value at the focal point is given by

$$I_{i_{DC}} = |h_{i1}|^2 + |h_{i2}|^2 \tag{A.4}$$

The heterodyne value at the focal point is given by

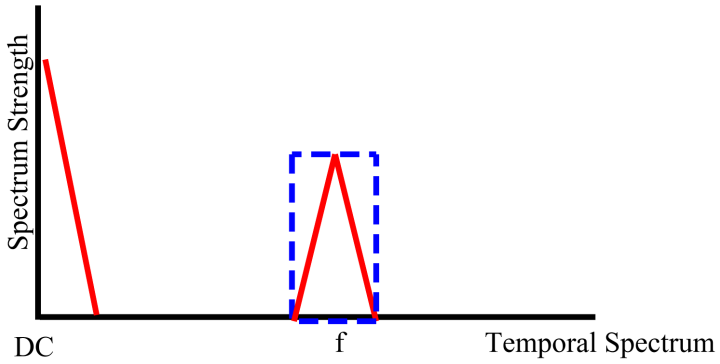

Figure A.1: Spectrum of intensity modulation at focal point.
The blue dashed outline indicate the ideal band pass filter bandwidth to extract the modulated signal

$$I_{i_{heterodyne}} = 2\left|h_{i1}h_{i2}^{*}\right| \tag{A.5}$$

Alternatively, we can detect the AM modulation index or essentially the term $|h_{i1}h_{i2}^{*}|$ through the difference from the in-phase (maximum) and off-phase (minimum) signal described by

$$\begin{aligned} I_{i_{in-phase}} &= DC + 2\left|h_{i1}h_{i2}^{*}\right| \\ \\ I_{i_{off-phase}} &= DC + 2\left|h_{i1}h_{i2}^{*}\right|\cos\left(\pi\right) \\ &= DC - 2\left|h_{i1}h_{i2}^{*}\right| \end{aligned}$$

Essentially, $2\pi ft + \theta_0$ is set to be 0^o in order to get the maximal signal and 180^o to get minimal signal. The actual modulation term $exp\left(j2\pi ft\right)$ for the pupil function is likewise modified to be $exp\left(0\right)$ and $exp\left(j\pi\right)$ for the maximal (in-phase) and minimum (off-phase) excitation signal respectively.

Therefore the difference of the two signal or the modulation term is given by

$$\begin{aligned} I_{i_{difference}} &= I_{i_{in-phase}} - I_{i_{off-phase}} \\ &= 4\left|h_{i1}h_{i2}^{*}\right| \end{aligned} \tag{A.6}$$

For the derivation of the IPSF, Equation A.6 is utilised. While for the calculation of the OTF, we return to Equation A.3:

$$I_i\left(r_1\right) = DC + 2Re\left(h_{i1}h_{i2}^{*}exp\left(j2\pi ft\right)\right)$$

Performing a Fourier Transform, the equation would yield

$$F\left\{I_i\left(r_1\right)\right\} = F\left\{DC\right\} + F\left\{Re\left(h_{i1}h_{i2}^{*}\right)\right\} \otimes \left[\delta\left(f - f_c\right)\right]$$

with f_c representing the pupil modulation frequency. Using the interpretation $Re\left[Z_1Z_2\right] = \frac{1}{2}\left(Z_1Z_2^{*} + Z_2Z_1^{*}\right)$,

$$OTF_{f_c} = F\left\{\left(h_{i1}h_{i2}^{*}\right) + \left(h_{i2}h_{i1}^{*}\right)\right\} \tag{A.7}$$

Appendix B

OTF Definition for unequal pupil

Assuming the pupil function be p_1 & p_2,

(A) $p_1 > p_2$

For $0 \leq l < p_1 - p_2$,

$$otf\,(l,s) = \begin{Bmatrix} \frac{2}{l} Re\left(\sqrt{(p_2)^2 - \left(\frac{s}{l} - \frac{l}{2}\right)^2}\right) & -l\left(p_2 - \frac{l}{2}\right) \leq s \leq l\left(p_2 + \frac{l}{2}\right) \\ 0 & otherwise \end{Bmatrix} \quad \text{(B.1)}$$

For $p_1 - p_2 \leq l \leq p_1 + p_2$,

$$otf\,(l,s) = \begin{Bmatrix} \frac{2}{l} Re\left(\sqrt{(p_1)^2 - \left(\frac{s}{l} + \frac{l}{2}\right)^2}\right) & \frac{(p_1)^2 - (p_2)^2}{2} \leq s \leq l\left(p_1 - \frac{l}{2}\right) \\ \frac{2}{l} Re\left(\sqrt{(p_2)^2 - \left(\frac{s}{l} - \frac{l}{2}\right)^2}\right) & -l\left(p_2 - \frac{l}{2}\right) \leq s \leq \frac{(p_1)^2 - (p_2)^2}{2} \\ 0 & otherwise \end{Bmatrix} \quad \text{(B.2)}$$

(B) $p_1 < p_2$

We made the following replacement to the equation shown above,

$$p_1 \Rightarrow p_2, \quad p_2 \Rightarrow p_1, \quad s \Rightarrow -s$$

Appendix C

Phase introduced by double reflective mirror

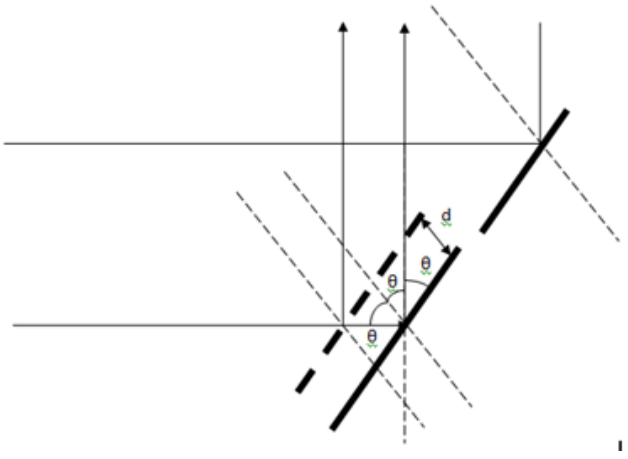

Figure C.1: Phase introduced by reflective plate

If we ignore the initial phase shift difference between the two plates, the path length difference is given by

$$\Delta OP = 2d \sin\theta \tag{C.1}$$

Given that the position function of the plate is a sinusoidal function,

$$\Delta OP = 2d\cos(wt)\sin\theta \tag{C.2}$$

And hence the phase is

$$\frac{d\varphi}{dt} = \frac{4\pi}{\lambda}d\cos(wt)\sin\theta \tag{C.3}$$

Appendix D

Phase introduced by tilting plate

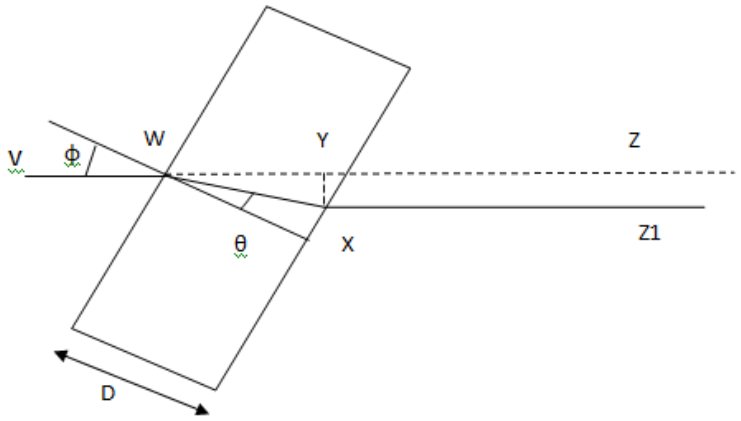

Figure D.1: Phase introduced by tilting transmission plate

$$\begin{aligned} \Delta OP &= OP_{new} - OP_{old} \\ &= n_1 L_{VW} + n_2 L_{WX} + n_1 L_{XZ1} - n_1 L_{VZ} \\ &= n_2 L_{WX} + n_1 L_{WY} \end{aligned} \tag{D.1}$$

Since n_1 is regarded as air, n_1 is taken to be 1.0,

$$\begin{aligned} L_{WX} &= \frac{D}{\cos\theta} \\ L_{WY} &= \frac{D}{\cos\theta}\cos\left(\theta-\phi\right) \end{aligned} \tag{D.2}$$

Making use of Snell's Law, $\sin\left(\phi\right) = n_2 \sin\left(\theta\right)$,

$$\begin{aligned} \Delta OP &= \frac{D}{\cos\theta}\left(n_2 - \cos\left(\theta-\phi\right)\right) \\ &= \frac{D}{\cos\theta}\left(n_2 - \cos\theta\cos\phi - \sin\theta\sin\phi\right) \end{aligned} \tag{D.3}$$

Applying Snell's Law,

$$\begin{aligned} \Delta OP &= \frac{D}{\cos\theta}\left(n_2 - n_2\sin^2\theta - \cos\theta\cos\phi\right) \\ &= D\left(\frac{n_2\left(1-\sin^2\theta\right)}{\cos\theta} - \cos\phi\right) \\ &= D\left(n_2\cos\theta - \cos\phi\right) \\ &= D\left(n_2\sqrt{1-\sin^2\theta} - \cos\phi\right) \\ &= D\left(n_2\sqrt{n_2^2 - n_2^2\sin^2\theta} - \cos\phi\right) \end{aligned} \tag{D.4}$$

The phase change introduced by the changing path length is given by

$$\begin{aligned} \Delta\psi\left(t\right) &= \Delta OP \times \frac{2\pi}{\lambda} \\ &= \frac{2\pi}{\lambda} D\left(\sqrt{n_2^2 - \sin^2\phi\left(t\right)} - \cos\phi\left(t\right)\right) \end{aligned} \tag{D.5}$$

The above equation showing the phase relationship with the tilting angle is then plotted in the Figure D.2

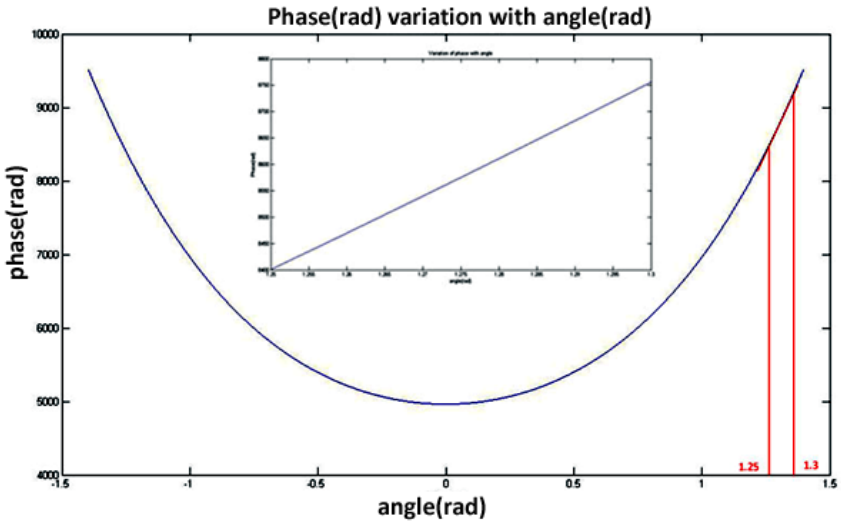

Figure D.2: Phase (rad) variation with angle (rad)
Insert: An exploded view of the phase vs angle relationship in the region between rad =1.25 and 1.3. A linear relationship is observed in this region.

From the Figure D.2, a linear response is observed in the region between radian = 1.25 and 1.3. In order for the tilt plate to operate in this region, the plate is initially aligned to the corresponding tilt angle (radian =1.275). This allows for a lower operation driving voltage. Another interesting observation shows that if the tilt plate is aligned close to zero tilt degree, the phase change does not respond to small changes in tilt angle. The resultant phase change is a constant. This is in agreement with the Taylor Expansion (not entirely shown here) done on Equation D.5. The Taylor coefficients for the odd power terms $(x, x^3, x^5.....)$ are zero.

Hence the Taylor Expansion, under small number approximation is:

$$\begin{aligned} \Delta\psi &= a_0 + a_2x^2 + a_4x^4 + a_6x^6 + ... \\ &\approx a_0 \end{aligned} \tag{D.6}$$

As the tilt angle, ϕ, is a time dependent function, the tilt angle corresponds linearly to an input voltage signal(galvoscanner operation)

$$\phi(t) = k_g triangle(\omega t) + \phi_0$$

where k_g is a constant factor determined by the galvoscanner and ϕ_0 is the initial operation tilt angle as mentioned above. Assuming k_g has a numeric value of 1, the phase variation against time, t, is then given by

$$\Delta\psi(t) = \frac{2\pi}{\lambda} D\left(\sqrt{n_2^2 - \sin^2(triangle(\omega t))} - \cos(triangle(\omega t))\right) \tag{D.7}$$

The final modulation intensity, $I(t)$, produced is simply given by

$$I(t) = \cos(\Delta\psi(t)) \tag{D.8}$$

A frequency of approximately 1kHz (Figure D.4) is obtained with a triangular wave control input of approximately 9Hz (Figure D.3).

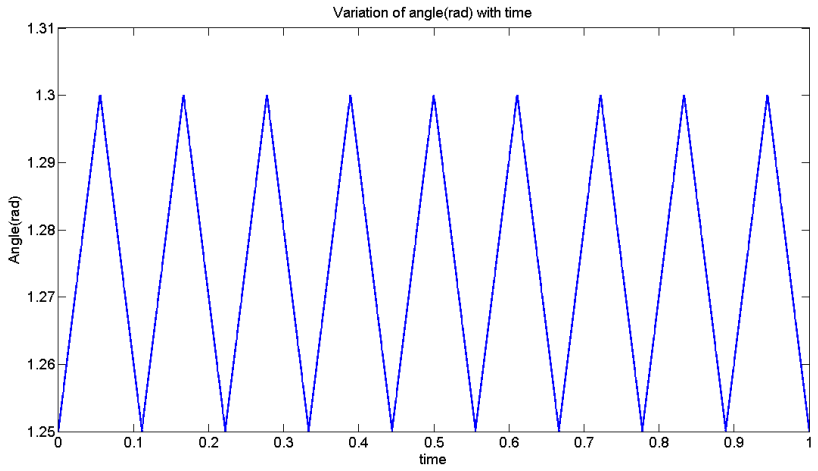

Figure D.3: Tilt control signal

A triangular signal wave of about $\approx$ 9Hz is supplied as input control.

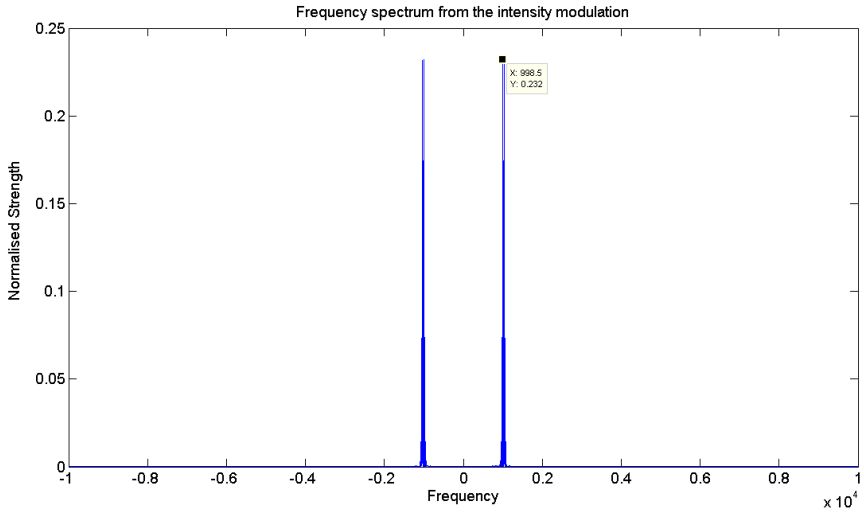

Figure D.4: Modulation intensity spectrum

The main frequency intensity spectrum peak is around 1kHz. Noise spike is found surrounding the central peak.

Appendix E

Publications

Journal

1 L. Liu, C. Liu, C. H. Wong, C. J. R. Sheppard, N. Chen, "Binary-phase spatial filter for real-time swept-source optical coherence microscopy," Opt. Lett., Vol. 32, 2375-2377 (2007)

2 N. Chen, C. Wong, and C. J. R. Sheppard, "Focal modulation microscopy," Opt. Express 16, 18764-18769 (2008).

3 Chee Howe Wong, Shau Poh Chong, Colin J. R. Sheppard, and Nanguang Chen, "Simple spatial phase modulator for focal modulation microscopy," Appl. Opt. 48, 3237-3242 (2009)

Patent

1 N.G. Chen, C.J.R Sheppard & C.H. Wong, "Fluorescence focal modulation microscopy system and method(wo/2009/008838)"(Patent Pending)

Conferences(only first author listed)

1 C.H. Wong, N.G. Chen, C.J.R Sheppard," Study on potential of structured illumination microscopy utilizing digital micromirror device for endoscopy purpose", IEEE ISBNM(2006)

2 C.H. Wong, L.B. Liu, C.J.R. Sheppard and N.G. Chen, "Penetration Depth Extension via Focal Modulation", 3rd Tohoku-NUS Symposium(2008)

3 Chee Howe Wong, Shau Poh Chong, Nanguang Chen, "Implementation of Spatial Phase Modulation for Focal Modulation Microscopy", OSA, Novel Techniques in Microscopy, Vancouver, Canada (2009)

Bibliography

[1] M. George, "Optical methods and sensors for in situ histology in surgery and endoscopy," *Min Invas Ther & Allied Technol*, vol. 13, no. 15, pp. 95–104, 2004.

[2] T. Xie, H. Xie, G. K. Fedder, and Y. Pan, "Endoscopic optical coherence tomography with a modified microelectromechanical systems mirror for detection of bladder cancers," *Appl. Opt.*, vol. 42, no. 31, pp. 6422–6426, 2003.

[3] R. O. Moreira, F. R. Trujillo, R. M. Meirelles, V. C. Ellinger, and L. Zagury, "Use of optical coherence tomography (oct) and indirect ophthalmoscopy in the diagnosis of macular edema in diabetic patients," *International Ophthalmology*, vol. 24, pp. 331–336, 2001.

[4] N. V. Iftimia, D. X. Hammer, C. E. Bigelow, T. Ustun, J. F. de Boer, and R. D. Ferguson, "Hybrid retinal imager using line-scanning laser ophthalmoscopy and spectral domain optical coherence tomography," *Optics Express*, vol. 14, no. 26, 2006.

[5] M. Cope, P. der Zee, S. Arridge, M. Essenpreis, C. Elwell, and D. Delpy, "Non-invasive measurement of tissue oxygenation using near infrared (nir) spectroscopy," in *Techniques and Biomedical Applications, IEE Colloquium on*, 1991, pp. 14/1–14/4.

[6] A. S. Haka, K. E. Shafer-Peltier, M. Fitzmaurice, J. Crowe, R. R. Dasari, and M. S. Feld, "Diagnosing breast cancer by using raman spectroscopy," *PNAS*, vol. 102, no. 35, pp. 12 371–12 376, 2005.

[7] A. E. Dixon, S. Damaskinos, and M. R. Atkinson, "A scanning confocal microscope for transmission and reflection imaging," *Nature*, vol. 351, pp. 551 – 553, 1991.

[8] W. Mo and N. Chen, "A novel implementation of time-domain diffusive optical tomography." in *Complex Medical Engineering, 2007. CME 2007. IEEE/ICME International Conference on*, 2007, pp. 1101–1104.

[9] *IEEE SIGNAL PROCESSING MAGAZINE*, vol. 3, Nov. 2001.

[10] A. G. Martin Schweiger and S. R. Arridge, "Computational aspects of diffuse optical tomography," *Computing in optics*, vol. 11-12, pp. 33–41, 2003.

[11] R. Parrish, A. Rox, and A. John, "The optics of human skin," *J Invest Dermatol*, vol. 77, pp. 13–19, 1981.

[12] T. Wilson and C. Sheppard, Eds., *Theory and Practice of Scanning Optical Microscopy*. London: Academic Press, 1984.

[13] T. Collier, M. Guillaud, M. Follen, A. Malpica, and R. Richards-Kortum, "Real-time reflectance confocal microscopy: comparison of two-dimensional images and three-dimensional image stacks for detection of cervical precancer," *Journal of Biomedical Optics*, vol. 12, p. 024021, 2007.

[14] J. M. Schmitt, "Optical coherence tomography (oct): a review," *IEEE JOURNAL OF SELECTED TOPICS IN QUANTUM ELECTRONICS*, vol. 5, no. 4, pp. 1205–1215, 1999.

[15] A. G. Podoleanu, G. M. Dobre, R. Cernat, J. A. Rogers, J. Pedro, R. B. Rosen, and P. Garcia, "Investigations of the eye fundus using a simultaneous optical coherence tomography/indocyanine green fluorescence imaging system." *Journal of Biomedical Optics*, vol. 12, p. 014019, 2007.

[16] Y. Xu, N. Iftimia, H. Jiang, L. L. Key, and M. B. Bolster, "Three-dimensional diffuse optical tomography of bones and joints." *Journal of Biomedical Optics*, vol. 7, p. 88, 2002.

[17] B. Alberts, A. Johnson, J. Lewis, M. Raff, K. Roberts, and P. Walter, Eds., *Cell.In Molecular Biology of the Cell.* Garland, 2002.

[18] W. Tan, A. Sendemir-Urkmez, L. Fahrner, R. Jamison, D. Leckband, and S. A. Boppart, "Structural and functional optical imaging of three-dimensional engineered tissue development," *Tissue Engineering*, vol. 10, no. 11/12, 2004.

[19] W. F. Cheong, S. A. Prahl, and A. J. Welch, "A review of the optical properties of biological tissues." *IEEE Journal of Quantum Electronics*, vol. 26, pp. 2166–2185, 1990.

[20] M. Minsky, "Microscopy apparatus," Patent 3,013,467, 1957.

[21] C. J. R. Sheppard and A. Choudhury, "Image formation in the scanning microscope." *Optica Acta*, vol. 24, pp. 1051–1073, 1977.

[22] M. Gu, T. Tannous, and C. J. R. Sheppard, "Effect of numerical aperture and annular pupil on confocal imaging through highly-scattering media." *Optics Letters*, vol. 21, pp. 312–314, 1996.

[23] C. J. R. Sheppard and R. Kompfner, "Resonant scanning optical microscope." *Applied Optics*, vol. 17, pp. 2879–2882, 1978.

[24] X. Deng and M. Gu, "Penetration depth of single-, two-, and three-photon fluorescence microscopic imaging through human cortex structures: Monte carlo simulation." *Applied Optics*, vol. 42, pp. 3321–3329, 2003.

[25] W. Denk, J. H. Strickler, and W. W. Webb, "Two-photon laser scanning fluorescence microscopy." *Science*, vol. 248, pp. 73–76, 1990.

[26] M. Oheim, E. Beaurepaire, E. Chaigneau, J. Mertz, and S. Charpak, "Two photon microscopy in brain tissue: parameters influencing the imaging depth." *J Neurosci Methods*, vol. 111, pp. 29–37, 2001.

[27] P. Theer, M. T. Hasan, and W. Denk, "Two-photon imaging to a depth of 1000 m in living brains by use of a ti:al2o3 regenerative amplifier." *Optics Letter*, vol. 28, pp. 1022–1024, 2003.

[28] D. Huang, E. A. Swanson, C. P. Lin, J. S. Schuman, W. G. Stinson, W. Chang, M. R. Hee, T. Flotte, K. Gregory, C. A. Puliafito, and J. G. Fujimoto, "Optical coherence tomography," *Science*, vol. 254, pp. 1178–1181, 1991.

[29] J. G. Fujimoto, "Optical coherence tomography for ultrahigh resolution in vivo imaging," *Nature Biotechnology*, vol. 21, pp. 1361–1367, 2003.

[30] S. R. Chin, E. A. Swanson, and J. G. Fujimoto, "Optical coherence tomography using a frequency-tunable optical source." *Optics Letters*, vol. 22, pp. 340–342, 1997.

[31] M. Choma, M. Sarunic, C. Yang, and J. Izatt, "Sensitivity advantage of swept source and fourier domain optical coherence tomography." *Optics Express*, vol. 11, pp. 2183–2189, 2003.

[32] M. R. Hee, J. A. Izatt, E. A. Swanson, D. Huang, J. S. Schuman, C. P. Lin, C. A. Puliafito, and J. G. Fujimoto, "Optical coherence tomography of the human retina." *Archives of Ophthalmology*, vol. 113, pp. 325–332, 1995.

[33] G. J. Tearney, M. E. Brezinski, B. E. Bouma, S. A. Boppart, C. Pitris, J. F. Southern, and J. G. Fujimoto, "In vivo endoscopic optical biopsy with optical coherence tomography." *Science*, vol. 276, pp. 2037–2039, 1997.

[34] W. Drexler, A. Baumgartner, O. Findl, C. K. Hitzenberger, H. Sattmann, and A. F. Fercher, "Submicrometer precision biometry of the anterior segment of the human eye." *Investigative Ophthalmology and Visual Science*, vol. 38, pp. 1304–1313, 1997.

[35] L. Rayleigh., "On the light from the sky, its polarization and colour." *Philos. Mag*, vol. 41, pp. 274–279, 1871.

[36] J. Tyndall, *Philos. Mag*, vol. 37, p. 384, 1869.

[37] P. Madden, "Light scattering studies of the dynamics and structure of liquids," *Philosophical Transactions of the Royal Society of London. Series A, Mathematical and Physical Sciences*, vol. 293, no. 1402, pp. 419–428, 1979.

[38] A. A. A. Abdel-Azim and P. Munk, "Light scattering of liquids and liquid mixtures. 1. compressibility of pure liquids," *J. Phys. Chem*, vol. 91, no. 14, pp. 3910–3914, 1987.

[39] A. Y. Val'kov, V. P. Romanov, and A. N. Shalaginov, "Fluctuations and light scattering in liquid crystals," *Phys.-Usp*, vol. 37, pp. 139–183, 1994.

[40] G. Ross, "Light scattering in amorphous media," *Journal of Modern Optics*, vol. 16, no. 1, pp. 95–109, 1969.

[41] B. T. Schaneberg, R. J. Molyneux, and I. A. Khan, "Evaporative light scattering detection of pyrrolizidine alkaloids," *Phytochemical Analysis*, vol. 15, no. 1, pp. 36–39, 2004.

[42] U. Kutzel, M. Vorbau, M. Stintz, T. Gottschalk-Gaudig, and H. Bartheland, "Dynamic light scattering for the characterization of polydisperse fractal systems: Ii. relation between structure and dls results," *Particle and Particle Systems Characterization*, vol. 25, no. 1, pp. 19–30, 2008.

[43] C. Z. Huang, Y. Liu, Y. Hong Wang, and H. Guo, "Resonance light scattering imaging detection of proteins with $\alpha, \beta, \gamma, \delta$-tetrakis(p-sulfophenyl)porinphyr," *Analytical Biochemistry*, vol. 321, no. 2, pp. 236–243, 2003.

[44] A. Liebert and R. Maniewsky, *Scattering: in Encyclopedia of Optical Engineering*, R. Driggers, Ed. New York: Marcel Dekker, 2003.

[45] W. Lihong and W. Hsin-i, *Biomedical Optics: Principles and Imaging.* Wiley-Interscience, 2007.

[46] Rayleigh scattering. [Online]. Available: http://www.philiplaven.com/p8b.html

[47] H. Naus and W. Ubachs, "Experimental verification of rayleigh scattering cross sections," *Optics Letter*, vol. 25, pp. 347–349, 2000.

[48] C. Bohren and D. Huffman, *Absorption and scattering of light by small particles.* 'New York: John Wiley, 1983.

[49] Blue sky. [Online]. Available: http://hyperphysics.phy-astr.gsu.edu/Hbase/atmos/blusky.html

[50] H. C. van de Hulst, *Light scattering by small particles*. 'New York: Dover, 1981.

[51] Robert and G. W. Brown, "Homodyne optical fiber dynamic light scattering," *Appl. Opt.*, vol. 40, pp. 4004–4010, 2001.

[52] K. Schutzel, "Correlation techniques in dynamic light scattering," *Appl. Phys. B*, vol. 42, 1987.

[53] B. J. Berne and R. Pecora, *Dynamic Light Scattering: With Applications to Chemistry, Biology, and Physics*. New York: Dover Publication, 2000.

[54] Y. Ozeki, F. Dake, S. Kajiyama, K. Fukui, and K. Itoh, "Analysis and experimental assessment of the sensitivity of stimulated raman scattering microscopy," *Opt. Express*, vol. 17, pp. 3651–3658, 2009.

[55] M. Kerker, "Founding fathers of light scattering and surface-enhanced raman scattering," *Appl. Opt.*, vol. 30, pp. 4699–4705, 1991.

[56] S. H. Melfi, K. D. Evans, J. Li, D. Whiteman, R. Ferrare, and G. Schwemmer, "Observation of raman scattering by cloud droplets in the atmosphere," *Appl. Opt.*, vol. 36, pp. 3551–3559, 1997.

[57] R. H. Stavn, "Effects of raman scattering across the visible spectrum in clear ocean water: a monte carlo study," *Appl. Opt.*, vol. 32, pp. 6853–6863, 1993.

[58] M. Ramsteiner, C. Wild, and J. Wagner, "Interference effects in the raman scattering intensity from thin films," *Appl. Opt.*, vol. 28, pp. 4017–4023, 1989.

[59] E. Tatsu, T. Sonehara, S. Ohno, S. Moriguchi, A. Koreeda, and S. Saikan, "Measurement of polarization dependence of nonlinear susceptibility responsible for rayleigh-wing and brillouin scattering," *Opt. Lett.*, vol. 29, pp. 2417–2419, 2004.

[60] J. H. Simmons and K. S. Potter, *Optical Materials*. San Diego: Academic Press, 2000.

[61] J. Randall and J. M. Vaughan, "The measurement and interpretation of brillouin scattering in the lens of the eye," *Opt. Lett.*, vol. 214, no. 1197, pp. 449–470, 1982.

[62] M. Winchester, L. Winchester, and N. Chou, "Application of raman scattering to the measurement of ligament tension," in *Engineering in Medicine and Biology Society, 2008. EMBS 2008. 30th Annual International Conference of the IEEE*, Aug. 2007, pp. 3434 – 3437.

[63] Z. Huang, S. K. Teh, W. Zheng, J. Mo, K. Lin, X. Shao, K. Y. Ho, M. Teh, and K. G. Yeoh, "Integrated raman spectroscopy and trimodal wide-field imaging techniques for real-time in vivo tissue raman measurements at endoscopy," *Opt. Lett.*, vol. 34, pp. 758–760, 2009.

[64] S. K. Teh, W. Zheng, K. Y. Ho, M. Teh, K. G. Yeoh, and Z. Huang, "Diagnostic potential of near-infrared raman spectroscopy in the stomach: differentiating dysplasia from normal tissue," *Br. J. Cancer*, vol. 98, p. 457, 2008.

[65] R. F. Begley, A. B. Harvey, and R. L. Byer, "Coherent anti-stokes raman spectroscopy," *Appl. Phys. Lett*, vol. 25, p. 387, 1974.

[66] A. K. Popp, M. T. Valentine, P. D. Kaplan, and D. A. Weitz, "Microscopic origin of light scattering in tissue," *Appl. Opt.*, vol. 42, pp. 2871–2880, 2003.

[67] V. V. Tuchin, "Microscopic origin of light scattering in tissue," *Appl. Opt.*, vol. 42, pp. 2871–2880, 2003.

[68] X. Y. Jiang, X. Q. Chen, Z. Dong, and M. Xu, "The application of resonance light scattering technique for the determination of tinidazole in drugs,," *J Autom Methods Manag Chem*, p. Article ID 86857, 2007.

[69] S. ClauBen, M. Janich, and R. Neubert, "Light scattering investigations on freeze-dried glucocorticoids in aqueous solution," *International Journal of Pharmaceutics*, vol. 252, pp. 267–270, 2003.

[70] Z. Chen, T. Song, S. Wang, X. Chen, J. Chen, and Y. Li, "Screen anticancer drug in vitro using resonance light scattering technique," *International Journal of Pharmaceutics*, vol. 77, no. 4, pp. 1365–1369, 2009.

[71] J. G. Fujimoto and D. Farkas, *Biomedical optical imaging*. Oxford university press, 2009.

[72] M. Yang, E. Baranov, P. Jiang, F. X. Sun, X. M. Li, L. Li, S. Hasegawa, M. Bouvet, M. Al-Tuwaijri, T. Chishima, H. Shimada, A. R. Moossa, S. Penman, and R. M. Hoffman, "Whole-body optical imaging of green fluorescent protein-expressing tumors and metastases," *PNAS*, vol. 97, no. 3, pp. 1206–1211, 2000.

[73] L. Li and L. V. Wang, "Optical coherence computed tomography," *Appl. Phys. Lett.*, vol. 91, p. 141107, 2007.

[74] M. Xu and L. V. Wang, "Photoacoustic imaging in biomedicine," *Rev. Sci. Instrum.*, vol. 77, p. 041101, 2006.

[75] N. S. Vorob'ev, V. M. Podgaetskii, A. V. Smirnov, S. A. Tereshchenko, and L. G. Tomilova, "Improvement of the optical imaging of objects in a strongly scattering medium by means of contrast-enhancing dyes," *Quantum Electronics*, vol. 29, pp. 1099–, 1999.

[76] O. Vargas, E. K. Chan, J. K. Barton, H. G. Rylander, and A. J. Welch, "Improvement of the optical imaging of objects in a strongly scattering medium by means of contrast-enhancing dyes," *Quantum Electronics*, vol. 29, pp. 1099–, 1999.

[77] M. R. Hee, J. A. Izatt, J. M. Jacobson, J. G. Fujimoto, and E. A. Swanson, "Femtosecond transillumination optical coherence tomography," *Opt. Lett.*, vol. 18, pp. 950–952, 1993.

[78] W. Mo and N. Chen, "Fast time-domain diffuse optical tomography using pseudorandom bit sequences," *Opt. Express.*, vol. 16, pp. 13 643–13 650, 2008.

[79] D. R. Leff, O. Warren, L. C. Enfield, A. P. Gibson, T. Athanasiou, D. K. Pattern, J. C. Hebden, G. Z. Yang, and A. Darzi, "Diffuse optical imaging of the healthy and diseased breast - a systematic review," *Breast Cancer Res. Treat*, vol. 108, pp. 9–22, 2008.

[80] M. A. Franceschini, D. K. Joseph, T. J. Huppert, S. G. Diamond, and D. A. Boas, "Diffuse optical imaging of the whole head," *J. Biomed. Opt.*, vol. 11, p. 054007, 2006.

[81] N. Chen and Q. Zhu, "Time-resolved diffusive optical imaging using pseudorandom bit sequences," *Opt. Express*, vol. 11, pp. 3445–3454, 2003.

[82] G. Indebetouw, "Distortion-free imaging through inhomogeneities by selective spatial-filtering," *Appl. Opt.*, vol. 29, pp. 5262–7, 1990.

[83] G. E. Anderson, F. Liu, and R. R. Alfano, "Microscope imaging through highly scattering media," *Appl. Opt.*, vol. 19, pp. 981–983, 1994.

[84] M. Rajadhyaksha, R. R. Anderson, and R. H. Webb, "Video-rate confocal scanning laser microscope for imaging human tissues in vivo," *Appl. Opt.*, vol. 38, pp. 2105–15, 1999.

[85] R. R. Alfano, X. Liang, L. Wang, and P. P. Ho, "Time-resolved imaging of translucent droplets in highly scattering turbid media," *Science*, vol. 264, p. 5167, 1994.

[86] K. M. Yoo and R. R. Alfano, "Time-resolved coherent and incoherent components of forward light-scattering in random-media," *Opt. Lett.*, vol. 15, pp. 320–322, 1990.

[87] P. Naulleau, E. Leith, H. Chen, B. Hoover, and J. Lopez, "Time-gated ensemble-averaged imaging through highly scattering media," *Appl. Opt.*, vol. 36, p. 3889, 1997.

[88] G. Stibenz and G. Steinmeyer, "Interferometric frequency-resolved optical gating," *Opt. Express*, vol. 13, p. 2617, 2005.

[89] G. Mitic, J. Koelzer, J. Otto, E. Plies, G. Soelkner, and W. Zinth, "Time-gated transillumination of biological tissues and tissuelike phantoms," *Appl. Opt.*, vol. 33, pp. 6699–6719, 1994.

[90] E. A. McLean, H. R. J. Burris, and M. P. Strand, "Short-pulse range-gated optical imaging in turbid water," *Appl. Opt.*, vol. 34, pp. 4343–4351, 1995.

[91] S. G. Demos and R. R. Alfano, "Temporal gating in highly scattering media by the degree of optical polarization," *Opt. Lett.*, vol. 21, pp. 161–163, 1996.

[92] K. M. Yoo, Q. R. Xing, and R. R. Alfano, "Imaging objects hidden in highly scattering media using femtosecond 2nd-harmonic-generation cross-correlation time gating," *Opt. Lett.*, vol. 16, pp. 1019–1021, 1991.

[93] J. G. Fujimoto, S. Desilvestri, E. P. Ippen, C. A. Puliafito, R. Margolis, and A. Oseroff, "Femtosecond optical ranging in biological-systems," *Opt. Lett.*, vol. 11, pp. 150–152, 1986.

[94] M. Feierabend, M. Rckel, and W. Denk, "Coherence-gated wave-front sensing in strongly scattering samples," *Opt. Lett.*, vol. 29, pp. 2255–2257, 2004.

[95] K. P. Chan, B. Devaraj, M. Yamada, and H. Inaba, "Coherent detection techniques in optical imaging of tissues," *Physics in Medicine and Biology*, vol. 42, p. 855, 1997.

[96] M. Kempe, A. Z. Genack, W. Rudolph, and P. Dorn, "Ballistic and diffuse light detection in confocal and heterodyne imaging systems,," *J. Opt. Soc. Am. A*, vol. 14, pp. 216–223, 1997.

[97] M. Ducros, M. Laubscher, B. Karamata, S. Bourquin, T. Lasser, and R. P. Salathe, "Barallel optical coherence tomography in scattering samples using a two-dimensional smart-pixel detector array," *Opt. Commun.*, vol. 202, pp. 29–35, 2002.

[98] A.Schmidt, R. Corey, and P. Saulnier, "Imaging through random media by use of low-coherence optical heterodyning," *Opt. Lett.*, vol. 20, pp. 404–, 1995.

[99] E. A. Swanson, J. A. Izatt, M. R. Hee, D. Huang, C. P. Lin, J. S. Schuman, C. A. Puliafito, and J. G. Fujimoto, "In vivo retinal imaging using optical coherence tomography,," *Opt. Lett.*, vol. 18, pp. 1864–1866, 1993.

[100] P. Dean, M. R. Dickinson, and D. P. West, "Full-field coherence-gated holographic imaging through scattering media using a photorefractive polymer composite device,," *Appl. Phys. Lett.*, vol. 85, p. 363, 2004.

[101] P. Yu, M. Mustata, J. J. Turek, P. M. W. French, M. R. Melloch, and D. D. Nolte, "Holographic optical coherence imaging of tumor spheroids,," *Appl. Phys. Lett.*, vol. 83, p. 575, 2003.

[102] M. P. Rowe, E. N. Pugh-Jr, J. S. Tyo, and N. Engheta, "Polarization-difference imaging: a biologically inspired technique for observation through scattering media,," *Opt. Lett.*, vol. 20, pp. 608–610, 1995.

[103] J. S. Tyo, M. P. Rowe, E. N. Pugh-Jr, and N. Engheta, "Polarization-difference imaging: a biologically inspired technique for observation through scattering media,," *Appl. Opt.*, vol. 35, pp. 1855–1870, 1996.

[104] J. S. Tyo, "Enhancement of the point-spread function for imaging in scattering media by use of polarization-difference imaging,," *J. Opt. Soc. Am.*, vol. 17, pp. 1–10, 2000.

[105] P. Gonzlez-Rodrguez and A. D. Ki, "Comparison of light scattering models for diffuse optical tomography,," *Opt. Express*, vol. 17, pp. 8756–8774, 2009.

[106] A. Ishimaru, *Wave Propagation and Scattering in Random Media.* New York: IEEE press, 1997.

[107] R. C. Haskell, L. O. Svaasand, T.-T. Tsay, T.-C. Feng, M. S. McAdams, and B. J. Tromberg, "Boundary conditions for the diffusion equation in radiative transfer,," *J. Opt. Soc. Am. A*, vol. 17, pp. 2727–2741, 1994.

[108] G. W. Faris, "Diffusion equation boundary conditions for the interface between turbid media: a comment,," *J. Opt. Soc. Am. A*, vol. 19, pp. 519–520, 2002.

[109] T. J. Farrell, M. S. Patterson, and B. Wilson, "A diffusion theory model of spatially resolved, steady-state diffuse reflectance for the noninvasive determination of tissue optical properties in vivo,," *Med. Phys.*, vol. 19, pp. 879–888, 1992.

[110] A. Ishimaru, "Diffusion of light in turbid material,," *Appl. Opt.*, vol. 28, pp. 2210–2215, 1989.

[111] M. Schweiger, S. Arridge, M. Hiraoka, and D. Delpy, "The finite element method for the propagation of light in scattering media: boundary and source conditions,," *Medical physics*, vol. 22, no. 11, pp. 1779–1792, 1995.

[112] L.-H. Wang and S. Jacques, "Hybrid model of monte carlo simulation and diffusion theory for light reflectance by turbid media,," *J. Optical Soc. Am. A*, vol. 10, pp. 1746–1752, 1993.

[113] L. Wang and S. Jacques, "Optimized radial and angular positions in monte carlo modeling." *Med. Phys.*, vol. 21, pp. 1081–1083, 1994.

[114] L.-H. Wang, S. Jacques, and L.-Q. Zheng, "Monte carlo modeling of photon transport in multi-layered tissues." *Computer Methods and Programs in Biomedicine*, vol. 47, pp. 131–146, 1995.

[115] L. Wang, S. Jacques, and L. Zheng, "Conv - convolution for responses to a finite diameter photon beam incident on multi-layered tissues," *Computer Methods and Programs in Biomedicine*, vol. 54, pp. 141–150, 1997.

[116] N. Chen, "Controlled monte carlo method for light propagation in tissue of semi-infinite geometry," *Appl. Opt.*, vol. 46, pp. 1597 – 1603, 2007.

[117] Histology. [Online]. Available: http://en.wikipedia.org/wiki/Histology

[118] J.-A. Conchello and J. Lichtman, "Optical sectioning microscopy," *Nat. Methods*, vol. 2, pp. 920–931, 2005.

[119] K. Wilson and J. M. Walker, *Principles and Techniques of Biochemistry and Molecular Biology*. Cambridge University Press, 2005.

[120] R. Goldman and D. L. Spector, *Live cell imaging : a laboratory manual*. Cold Spring Harbor Laboratory Press, 2005.

[121] J. G. White, W. B. Amos, and M. Fordham, "An evaluation of confocal versus conventional imaging of biological structures by fluorescence light microscopy," *Journal of Cell Biology*, vol. 105, pp. 41–48, 1987.

[122] R. Hofman, J. Segenhout, and H. Wit, "Three-dimensional reconstruction of the guinea pig inner ear, comparison of opfos and light microscopy, applications of 3d reconstruction," *Journal of Microscopy*, vol. 233, no. 2, pp. 251–257, 2009.

[123] S. Kikuchi, K. Sonobe, S. Mashiko, Y. Hiraoka, and N. Ohyama, "Three-dimensional image reconstruction for biological micro-specimens using a double-axis fluorescence microscope," *Optics Communications*, vol. 138, no. 1-3, pp. 21–26, 1997.

[124] S. L. Shorte and F. Frischknecht, *Imaging Cellular and Molecular Biological Functions*. Springer, 2007.

[125] J. Itoh, K. Kawai, A. Serizawa, K. Yasumura, K. Ogawa, and R. Osamura, "A new approach to three-dimensional reconstructed imaging of hormone-secreting cells and their microvessel environments in rat pituitary glands by confocal laser scanning microscopy," *J. Histochem. Cytochem.*, vol. 48, pp. 569–578, 2000.

[126] J.-A. Conchello, J. Kim, and E. Hansen, "Enhanced 3d reconstruction from confocal scanning microscope images. ii: depth discrimination vs. signal-to-noise ratio in partially confocal images." *Appl. Opt.*, vol. 33, pp. 3740–3750, 1994.

[127] J. Pawley, *Handbook of Biological Confocal Microscopy*. Springer, 2006.

[128] S. W. Paddock, *Confocal microscopy methods and protocols.* Humana Press, 1999.

[129] C. Sheppard and D. Shotton, *Confocal laser scanning microscopy.* Springer, 1998.

[130] C. Sheppard, D. Hamilton, and I. Cox, "Optical microscopy with extended depth of field." *Proc. R. Soc. Lond. A*, vol. 387, pp. 171–186, 1983.

[131] M. Gu, *Principles of three dimensional imaging in confocal microscopes.* Singapore: World Scientific, 1996.

[132] M. Minsky., "Memoir on inventing the confocal scanning microscope." *Scanning*, vol. 10, pp. 128–138, 1988.

[133] T. Wilson and A. R. Carlini, "Effect of detector displacement in confocal imaging systems," *Appl. Opt.*, vol. 27, pp. 3791–3799, 1988.

[134] T.Wilson and A. R. Carlini, "Size of the detector in confocal imaging systems," *Opt. Lett.*, vol. 12, pp. 227–229, 1987.

[135] C. J. Koester, S. M. Khanna, H. D. Rosskothen, R. B. Tackaberry, and M. Ulfendahl, "Confocal slit divided-aperture microscope: applications in ear research," *Appl. Opt.*, vol. 33, pp. 702–708, 1994.

[136] Theory of confocal microscope: Resolution and contrast in confocal microscopy, olympus fluoview resource center. [Online]. Available: http://www.olympusconfocal.com/theory/resolutionintro.html

[137] Lateral and axial resolution in confocal microsope:advanced microscopy unit. [Online]. Available: http://www.hi.helsinki.fi/amu/AMU%20Cf_tut/cf_tut_part1-5.htm

[138] C. Sheppard and M. Sharma, "Integrated intensity and confocal imaging through scattering media," *Journal of Modern Optics*, vol. 48, no. 9, pp. 1517–1525, 2001.

[139] J. M. Schmitt, A. Knuttel, and M. Yadlowsky, "Confocal microscopy in turbid media," *J. Opt. Soc. Am. A*, vol. 11, pp. 2226–2235, 1994.

[140] M. Kempe, W. Rudolph, and E. Welsch, "Comparative study of confocal and heterodyne microscopy for imaging throughscattering media," *J. Opt. Soc. Am. A*, vol. 13, pp. 46–52, 1996.

[141] M. Kempe, A. Thon, and W. Rudolph, "Resolution limits of microscopy through scattering layers," *Opt. Commun.*, vol. 110, pp. 492–496, 1994.

[142] J. A. Moon and J. Reintjes, "Image resolution by use of multiply scattered light," *Opt. Lett.*, vol. 19, pp. 521–523, 1994.

[143] B. R. Masters, *Confocal microscopy and multiphoton excitation microscopy.* Singapore: SPIE Press, 2006.

[144] M. Mller, *Introduction to Confocal Fluorescence Microscopy.* Singapore: SPIE Press, 2005.

[145] A. K. Dunn, C. Smithpeter, A. J. Welch, and R. Richards-Kortum, "Sources of contrast in confocal reflectance imaging," *Appl. Opt.*, vol. 35, pp. 3441–3446, 1996.

[146] M. Schrader, S. W. Hell, and H. T. M. van der Voort, "Potential of confocal microscopes to resolve in the 50-100 nm range," *Appl. Phys. Lett.*, vol. 69, no. 24, pp. 3441–3446, 1996.

[147] C. L. Smithpeter, A. K. Dunn, A. J. Welch, and R. Richards-Kortum, "Penetration depth limits of in vivo confocal reflectance imaging," *Appl. Opt.*, vol. 37, pp. 2749–2754, 1998.

[148] X.Gan, S.Schilders, and M.Gu, "Combination of annular aperture and polarization gating methods for efficient microscopic imaging through a turbid medium: Theoretical analysis," *Microscopy and Microanalysis*, vol. 3, no. 6, pp. 495–503, 1997.

[149] T. D. Wang, M. J. Mandella, C. H. Contag, and G. S. Kino, "Dual-axis confocal microscope for high-resolution in vivo imaging," *Opt. Lett.*, vol. 28, pp. 414–416, 2003.

[150] M. Winchester, L. Winchester, and N. Chou, "The scanning harmonic optical microscope," in *IEEE/OSA Conf. Laser Engineering and Applications Washington*, 1977.

[151] C. J. Juergen and J. S. Mark, "Multiphoton endoscopy," *Opt. Lett.*, vol. 28, pp. 902–904, 2003.

[152] H.-S. Lee, Y. Liu, H.-C. Chen, L.-L. Chiou, G.-T. Huang, W. Lo, and C.-Y. Dong, "Optical biopsy of liver fibrosis by use of multiphoton microscopy," *Opt. Lett.*, vol. 29, pp. 2614–2616, 2004.

[153] W. Zipfel, R. Williams, and W. Webb, "Nonlinear magic: multiphoton microscopy in the biosciences," *Nature Biotechnology*, vol. 21, pp. 1369–1377, 2003.

[154] D. W. Piston, "Imaging living cells and tissues by two-photon excitation microscopy." *Trends Cell Biol.*, vol. 9, no. 2, pp. 66–69, 1999.

[155] M. Goeppert-Mayer, "Elementary processes with two-quantum transitions." *Ann. d. Physik.*, vol. 9, p. 273, 1931.

[156] E. W. V. Stryland, M. A. Woodall, H. Vanherzeele, and M. J. Soileau, "Energy band-gap dependence of two-photon absorption." *Opt. Lett.*, vol. 10, pp. 490–492, 1985.

[157] C. Rulliere, *Femtosecond Laser Pulses: Principles and Experiments.* Springer, 2004.

[158] Coherent inc: Mira 900 brochure. [Online]. Available: http://www.coherent.com/downloads/Mira900Brochure.pdf

[159] M. Gu and C. Sheppard, "Effects of a finite-sized pinhole on 3-d image formation in confocal two-photon fluorescence microscopy." *J. Mod. Opt.*, vol. 40, pp. 2009–2024, 1993.

[160] R. Gauderon and C. Sheppard, "Effect of a finite-sized pinhole on noise performance in single-, two-, and three-photon confocal fluorescence microscopy." *Appl. Opt.*, vol. 38, pp. 3562–3565, 1999.

[161] R. Gauderon, P. Lukins, and C. Sheppard, "Effect of a confocal pinhole in two-photon microscopy," *Microsc. Res. and Tech.*, vol. 47, pp. 210–214, 1999.

[162] R. M. Barry and P. So, *Handbook of Biomedical Nonlinear Optical Microscopy.* USA: Oxford University Press, 2008.

[163] E. Beaurepaire, M. Oheim, and J. Mertz, "Ultra-deep two-photon fluorescence excitation in turbid media," *Opt.Commun.*, vol. 188, pp. 25–9, 2001.

[164] M. B. Lilledahl, O. A. Haugen, C. de Lange Davies, and L. O. Svaasand, "Characterization of vulnerable plaques by multiphoton microscopy," *J. Biomed. Opt.*, vol. 12, no. 4, p. 044005, 2007.

[165] V. Andresen, S. Alexander, W.-M. Heupel, M. Hirschberg, R. M. Hoffman, and P. Friedl, "Infrared multiphoton microscopy: subcellular-resolved deep tissue imaging." *Current Opinion in Biotechnology*, vol. 20, no. 1, pp. 54–62, 2009.

[166] F. Helmchen and W. Denk, "Deep tissue two-photon microscopy." *Nature Methods*, vol. 2, pp. 932–940, 2005.

[167] A. Leray and J. Mertz, "Rejection of two-photon fluorescence background in thick tissue by differential aberration imaging." *Opt. Express*, vol. 14, pp. 10 565–10 573, 2006.

[168] J. Ying, F. Liu, and R. R. Alfano, "Spatial distribution of two-photon-excited fluorescence in scattering media." *Appl. Opt.*, vol. 38, pp. 224–229, 1999.

[169] A. F. Fercher, "Optical coherence tomography - principles and applications," *Rep. Prog. Phys.*, vol. 66, pp. 239–303, 2003.

[170] L. Liu and N. G. Chen, "Double-pass rotary mirror array for fast scanning optical delay line," *Appl. Opt.*, vol. 45, pp. 5426–5431, 2006.

[171] L. Liu, N. Chen, and C. J. R. Sheppard, "Double-reflection polygon mirror for high-speed optical coherence microscopy," *Opt. Lett.*, vol. 32, pp. 3528–3530, 2007.

[172] L. Liu, C. Liu, C. H. Wong, C. J. R. Sheppard, and N. Chen, "Binary-phase spatial filter for real-time swept-source optical coherence microscopy," *Opt. Lett.*, vol. 32, pp. 2375–2377, 2007.

[173] L. M. Smith and C. C. Dobson, "Absolute displacement measurements using modulation of the spectrum of white light in a michelson interferometer," *Appl.Opt.*, vol. 28, pp. 3339–3342, 1981.

[174] A. F. Fercher, C. K. Hitzenberger, G. Kamp, and S. Y. El-Zaiat, "Measurements of intraocular distances by backscattering spectral interferometry," *Optics Communications*, vol. 117, pp. 43–48, 1995.

[175] A. Bachmann, R. Leitgeb, , and T. Lasser, "Heterodyne fourier domain optical coherence tomography for full range probing with high axial resolution," *Opt. Express*, vol. 14, pp. 1487–1496, 2006.

[176] G. Hausler and M. W. Lindner, "Coherence radar and spectral radar - new tools for dermatological diagnosis," *J. Biomed. Optics*, vol. 3, pp. 21–31, 1998.

[177] P. Blazkiewicz, M. Gourlay, J. R. Tucker, A. D. Rakic, and A. V. Zvyagin, "Signal-to-noise ratio study of full-field fourier-domain optical coherence tomography," *Appl. Opt.*, vol. 44, pp. 7722–7729, 2005.

[178] E. Beaurepaire, A. C. Boccara, M. Lebec, L. Blanchot, and H. Saint-Jalmes, "Full-field optical coherence microscopy," *Opt. Lett.*, vol. 23, pp. 244–246, 1998.

[179] M. Brezinski and J. Fujimoto, "Optical coherence tomography: high-resolution imaging in nontransparent tissue," *IEEE Journal of Selected Topics in Quantum Electronics*, vol. 5, no. 4, pp. 1185 – 1192, 1999.

[180] W. Drexler and J. G. Fujimoto, *Optical Coherence Tomography: Technology And Applications*. Springer Verlag, 2008.

[181] B. E. Bouma and G. J. Tearney, *Handbook of Optical Coherence Tomography*. Informa HealthCare, 2001.

[182] M. R. Hee, J. A. Izatt, E. A. Swanson, D. Huang, J. S. Schuman, C. P. Lin, C. A. Puliafito, and J. G. Fujimoto, "Optical coherence tomography: high-resolution imaging in nontransparent tissue," *Arch. Ophthalmol.*, vol. 113, pp. 325–332, 1995.

[183] S. Yazdanfar, A. M. Rollins, and J. A. Izatt, "Imaging and velocimetry of the human retinal circulation with color doppler optical coherence tomography," *Opt.Lett.*, vol. 25, pp. 1448–1450, 2000.

[184] D. Huang, M. R. Chalita, Y. Li, C. Y. Lowder, D. M. Meisler, A. M. Rollins, and J. A. Izatt, "High-speed optical coherence tomography of anterior segment surgical anatomy and pathology," *Invest. Ophthalmol. Vis. Sci.*, vol. 44, pp. U141–Ul41, 2003.

[185] Y. Li, M. R. Chalita, J. Goldsmith, V. Westphal, B. A. Bower, R. Shekhar, A. M. Rollins, J. A. Izatt, and D. Huang, "Automated anterior chamber biometry with high-speed optical coherence tomography," *Invest. Ophthalmol. Vis. Sci.*, vol. 44, pp. U285–U285, 2003.

[186] S. Radhakrishnan, A. M. Rollins, J. E. Roth, S. Yazdanfar, V. Westphal, D. S.Bardenstein, and J. A. Izatt, "Real-time optical coherence tomography of the anterior segment at 1310 nm," *Arch. Ophthalmol.*, vol. 119, pp. 1179–1185, 2001.

[187] M. E. Brezinski, G. J. Tearney, B. E. Bouma, J. A. Izatt, M. R. Hee, E. A. Swanson, J. F. Southern, and J. G. Fujimoto, "Optical coherence tomography for optical biopsy-properties and demonstration of vascular pathology," *Circulation*, vol. 93, pp. 1206–1213, 1996.

[188] G. J. Tearney and B. E. Bouma, "Atherosclerotic plaque characterization by spatial and temporal speckle pattern analysis," *Opt. Lett.*, vol. 27, pp. 533–535, 2002.

[189] A. Das, M. V. Sivak, A. Chak, R. C. Wong, V. Westphal, A. M. Rollins, J. Izatt, G. A. Isenberg, and J. Willis, "Role of high resolution endoscopic imaging using optical coherence tomography (oct) in patients with barrett's esophagus (be)," *Gastrointest. Endosc.*, vol. 51, pp. AB93–AB93, 2000.

[190] M. V. Sivak, K. Kobayashi, J. A. Izatt, A. M. Rollins, R. Ungmnyawee, A. Chak, R. C. K. Wong, G. A. Isenberg, and J. Willis, "High-resolution endoscopic imaging of the gi tract using optical coherence tomography," *Gustruintest. Endosc.*, vol. 51, pp. 474–479, 2000.

[191] A. M. Rollins, R. Ung-arunyawee, A. Chak, R. C. K. Wong, K. Kobayashi, M. V. Sivak, and J. A. Izatt, "Real-time in vivo imaging of human gastrointestinal ultrastructure by use of endoscopic optical coherence tomography with a novel efficient interferometer design," *Opt. Lett.*, vol. 24, pp. 1358–1360, 1999.

[192] E. Beaurepaire, L. Moreaux, F. Amblard, and J. Mertz, "Combined scanning optical coherence and two-photon-excited fluorescence microscopy," *Opt. Lett.*, vol. 24, pp. 969–971, 1999.

[193] J. Dunkers, M. Cicerone, and N. Washburn, "Collinear optical coherence and confocal fluorescence microscopies for tissue engineering," *Opt. Express*, vol. 11, pp. 3074–3079, 2003.

[194] J. McNally, T. Karpova, J. Cooper, and J. Conchello, "Three-dimensional imaging by deconvolution microscopy," *Methods.*, vol. 19, no. 3, pp. 373–385, 1999.

[195] P. Shaw, "Deconvolution in 3-d optical microscopy," *The Histochemical Journal*, vol. 26, no. 3, pp. 687–694, 1994.

[196] B. Vermolen, Y. Garini, and Y. IT, "3d restoration with multiple images acquired by a modified conventional microscope," *Microsc Res Tech*, vol. 64, no. 2, pp. 113–25,, 2004.

[197] Y. Hiraoka, J. Sedat, and D. Agard, "The use of a charge-coupled device for quantitative optical microscopy of biological structures," *Science*, vol. 238, no. 4823, pp. 36–41, 1987.

[198] J. G. McNally, C. Preza, J.-A. Conchello, and L. J. Thomas, "Artifacts in computational optical-sectioning microscopy," *J. Opt. Soc. Am. A*, vol. 11, pp. 1056–1067, 1994.

[199] J. Markham and J.-A. Conchello, "Parametric blind deconvolution: a robust method for the simultaneous estimation of image and blur," *J. Opt. Soc. Am. A*, vol. 16, pp. 2377–2391, 1999.

[200] J. Swoger, P. Verveer, K. Greger, J. Huisken, and E. H. K. Stelzer, "Multi-view image fusion improves resolution in three-dimensional microscopy," *Opt. Express*, vol. 15, pp. 8029–8042, 2007.

[201] Y. Liu, Y. Liang, G. Mu, and X. Zhu, "Deconvolution methods for image deblurring in optical coherence tomography," *J. Opt. Soc. Am. A*, vol. 26, pp. 72–77, 2009.

[202] T. S. Ralston, D. L. Marks, F. Kamalabadi, and S. A. Boppart, "Deconvolution methods for mitigation of transversal blurring in optical coherence tomography," *IEEE Trans. Image Process.*, vol. 14, pp. 1254–1264, 2005.

[203] C. Vinegoni, T. Ralston, W. Tan, W. Luo, D. Marks, and S. Boppart, "Integrated structural and functional optical imaging combining spectral-domain optical coherence and multiphoton microscopy," *Appl. Phys. Lett.*, vol. 88, p. 053901, 2006.

[204] S. Tang, T. B. Krasieva, Z. Chen, and B. J. Tromberg, "Combined multiphoton microscopy and optical coherence tomography using a 12-fs broadband source," *J. Biomed. Opt.*, vol. 11, p. 20502, 2006.

[205] M. A. A. Neil, R. Juskaitis, and T. Wilson, "Method of obtaining optical sectioning by using structured light in a conventional microscope," *Opt. Lett.*, vol. 22, pp. 1905–1907, 1997.

[206] D. Dbarre, E. J. Botcherby, M. J. Booth, and T. Wilson, "Adaptive optics for structured illumination microscopy," *Opt. Express*, vol. 16, pp. 9290–9305, 2008.

[207] S. Delica and C. M. Blanca, "Wide-field depth-sectioning fluorescence microscopy using projector-generated patterned illumination," *Appl. Opt.*, vol. 46, pp. 7237–7243, 2007.

[208] J. Siegel, D. S. Elson, S. E. D. Webb, D. Parsons-Karavassilis, S. Lvque-Fort, M. J. Cole, M. J. Lever, P. M. W. French, M. A. A. Neil, R. Juskaitis, L. O. Sucharov, and T. Wilson, "Whole-field five-dimensional fluorescence microscopy combining lifetime and spectral resolution with optical sectioning," *Opt. Lett.*, vol. 26, pp. 1338–1340, 2001.

[209] C. Wong, N. Chen, and C. Sheppard, "Study on potential of structured illumination microscopy utilizing digital micromirror device for endoscopy purpose," in *IEEE ISBNM*, 2006.

[210] D. Scharstein and R. Szeliski, "High-accuracy stereo depth maps using structured light," in *In IEEE Computer Society Conference on Computer Vision and Pattern Recognition (CVPR 2003), Vol 1*, 2003, pp. 195–202.

[211] R. A. Morano, C. Ozturk, R. Conn, S. Dubin, S. Zietz, and J. Nissanov, "Structured light using pseudorandom codes," *IEEE Transactions on Pattern Analysis and Machine Intelligence*, vol. 20, no. 3, pp. 322–327, 1998.

[212] R. Heintzmann, T. M. Jovin, and C. Cremer, "Saturated patterned excitation microscopy-a concept for optical resolution improvement," *J. Opt. Soc. Am. A*, vol. 19, pp. 1599–1609, 2002.

[213] V. Poher, H. X. Zhang, G. T. Kennedy, C. Griffin, S. Oddos, E. Gu, D. S. Elson, M. Girkin, P. M. W. French, M. D. Dawson, and M. A. Neil, "Optical sectioning microscopes with no moving parts using a micro-stripe array light emitting diode," *Opt. Express*, vol. 15, pp. 11 196–11 206, 2007.

[214] L. G. Krzewina and M. K. Kim, "Single-exposure optical sectioning by color structured illumination microscopy," *Opt. Lett.*, vol. 31, pp. 477–479, 2006.

[215] A. Weigel, D. Schild, and A. Zeu, "Resolution in the apotome and the confocal laser scanning microscope: comparison," *J Biomed.Opt*, vol. 14, no. 1, p. 014022, 2009.

[216] F. Chasles, B. Dubertret, and A. C. Boccar, "Optimization and characterization of a structured illumination microscope," *Opt. Express*, vol. 15, pp. 16 130–16 140, 2007.

[217] M. Neil, C. Dunsby, and P. Lanigan, "Noise in structured illumination microscopes," in *Invited talk at ICONA meeting, Hakone Japan*, 2004. [Online]. Available: http://www.imperial.ac.uk/research/photonics/about/staff/icona.pdf

[218] G. Herbert, *Chapter 7: Handbook of Optical Systems, Volume 1, Fundamentals of Technical Optics*. Berlin: Wiley-VCH, 2005.

[219] P. C. D. Hobbs, *Building Electro-Optical Systems: Making It All Work*. Wiley-Interscience, 2000.

[220] D. B. Murphy, *Fundamentals of Light Microscopy and Electronic Imaging*. Wiley-Liss, 2001.

[221] C. Sheppard, M. Gu, and M. Roy, "Signal to noise ratio in confocal microscope systems," *J.Microscopy*, vol. 168, pp. 209–218, 1992.

[222] J. F. de Boer, B. Cense, B. H. Park, M. C. Pierce, G. J. Tearney, and B. E. Bouma, "Improved signal-to-noise ratio in spectral-domain compared with time domain optical coherence tomography," *Opt. Lett.*, vol. 28, pp. 2067–2069, 2003.

[223] M. A. Choma, M. V. Sarunic, C. Yang, and J. A. Izzat, "Sensitivity advantage of swept source and fourier domain optical coherence tomography," *Opt. Exp.*, vol. 11, pp. 2183–2189, 2003.

[224] R. Leitgeb, C. Hitzenberger, and A. Fercher, "Performance of fourier domain vs. time domain optical coherence tomography," *Opt. Exp.*, vol. 11, pp. 889–894, 2003.

[225] H. Y. Cheng and Y. C.King, "An ultra low dark current cmos image sensor cell using n+ ring reset," *IEEE Electron Dev.Lett*, vol. 23, no. 9, 2002.

[226] V.Ward, M.Syrzycki, and G. Chapman, "Cmos photodetector with built in light adaptation mechanism," *Microelectronics Journal*, vol. 24, no. 5, pp. 547–553, 1993.

[227] Matlab, version 2007a, the mathworks inc, (2007). [Online]. Available: http://www.mathworks.com/

[228] J. Goodman, *Introduction to Fourier Optics*. New York: McGraw Hill, 1968.

[229] M. Born and E.Wolf, *Principles of Optics*. New York: Pergamon.

[230] N. Chen, C. Wong, and C. J. R. Sheppard, "Focal modulation microscopy," *Opt. Express*, vol. 16, pp. 18 764–18 769, 2008.

[231] C. J. Sheppard, W. Gong, and K. Si, "The divided aperture technique for microscopy through scattering media," *Opt. Express*, vol. 16, pp. 17 031–17 038, 2008.

[232] C. H. Wong, S. P. Chong, C. J. R. Sheppard, and N. Chen, "Simple spatial phase modulator for focal modulation microscopy," *Appl. Opt.*, vol. 48, pp. 3237–3242, 2009.

[233] Y. Hiraoka, J. Sedat, and D. Agard, "Determination of the three-dimensional imaging properties of a light microscope system: partial confocal behavior in epifluorescence microscopy," *Biophys. J.*, vol. 57, pp. 325–333, 1990.

[234] V. Kalchenko, S. Shivtiel, V. Malina, K. Lapid, S. Haramati, T. Lapidot, A. Brill, and A. Harmelin, "Use of lipophilic near-infrared dye in whole-body optical imaging of hematopoietic cell homing," *J. Biomed. Opt.*, vol. 11, p. 050507, 2006.